Variable Stiffness Actuators

Modeling, Control, and Application
to Compliant Bipedal Walking

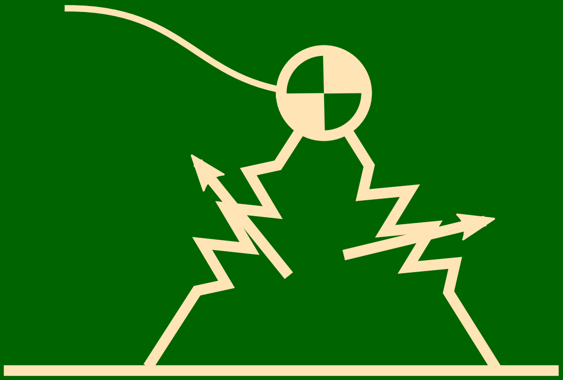

Ludo Visser

Variable Stiffness Actuators:
Modeling, Control, and Application
to Compliant Bipedal Walking

Committee members

Chairman and Secretary:	
prof.dr.ir. Ton Mouthaan	Universiteit Twente
Promotor:	
prof.dr.ir. Stefano Stramigioli	Universiteit Twente
Assistant Promotor:	
dr. Raffaella Carloni	Universiteit Twente
Members:	
prof. Antonio Bicchi	Università di Pisa
prof.dr. Arjan van der Schaft	Rijksuniversiteit Groningen
prof.dr.ir. Just Herder	Universiteit Twente/TU Delft
prof.dr.ir. Herman van der Kooij	Universiteit Twente
prof.dr.ir. Peter Veltink	Universiteit Twente

Paranymphs

Leon Verheggen
Rob Reilink

The research described in this thesis has been conducted at the Robotics and Mechatronics group of the Faculty of Electrical Engineering, Mathematics, and Computer Science at the University of Twente, Enschede, The Netherlands.
This research is part of the research program of the Dutch Institute of Systems and Control (DISC). The author has successfully completed the educational program of the DISC Graduate School.

ISBN 978-90-365-3551-9
DOI 10.3990/1.9789036535519

Printed by Wöhrmann Print Service, Zutphen, The Netherlands.

VARIABLE STIFFNESS ACTUATORS: MODELING, CONTROL, AND APPLICATION TO COMPLIANT BIPEDAL WALKING

PROEFSCHRIFT

ter verkrijging van
de graad van doctor aan de Universiteit Twente,
op gezag van de rector magnificus,
prof.dr. H. Brinksma,
volgens besluit van het College voor Promoties
in het openbaar te verdedigen
op vrijdag 17 mei 2013 om 12:45 uur

door

Ludo Christian Visser

geboren op 13 augustus 1984
te Arnhem.

Dit proefschrift is goedgekeurd door:
prof.dr.ir. S. Stramigioli, *promotor*
dr. R. Carloni, *assistent promotor*

SAMENVATTING

Robots worden traditioneel toegepast in fabrieksomgevingen, waar ze repetitief werk verrichten met hoge precisie en snelheid. Robots die specifiek voor dit soort werk ontworpen zijn hebben een stijve constructie en krachtige motoren, wat ze inherent gevaarlijk maakt. Daarom zijn deze robots zorgvuldig afgeschermd van de arbeiders, om ongelukken door botsingen te voorkomen. Echter, recente ontwikkelingen in robotica onderzoek en ontwikkeling gaan in de richting van mens-robot interactie en samenwerking. Om robots uit de gestructureerde fabrieksomgeving naar dynamische en veranderlijke omgevingen te krijgen moeten robots aan nieuwe criteria voldoen op het gebied van veiligheid en interactie.

Actuatoren met variabele stijfheid worden gekarakteriseerd door de eigenschap dat zij hun uitgangsstijfheid kunnen variëren, onafhankelijk van de positie van de uitgang. Dit wordt in het algemeen gerealiseerd door een aantal elastische elementen op te nemen in het ontwerp van de actuator, tezamen met een aantal interne vrijheidsgraden die bepalen hoe deze elastische elementen aan de uitgang van de actuator worden waargenomen. Een dergelijke regelbare stijfheid stelt een robot uitgerust met deze actuatoren in staat om zijn impedantie mechanisch te regelen, en op deze manier kan een veilige interactie met onbekende omgevingen mechanisch gegarandeerd worden. Bovendien biedt de aanwezigheid van de elastische elementen een manier om tijdelijk mechanische energie op te slaan, wat nieuwe mogelijkheden biedt voor energie-efficiënte actuatie.

Deze dissertatie verkent het ontwerpen en toepassen van actuatoren met variabele stijfheid, met in het bijzonder aandacht voor het energetische gedrag van de actuator tijdens interactie met de omgeving. Voor dit doeleinde wordt een generiek, poort-gebaseerd model gepresenteerd, waarmee de vermogensstromen tussen de interne vrijheidsgraden en de interne elastische elementen, alsook de omgeving, geanalyseerd kunnen worden. Deze analysemethode wordt gebruikt om de energetische presentaties van diverse ontwerpen van actuatoren met variabele stijfheid te vergelijken door deze ontwerpen te categoriseren op basis van hun werkingsprincipes.

Op basis van het poort-gebaseerde model en de analyse van de vermogensstromen worden nieuwe regeltechnieken voorgesteld, met als doel het realiseren van energie-efficiënte actuatie van periodieke bewegingen, door middel van het

gebruik van de interne elastische elementen voor tijdelijke opslag van mechanische energie. De eerste regelmethode slaat energie, toegevoerd via externe verstoringen, op als elastische energie in de interne elastische elementen, en tracht deze energie te hergebruiken voor het compenseren van de verstoring. De tweede methode daarentegen is gebaseerd op resonantie, en tracht het gewenste periodieke gedrag in te bedden in de passieve dynamica van de actuator met variabele stijfheid.

Als laatste wordt de toepassing van actuatie met variabele stijfheid op voortbewegingstechnieken verkend. Er wordt aangetoond dat een variabele stijfheid in de benen van een tweebenige looprobot gunstig is voor de robuustheid van het looppatroon, terwijl tegelijkertijd energie-efficiënte voortbeweging gerealiseerd kan worden. Een regelalgoritme wordt voorgesteld dat deze principes demonstreert in een generiek model van een tweebenige looprobot.

SUMMARY

Traditionally, robots have been employed in factory environments, performing repetitive tasks with high precision at high speeds. Robots designed for this purpose are characterized by rigid links and powerful motors, making them inherently dangerous. As such, these robots are carefully separated from human workers, to prevent accidental collisions. However, in recent years a trend towards human-robot interaction and cooperation can be observed in robotics research and development. Taking robots out of the well-defined factory environments into unknown and dynamically changing environments imposes new requirements on robots in terms of safety and interaction control.

Variable stiffness actuators are characterized by the property that their apparent output stiffness can be changed independently from the actuator position. This is generally achieved by incorporating a number of elastic elements internal to the actuator design, together with a number of internal degrees of freedom that determine how these elastic elements are perceived at the actuator output. This controllable output stiffness enables a robot equipped with these actuators to mechanically control its impedance, thus providing a way to mechanically ensure safe interaction with unknown environments. Moreover, the presence of internal elastic elements introduces a way to temporarily store mechanical energy, opening up new possibilities for energy-efficient actuation.

This thesis explores the design and application of variable stiffness actuators, focussing in particular on the energetic behavior of the actuators interacting with the environment. For this purpose, a generic port-based model is presented, that allows the analysis of the power flows between the internal degrees of freedom and the internal elastic elements of the actuator, and its environment. This power flow analysis method is used to compare the energetic performance of various variable stiffness actuator designs, on the basis of a categorizing of their working principles.

Using the port-based model and the power flow analysis, new control methods are proposed, with the aim of realizing energy-efficient actuation of periodic motions by using the internal elastic elements to temporarily store mechanical energy. The first control method purposefully stores energy, supplied by external disturbances, as elastic energy in the internal elastic elements and aims to reuse this energy to reject the disturbance. The second control method instead takes a

resonance-based approach, in which the desired oscillatory behavior is embodied in the passive dynamics of the variable stiffness actuator.

Finally, the application of variable stiffness actuation to locomotion is investigated. It is shown that a variable compliance in the legs of bipedal walkers can be beneficial to the robustness of the gaits, while achieving at the same time energy-efficient locomotion. A control strategy is presented, that demonstrates these principles in a template model of a bipedal walker.

CONTENTS

II Selected Papers 49

III Appendix 155

CHAPTER 1

Introduction

Traditionally, the main application area for robots has been the manufacturing industry, where robots perform repetitive tasks with high precision. A good example can be found in car factories, such as shown in Figure 1.1, where industrial robots are used to perform high-precision welding tasks. Such tasks are performed by executing a sequence of predefined motions in a structured environment, without any human intervention. In fact, because these robots are not aware of their environment, their working area is strictly separated from the rest of the factory, to protect human workers from being injured.

Recently, robots are being developed that can work together with humans and cooperate with them. Such robots must meet very different requirements than robots that operate in factory environments. In particular, when robots operate a dynamically changing environment where humans are also present, the most important requirement for such robots is that they are safe, both towards human and robot [72]. This, in turn, requires that these robots need to be adaptable, so that they can safely interact with environments with varying properties and characteristics [5, 1].

Furthermore, many use-cases of human-robot interaction and cooperation require that the robot is mobile. In contrast with the mostly immobile factory robots, this requirement introduces new challenges in energy efficiency. In particular, robot locomotion should be highly energy-efficient in order to be able to use on-board energy storage as much as possible for interaction and cooperation tasks. While prevalent wheeled platforms provide an energy efficient way of locomotion, they are generally not well suited for human environments where steps, stairs, and uneven surfaces are commonly encountered. Legged robots are much more suitable for such environments, but energy-efficient and robust legged locomotion is still an unsolved problem [48].

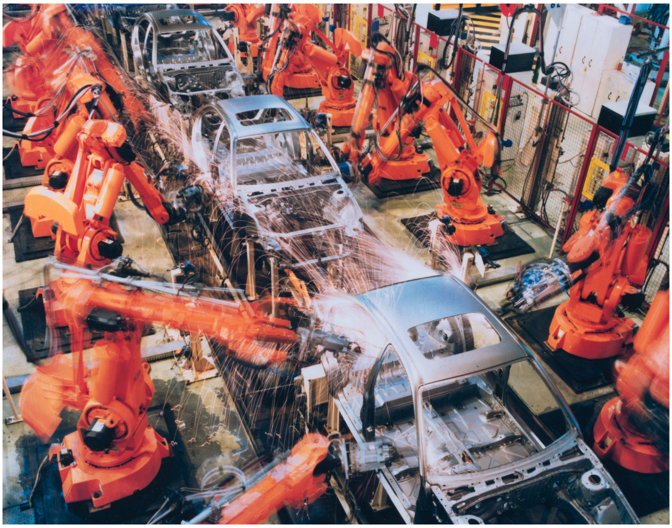

Figure 1.1: ABB IRB 6400 robots spot-welding car frames—Robots are commonly used in factories, where they perform repetitive tasks with high precision at high speed. However, due to their size and operating speed, and their lack of environmental awareness, such robots are extremely unsafe. As such, these manufacturing lines are carefully shielded off from the rest of the factory to prevent accidental collisions. *Image source: abb.com*

One aspect of addressing intrinsic safety and energy efficiency is robot actuation, since the dynamic properties of the actuation systems of a robot contribute significantly to the overall dynamics. Safe and energy-efficient robots can be realized only if the actuation system can be made intrinsically safe and energy efficient.

1.1 Conventional Actuation Principles

The repetitive and high-precision nature of factory tasks has resulted in the design of highly specialized robots, with "stiff actuation" to achieve the required levels of accuracy. Here, "stiff actuation" means that the combination of the motor and motor control result in a joint that appears to be stiff, i.e. when disturbed, the joint motion deviates very little from the desired motion. This stiffness is achieved in a number of ways. In the first place, the mechanical structure of the robot is designed to be as stiff as possible, with the aim of preventing undesired vibrations to propagate through the system. Secondly, high-performance electromechanical motors with high-gain controllers are used to accurately control the joint motion.

The result of these design principles is a robot that can accurately track specified joint trajectories, such that precision tasks can be performed at high speeds. This facilitates high-quality, high-throughput production lines, which are essential to manufacturing industries. However, a side effect is that, due to the stiff structures and control combined with high-speed motion, that these robots are unsafe. The lack of safety is due to the high levels of kinetic energy associated with the fast motions of the robot, which will be released upon impact. As a result, robotic production lines are shielded off from the rest of the factory, with the aim of preventing accidental collisions.

If robots are to operate in an environment together with humans, safety is a high priority. It cannot be assumed that accidental collisions can be prevented by means of sensors, as this would require large amounts of computational resources, and redundant sensors would be required to safeguard against sensor failure. Instead, an intrinsic level of safety is preferred by designing the robot such that it is mechanically safe even in the absence of sensory feedback and control action. This can be partly achieved by using lightweight materials and more compliant mechanical structures, but this cannot overcome the intrinsic stiffness of conventional electromechanical actuators. For example, a DC-motor with a motor inertia J and a gearbox transmission ratio $1 : n$ adds a reflected inertia of $n^2 \cdot J$ to the joint that the motor is actuating. With gearbox ratios in the order of $1 : 100$, the reflected inertia contributes significantly to the total robot inertia. This effect can be partly mitigated by using direct-drive motors, but such motors need to be much larger in order to achieve the same level of performance of geared motors.

A second drawback of conventional electromechanical actuators is their poor energy efficiency. While motors and gearboxes by themselves are getting increasingly more efficient, dissipation of electrical energy cannot be avoided. Furthermore, electrical motors are inherently inefficient when negative work is done. Especially the automotive industry is directing efforts towards enabling back-drivable motors to convert mechanical energy back to electrical energy, but the conversion of energy from the mechanical domain to the electrical domain will always be inherently inefficient. To enable the deployment of safe and energy efficient robots in human environments, these issues need to be addressed.

1.2 Variable Stiffness Actuators

New actuation principles are being developed by the robotics community, which aim to reach levels of performance in actuation that match or exceed human performance. Examples include torque-feedback systems [1], artificial muscles [63], and series-elastic actuation [73]. Many of these new principles introduce an intrinsic compliance to the actuation system, which is believed to be a necessary requirement for safe interaction [4], and also allows to mechanically store energy for increasing energy efficiency [52]. However, introducing compliance will result in decreased accuracy, which might be problematic for some tasks. Yet, the added compliance renders robots intrinsically safe and opens possibilities for energy-efficient actuation based on resonance principles [56]. Therefore, research efforts have been directed towards combining the advantages of both conventional electromechanical actuators and those of compliant actuators.

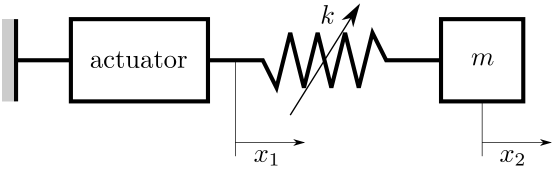

Figure 1.2: The working principle of variable stiffness actuators—The equilibrium position x_1 is controlled by a conventional actuator, that is connected to the load m by a spring with controllable stiffness k.

To negotiate the trade-off between compliancy and accuracy, the concept of *variable stiffness actuation* has been introduced [5]. This principle introduces a compliant element with controllable stiffness in between a conventional electromechanical actuator and the joint that is being actuated, as illustrated in Figure 1.2. A variable stiffness actuator thus has two controlled degrees of freedom: the equilibrium position x_1 and the stiffness k. The dynamics of the load m are those of a spring-mass system with a variable stiffness:

$$m\ddot{x}_2(t) = k(t)\left(x_1(t) - x_2(t)\right).$$

Variable stiffness actuators allow to balance between compliant and stiff actuation, depending on the task at hand. In particular applications the stiffness can be tuned to realize specific interaction behavior with an unknown environment, or to realize resonance frequencies for energy-efficient actuation of periodic motions. For example, analogously to human capabilities, a robotic walker equipped with variable stiffness actuators can tune its leg stiffness to achieve energy-efficient locomotion on even terrain, or improve robustness on uneven terrain. Therefore, variable stiffness actuators are essential to new robotic applications in human-robot interaction and cooperation.

1.3 About this Thesis

The focus of this thesis is on modeling and control of variable stiffness actuators, as well as their application to compliant bipedal walking. The thesis is split in two parts: the first part aims to provide a complete overview of the obtained results in the form of a short dissertation, while the second part provides a selection of papers that are at the basis of these results, providing more details on particular aspects of the work.

Within the first part, Chapter 2 presents an overview of variable stiffness actuator designs, and a classification of working principles is established. This classification is instrumental in understanding the capabilities and performance limits of various designs. In Chapter 3, a generic model for variable stiffness actuators is presented, based on a port-based modeling framework. With this model, the power flows within a variable stiffness actuator can be investigated, giving insight in the energy exchange between the actuator and its environment. Based on these insights, a metric for energy efficiency can be established, which is further elaborated for the previously identified working principles. The port-based model is the basis for a number of novel control methods, presented in Chapter 4. These methods exploit the energy-storing capabilities of the internal compliant elements of variable stiffness actuators, thus arriving at energy-efficient control. Chapter 5 investigates the application of variable stiffness actuation to bipedal locomotion. Starting from a conceptual model for human walking, it is shown how variable stiffness actuation can be used to improves robustness and realize energy-efficient walking robots. Finally, Chapter 6 presents a discussion of the results, and recommendations for future work.

1.3.1 The VIACTORS Project

The work presented in this thesis has been conducted in the context of the European project VIACTORS, an acronym for "Variable Impedance ACTuation systems embodying advanced interaction behaviORS" (`http://www.viactors.org`). The goal of this project has been to develop new actuation principles for robots to safely coexist and cooperate with humans. In particular, the project aimed to investigate how human performance levels can be achieved in terms of manipulation and locomotion, while at the same time be energy efficient and inherently safe.

Within the project, the premise is that these goals can be achieved by developing *variable impedance actuators*, which allow generic control of interaction with the environment by modifying the actuator impedance to match the expected environment. Variable stiffness actuators are a subset of variable impedance actuators, since they only allow the actuator stiffness to be adjusted. This thesis shows how variable stiffness actuators can be used to achieve the project goals. In particular, it is shown how these actuators can realize energy-efficient actuation by exploiting the energy-storing capabilities of the internal elastic elements. Furthermore, it is shown that variable stiffness actuators can be employed to mimic human capabilities in locomotion, realizing robust and energy-efficient locomotion by regulation of leg stiffness.

1.3.2 Overview of Publications

A number of publications in international conferences and journals have lead up to the results presented in this thesis. A few of these publications are included in the second part of this thesis:

- Chapter 7: "Energy-Efficient Variable Stiffness Actuators", published in: *IEEE Transactions on Robotics*, 2011.
- Chapter 8: "Variable Stiffness Actuators: a Port-based Power Flow Analysis", published in: *IEEE Transactions on Robotics*, 2012.

- Chapter 9: “Energy-Efficient Control of Robots with Variable Stiffness Actuators”, published in: *Proceedings of the 8th IFAC Symposium on Nonlinear Control Systems*, 2010.
- Chapter 10: “Embodying Desired Behavior in Variable Stiffness Actuators”, published in: *Proceedings of the 18th IFAC World Congress*, 2011.
- Chapter 11: “Energy-Efficient Bipedal Locomotion using Variable Stiffness Actuation”, submitted to: *IEEE Transactions on Robotics*, 2013.

A complete overview of all publications can be found in the bibliography.

Part I

Dissertation

CHAPTER 2

Variable Stiffness Actuators

The defining characteristic of variable stiffness actuators is that this class of actuators is capable of varying the apparent output stiffness independently of the actuator output position. This allows to control the interaction forces between the robot and the environment, which is an essential ability for robots operating in an unknown environment. In particular, when interaction forces and impedance can be controlled, interaction with the environment can be rendered safe and stable, even in unknown conditions.

This chapter provides a background in the emergence of variable stiffness actuators. Furthermore, an overview of working principles for variable stiffness actuator is presented. These designs can be classified to establish a set of conceptual working principles, that lie at the basis of these designs. This classification is instrumental in understanding the actuator designs and in evaluating their performance.

2.1 Origin and Background

Initially, robots have most often been position-controlled, such as the spot-welding robots depicted in Figure 1.1. This is sufficient as long as the joint trajectories of the robot are known in advance, which is generally the case in production lines. The development of high-resolution position sensors, such as encoders, has further facilitated the development of the high-speed, high-precision robots that are required in modern manufacturing industry.

However, there are many applications in which position control does not suffice. In particular, when a robot needs to physically interact with the environment, position control of the end-effector, e.g. a tool, can result in unstable behavior. For example, consider a robot with a sanding tool that needs to smoothen a particular surface of an object. Let the joint configuration of the robot be denoted by $q(t)$, and assume that these quantities can be accurately measured by position sensors. Let $q_d(t)$ be predefined desired joint trajectories, designed such that the sanding tool follows a specific trajectory in Cartesian space. A commonly used control strategy is to calculate joint torques τ using a proportional-integral-differential (PID) control law, i.e.

$$\tau = K_p(q_d(t) - q(t)) + K_i \int (q_d(t) - q(t))\,\mathrm{d}t + K_d \frac{\mathrm{d}}{\mathrm{d}t}(q_d(t) - q(t)),$$

where K_p, K_i, K_d are positive-definite diagonal gain matrices. Assuming that the time derivative of $q(t)$ is available, it can be readily shown that applying this torque to the joint will result in the error $q_d(t) - q(t)$ converging to zero, and thus that the tool tracks the intended trajectory in Cartesian space.

However, in this scenario, the surface to be sanded is inherently unknown. A static error $q_d(t) - q(t)$, due to the fact that the sanding tool cannot move through the surface to be sanded, might result in excessively high torques τ. Furthermore, when this control law is discretized to be implemented on a computer, such scenarios can easily lead to instability. This can be avoided by employing a different technique called *force control* [77]. In this approach, instead of defining the position trajectory for the tool, a desired *interaction force* is defined. In this way, when the tool is in contact with the environment, no instability will occur when this contact point deviates from the intended tool position. In the context of the sanding example, the sanding tool will apply a suitable force to the surface to be sanded, even when the surface is uneven.

Force control can be realized similar to position control, replacing position sensors by force sensors, and implementing a feedback control law in software. However, this approach suffers from two drawbacks. First, force sensors are expensive and subject to noise. Furthermore, the bandwidth of a digitally implemented controlled inherently has a limited bandwidth, bounded by the sample rate of the analog-to-digital converters. While the bandwidth limitation is of course also present in position control, high-frequency contact dynamics that are observed in scenarios where force control would be beneficial, can pose serious problems when control bandwidth is limited.

To overcome the issues with force sensors, *series elastics actuators*, which use an internal spring as force sensor, have been proposed [73]. The working principle is depicted in Figure 2.1, and is based on Hooke's Law, which states that the force exerted on by a spring is proportional to its elongation, i.e. $F = k(x_1 - x_2)$. Since accurate position measurements can be obtained through relatively cheap sensors, the spring can be used as a force sensing device by measuring the position of both of its end points. In a series elastics actuator, one of the end points of the spring is attached to a conventional, position-controlled actuator, and the other end point connected to e.g. a robotic joint. The name thus originates from the spring (i.e. an elastic element) placed in series with a conventional actuator. In this way, the desired force to be applied to the joint can be realized by a conventional actuator

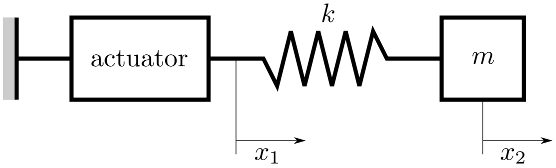

Figure 2.1: The working principle of series elastic actuation—The equilibrium position x_1 is controlled by a conventional actuator, that is connected to the load, consisting of a mass m, by a spring with stiffness k. In this way the load is decoupled from the actuator inertia.

and position measurements.

The main advantage of series elastics actuation over software-implemented force control is that the internal elastic element realizes a mechanical compliance, rather than a software-emulated compliance. This circumvents the bandwidth problem in physical interaction scenarios, since the spring realizes a physical actuator impedance suitable for interaction with stiff environments. However, this impedance is constant, which implies that a robot equipped with series elastics actuators will need to be designed keeping in mind the properties of the environment it will be operating in. If the robot is to operate in a wide variety of environments with different properties, it might not be possible to find a fixed actuator impedance that is suitable for all scenarios. This is were *variable stiffness actuators* offer a solution.

As shown in Figure 1.2, the working principle of variable stiffness actuators is very similar to that of series elastics actuators. The essential difference is that in variable stiffness actuators the apparent elasticity of the compliant element, i.e. how it is perceived by the load at the actuator output, can be varied as desired. This allows a robot to adapt itself to its environment, much like humans do. For example, a robot operating in a largely unknown environment should be compliant, so that unexpected impacts can be absorbed by the mechanical impedance. In contrast, a robot performing a high-precision task needs to present a high stiffness impedance, so that desired levels of accuracy may be achieved.

It is clear why variable stiffness actuators can be advantageous in certain applications. Translating the concept shown in Figure 1.2 to a physical realization can be done in many ways, each with specific advantages and disadvantages. The focus of the remainder of this chapter will be on different working principles for the realization of variable stiffness actuators and the properties of these principles.

2.2 Working Principles

Any variable stiffness actuator needs to have one or more internal compliant elements, and one or more internal degrees of freedom that determine how these compliant elements are perceived at the actuator output. Furthermore, one or more actuated degrees of freedom are needed to control the equilibrium position of

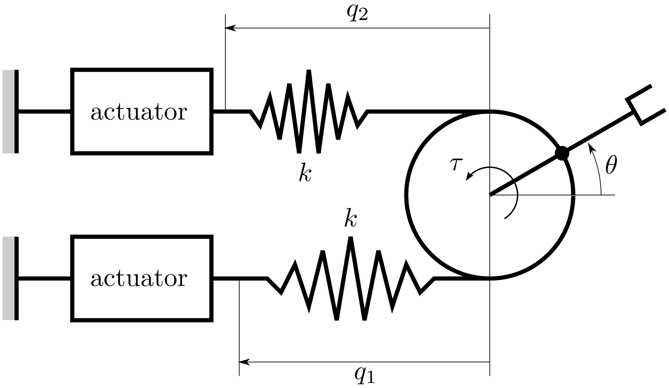

Figure 2.2: Variable stiffness actuation using antagonistic springs—The working principle consists of two springs with a nonlinear force-displacement relation, placed in an antagonistic configuration. The apparent output stiffness can be modulated by pretension of the springs, while the equilibrium position can be changed by operating the two actuators in differential mode.

the actuator, analogous to the equilibrium position of a spring. These degrees of freedom and compliant elements can be organized in many ways, but it is possible to classify most of the designs in three categories, corresponding to elementary working principles.

2.2.1 Antagonistic Spring Setup

Humans are capable of varying for example the stiffness of their elbow by co-contraction of biceps and triceps. In general, by co-contraction of antagonistic muscle pairs the stiffness of corresponding joints can be adjusted to suit a particular task. This can be emulated in a variable stiffness actuator as illustrated in Figure 2.2. In this design principle, two nonlinear springs are on one end connected to a pulley, and each of the other ends is connected to an actuated linear degree of freedom, denoted by $q_i, i = 1, 2$. The angle θ of the pulley is considered the output motion of the variable stiffness actuator, with the actuator torque τ collocated with output angle θ.

If the pulley has radius R, then the torque τ is given by

$$\tau = R(F_2 - F_1),$$

where F_i is the force exerted by the springs. The torsional stiffness σ perceived at the output is given by[1]

$$\sigma = \frac{\partial \tau}{\partial \theta} = R\left(\frac{\partial F_2}{\partial \theta} - \frac{\partial F_1}{\partial \theta}\right).$$

---

[1] By convention, stiffness is always a positive quantity, even if evaluating the partial derivative $\partial\tau/\partial\theta$ yields a negative value.

Assuming that the force generated by the spring springs is quadratic[2] in the spring elongation, i.e.

$$F_1 = k(q_1 + R\theta)^2 \quad \text{and} \quad F_2 = k(q_2 - R\theta)^2,$$

where k is a constant of elasticity, the generated output torque is given by:

$$\begin{aligned}\tau &= R\left(k(q_2 - R\theta)^2 - k(q_1 + R\theta)^2\right) \\ &= Rk\left(q_2^2 - q_1^2 - 2R(q_1 + q_2)\theta\right).\end{aligned}$$

From this, it is observed that the torsional output stiffness $\sigma = 2R^2k(q_1 + q_2)$ can be adjusted by operating the two internal degrees of freedom in common mode, analogously to muscle co-contraction. The equilibrium position of the actuator can be changed by operating the two internal degrees of freedom in differential mode, i.e. by keeping $q_1 - q_2$ constant.

This biologically inspired approach is at the basis of the designs presented in e.g. [33, 54, 46]. Its main advantages are the intuitive design and the simple construction principle. The main drawbacks are that the range of output stiffness that can be achieved is proportional to the operating range of the internal degrees of freedom q_i. Furthermore, if the stiffness is increased, work is converted in potential energy stored in the springs. This energy is essentially “locked up”, and cannot be used to do useful work at the output. This last point will be further elaborated in Chapter 3.

2.2.2 Pretension Mechanisms

In the antagonistic spring setup, both internal degrees of freedom are used equivalently to vary the apparent output stiffness and to change the equilibrium position of the actuator. This means that, if for a particular set of design requirements it is needed to vary the stiffness over only a small range, while the equilibrium position needs to be varied over a large range, both internal degrees of freedom need to have a large range of motion to accommodate both requirements. This drawback can be overcome by decoupling stiffness control and equilibrium position control, as conceptually shown in Figure 2.3.

In this working principle, which is at the basis of the designs presented in [60, 75, 61, 18, 74], the linear degree of freedom q_1 controls the pretension of the nonlinear springs, while the rotational degree of freedom q_2, in between the pulley and the actuator output, controls the equilibrium position of the actuator. As in the previous design, the output is the angle θ, with collocated torque τ.

Letting R denote again the radius of the pulley, the torque τ can be calculated as

$$\tau = R(F_2 - F_1),$$

---

[2] Taking linear springs, i.e. in which the generated force is of the form $F_i = k(q \pm R\theta)$, renders $\partial F/\partial\theta$ constant, leaving no way to influence the apparent output stiffness by means of control of the internal degrees of freedom.

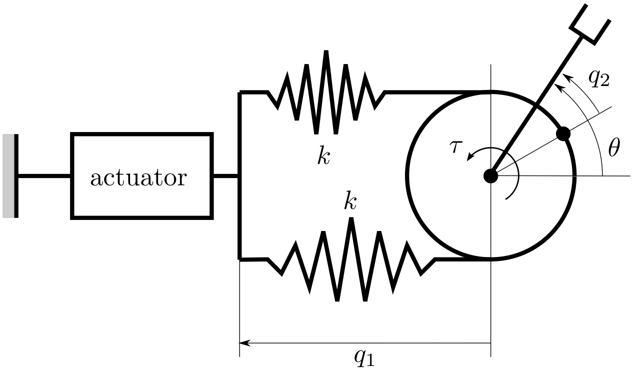

Figure 2.3: Variable stiffness actuation using a pretension mechanism—The working principle consists of two springs with a nonlinear force-displacement relation, with a conventional actuator modulating the pretension of these springs, thus modulating the apparent output stiffness. The equilibrium position can be changed by a separate actuator in series with the rotation axis of the pulley.

with, assuming again springs with a quadratic force-displacement relation, the forces given by:

$$F_1 = k\left(q_1 + R(\theta - q_2)\right)^2 \quad \text{and} \quad F_2 = k\left(q_1 - R(\theta - q_2)\right)^2 .$$

Substitution then yields

$$\tau = -4R^2 k q_1 (\theta - q_2),$$

from which the perceived torsional output stiffness σ is calculated as

$$\sigma = \frac{\partial \tau}{\partial \theta} = 4R^2 k q_1 .$$

This shows indeed that only the degree of freedom q_1 is used to adjust the apparent output stiffness. In this way, specific requirements for the range of stiffness and the range of motion of the actuator can be met by using adequate motors for the actuation of the corresponding degrees of freedom. However, this design still suffers from “locked up” energy.

2.2.3 Variable Transmission Ratio

Instead of changing the apparent actuator output stiffness by modifying the state of the internal springs, as is done in the previous two designs, the apparent stiffness can also be changed by introducing a variable transmission ratio between the internal spring element and the actuator output, thus avoiding the potential “lock-up” of energy. This concept is shown in Figure 2.4, and is essentially an evolution of the series elastics actuation principle shown in Figure 2.1.

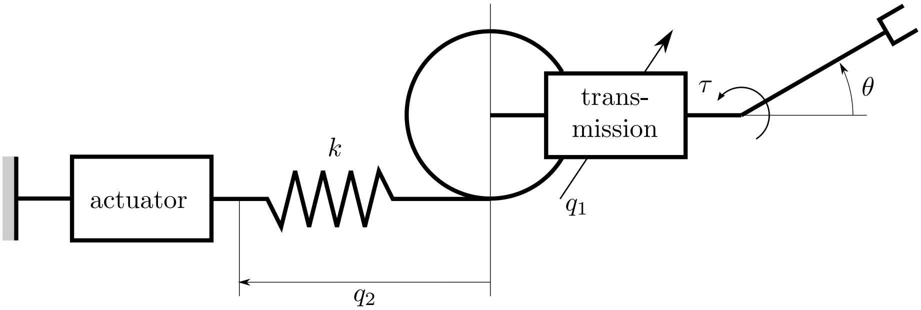

Figure 2.4: Variable stiffness actuation using a variable transmission—The controllable transmission ratio determines how the linear spring is perceived at the actuator output. The internal degree of freedom q_1 only controls the transmission ratio. The second degree of freedom q_2 is used to control the equilibrium position of the actuator.

The concept uses a variable transmission, of which the transmission ratio is controlled by the internal degree of freedom q_1, to modulate the apparent actuator output stiffness. As in the previous design, the internal degree of freedom q_2 is used to control the equilibrium position of the actuator output. The output angle θ is again collocated with the torque τ.

Assuming a spring abiding Hooke's Law, i.e. a linear spring, exerting a force $F = ks$, where k is the constant of elasticity and $s = s(q_2, \theta)$ is the elongation of the internal spring. Assuming that the pulley has unity radius and simplifying the implementation of the transmission ratio to a linear dependence on q_1, the output torque τ is calculated as

$$\tau = q_1 k s.$$

We then obtain the torsional output stiffness as:

$$\sigma = \frac{\partial \tau}{\partial \theta} = q_1 k \frac{\partial s}{\partial \theta}.$$

This shows that the apparent output stiffness can be manipulated by proper control of the internal degree of freedom q_1.

The concept of a spring in series with a continuously variable transmission was explored in [52, 51], with the aim of energy efficient actuation. The work presented in [68, 67] first applied the concept to the realization of energy efficient variable stiffness actuators. The mechanical advantages of this approach were simultaneously and independently recognized in [34, 39], and more recently in [35, 71, 26]. Chapter 3 further explores the energetic properties of this concept.

2.2.4 Other Design Principles

Some variable stiffness actuator designs cannot be captured by the concepts described in this chapter. For example, the "Jack Spring"$^{\text{TM}}$ presented in [32] varies the number of active coils of a spring to vary its stiffness. The design presented in [9] controls the apparent actuator stiffness by changing the configuration of a set of permanent magnets inside the actuator.

The list of designs mentioned in this chapter is therefore not exhaustive. However, it is considered complete enough for the purpose of the work presented in this thesis. In particular, the design principles presented in this chapter provide a basis for deriving a generic model for variable stiffness actuators, which will be elaborated in Chapter 3.

CHAPTER 3

Modeling and Analysis of Variable Stiffness Actuators

The previous chapter presented a number of working principles for variable stiffness actuators. However, this categorization is not yet sufficient to compare different actuator designs. In particular, it is desired that a uniform model is developed, that can be used to capture the properties of a wide variety of variable stiffness actuators in a uniform way.

This chapter presents a generic port-based model for variable stiffness actuators. The port-based approach enables an analysis of performance from an energetic viewpoint, showing how power flows between the variable stiffness actuator and the environment. In particular, using this model, a metric for energy efficiency is established, which allows to better evaluate the performance of the different variable stiffness actuator working principles.

3.1 A Port-based Model

The port-based approach focusses on power exchange between interconnected subsystems. Therefore, port-based modeling is a powerful way of modeling physical systems from an energetic point of view [14, 50, 19]. Chapter 7 provides an in-depth treatment of port-based modeling for variable stiffness actuators. Here the main results and the application of the model to energy efficiency analysis are presented.

Assumption 3.1 In deriving a generic model for variable stiffness actuators, it is assumed that

- the actuator has one degree of freedom output motion, its configuration denoted by the generalized coordinate r;

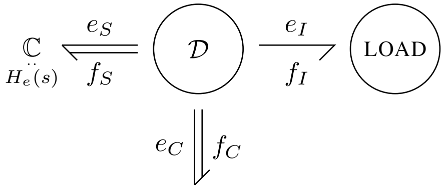

Figure 3.1: Generic port-based model of variable stiffness actuators—The internal elastic elements are represented by the $\mathbb{C}$-element. The internal degrees of freedom are controlled through the control port (f_C, e_C), while the interaction with the load is through the interaction port (f_I, e_I).

- the actuator has n_s internal elastic elements, with state s and an energy function $H_e(s)$ describing the amount of elastic energy as function of the spring state;
- the actuator has $n_q \geq n_s$ actuated degrees of freedom with configuration q;
- the apparent output stiffness K is determined by the intrinsic properties of the internal elastic elements and their state, and the configuration of the internal degrees of freedom.

Furthermore, it is assumed that internal friction and inertias can be neglected without affecting the working principle of the actuator design. •

In Figure 3.1 a bond graph representation of a generic model for variable stiffness actuators is presented, incorporating the assumptions listed above. In particular, the model includes a multidimensional $\mathbb{C}$-element representing the internal elastic elements, a one-dimensional interaction port (f_I, e_I) connecting the actuator to its load, and a multidimensional control port (f_C, e_C) defining the dynamics of the internal degrees of freedom. The Dirac structure $\mathcal{D}$ defines the interconnection structure. For the working principles presented in Chapter 2, the Dirac structure is defined by the actuator kinematics.

The port behavior of the $\mathbb{C}$-element is described by

$$\dot{s} = f_S, \quad e_S = \frac{\partial H_e}{\partial s}, \tag{3.1}$$

such that the dual product $\langle e_S | f_S \rangle$ of the flow f_S and the effort[1] e_S defines the power flow through the port:

$$\langle e_S | f_S \rangle := e_S^T f_S = \dot{H}_e(s). \tag{3.2}$$

This description allows the $\mathbb{C}$-element to model any elastic element.

---

[1] Efforts behave as row-vectors (co-vectors), but in this thesis they will be written as column-vectors for notational conveniency.

The internal degrees of freedom are controlled through the control port, with associated port variables (f_C, e_C). Here, the flow f_C corresponds to the rate of change $\dot{q}$ of the configuration q of the internal degrees of freedom, with e_C the collocated effort.

The output behavior of the variable stiffness actuator is described by the port variables (f_I, e_I), corresponding to the rate of change $\dot{r}$ of the actuator output position, and the torque or force exerted by the actuator, respectively. The apparent output stiffness K is then defined as

$$K := \frac{\delta e_I}{\delta r}, \tag{3.3}$$

i.e. the infinitesimal change in generated effort resulting from an infinitesimal displacement of the output position. Note that, under the previously stated assumptions, the apparent stiffness K should at least be a function of q, and possibly also of r.

The Dirac structure $\mathcal{D}$ defines a power-continuous interconnection of the $\mathbb{C}$-element and the control and interaction ports. It thus describes the kinematic working principle of the variable stiffness actuator, and may therefore depend on the configuration variables q of the internal degrees of freedom and the actuator output position r. Considering the causality of the ports, it can be represented by a skew-symmetric matrix $D(q,r)$ in

$$\begin{bmatrix} f_S \\ e_C \\ e_I \end{bmatrix} = \underbrace{\begin{bmatrix} 0 & A(q,r) & B(q,r) \\ -A^T(q,r) & 0 & 0 \\ -B^T(q,r) & 0 & 0 \end{bmatrix}}_{D(q,r)} \begin{bmatrix} e_S \\ f_C \\ f_I \end{bmatrix}. \tag{3.4}$$

The sub-matrices $A(q,r)$ and $B(q,r)$ define the relation between f_C and f_I, i.e. the rates of change of the configuration variables q and r, and f_S, i.e. the rate of change of the state variables s of the elastic elements. Therefore, by defining the kinematic relationship λ between the configuration (q,r) and the state s, i.e.

$$\lambda : (q,r) \mapsto s, \tag{3.5}$$

it is found that

$$A(q,r) := \frac{\partial \lambda}{\partial q}(q,r) \quad \text{and} \quad B(q,r) := \frac{\partial \lambda}{\partial r}(q,r). \tag{3.6}$$

The kinematic relations (3.6) and the representation of the Dirac structure (3.4) provide important insights in the working principles of the variable stiffness actuator. In particular, the generic port-based model enables to investigate the power flows in the control and interaction ports, and the energy storage of the elastic elements. This analysis is the focus of the remainder of this chapter, providing the basis for energy-based control strategies for variable stiffness actuators, which will be discussed in Chapter 4.

3.2 Power Flow Analysis

As stated before, the Dirac structure defines a power-continuous interconnection of the connected ports. As such, the following equality follows directly from (3.4):

$$\langle e_S | f_S \rangle + \langle e_C | f_C \rangle + \langle e_I | f_I \rangle = 0.$$

Using (3.2) and the kinematic relations (3.6) yields

$$\frac{\partial^T H_e}{\partial s} \left(\dot{s} + A(q,r)\dot{q} + B(q,r)\dot{r} \right) = 0. \tag{3.7}$$

From this, the following result is obtained.

Lemma 3.1 (Energy-free stiffness regulation) *The apparent output stiffness of a variable stiffness actuator can be changed in an energy-free way if there exists a trajectory $q(t)$ that realizes the desired change of stiffness while simultaneously satisfying*

$$\dot{q} \in \mathit{ker}\, A(q,r),$$

where $\mathit{ker}\, A(q,r)$ denotes the kernel of the Jacobian matrix $A(q,r)$.

Proof: It follows directly from (3.7) that trajectories $q(t)$ satisfying the conditions of Lemma 3.1 results in

$$\dot{H}_e = -e_S^T B(q,r)\dot{r},$$

i.e. the reconfiguration of the internal degrees of freedom does not induce a power flow through the control port, and any change in the energy balance is due to interaction with the environment through the interaction port. $\square$

Remark 3.1 It is emphasized that Lemma 3.1 states that the stiffness change is energy-free, which mean that the energy balance is not altered by the control action. In particular, if an actuator has multiple internal degrees of freedom, it is possible that positive work is done on one degree of freedom, while the same amount of negative work is done on another. The net result is a zero power flow through the control port, but it is apparent that in fact energy is required to achieve the change in output stiffness. $\triangleleft$

In order to realize variable stiffness actuators that can change their apparent output stiffness in an energy-free way, Lemma 3.1 provides insights in design requirements. In particular, the kinematics of the actuator must be such that $A(q,r)$ in fact has a kernel. This implies that the mechanical design must realize a redundancy in the kinematic structure that connects the internal degrees of freedom to the elastic elements. Furthermore, it can be shown that the apparent output stiffness, for a particular output position $r = \bar{r}$, is given by [8]

$$K(q, r = \bar{r}) = B^T(q,\bar{r}) \frac{\partial^2 H_e}{\partial s^2} B(q,\bar{r}),$$

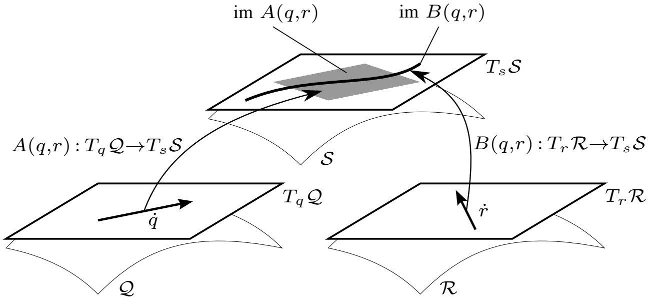

Figure 3.2: Relations between tangent spaces—The kinematic maps $A(q, r)$ and $B(q, r)$ define subspaces on $T_s\mathcal{S}$. Because the actuator output has only one degree of freedom, the integral manifold of the map $B(q, r)$ may define a submanifold of $\mathcal{S}$.

which implies that an energy-free stiffness change can be achieved only if $B(q, r)$ strictly depends on q. Together, these requirements imply that only designs based on a variable transmission ratio can be capable of energy-free stiffness changes. This statement will be further elaborated in Section 3.3.

The condition stated in Lemma 3.1 is sufficient for changing the apparent actuator output stiffness in an energy-free way. However, it does not say anything about the distribution of power if the condition is not satisfied. In particular, the way in which the power flow through the control port is distributed to the internal elastic elements and the interaction port provides information on the energetic costs of changing the apparent output stiffness. To answer this question, the kinematic relations defined in (3.6) need to be further investigated. Chapter 8 provides an in-depth analysis of relation between actuator kinematics and these power flows. Here, the main results are summarized.

For the analysis, consider the kinematic relation (3.5), which is a mapping between manifolds. In particular, $(q, r) \in \mathcal{Q} \times \mathcal{R}$, where $\mathcal{Q}$ is a state manifold of dimension n_q, while $\mathcal{R}$ is, by assumption, one-dimensional. Then, considering the state manifold $\mathcal{S}$ of dimension n_s for the state of the internal elastic elements, the map λ is defined as

$$\lambda : \quad \mathcal{Q} \times \mathcal{R} \to \mathcal{S},$$

and, from (3.6),

$$\begin{aligned} A(q, r) : &\quad T_q\mathcal{Q} \to T_s\mathcal{S}, \\ B(q, r) : &\quad T_r\mathcal{R} \to T_s\mathcal{S}, \end{aligned}$$

where $T_x\mathcal{X}$ denotes the tangent space to $\mathcal{X}$ at $x \in \mathcal{X}$. These relations are visualized in Figure 3.2.

Because $\mathcal{R}$ is one-dimensional, the image of the tangent map $B(q, r)$ is a line on $T_s\mathcal{S}$. Instead of using the natural coordinates on $T_s\mathcal{S}$, let $b^{\|}$ be a unit vector such that

$$\operatorname{im} B(q,r) = \operatorname{span}\{b^{\|}\}.$$

To complete the coordinate set, let $b^{\perp}$ be a set of $n_s - 1$ unit vectors such that

$$\operatorname{span}\{b^{\perp}\} = \operatorname{im} B^{\perp}(q,r),$$

where $\operatorname{im} B^{\perp}(q,r)$ is the orthogonal complement to $\operatorname{im} B(q,r)$, such that

$$T_s\mathcal{S} = \operatorname{im} B(q,r) \oplus \operatorname{im} B^{\perp}(q,r).$$

Length and orthogonality of vectors on $T_s\mathcal{S}$ are only defined if a metric is defined on this vector space. Elements of $T_s\mathcal{S}$ can be interpreted as infinitesimal displacements δs, corresponding to infinitesimal changes of the state of the elastic elements. It can be shown that the stiffness matrix is a physically meaningful metric for δs [25, 24]. Since the model does not incorporate internal friction, the variable stiffness actuator model represents a conservative system, and in this case the stiffness matrix is given by the Hessian of the potential energy function [76]. Therefore, the metric W on $T_s\mathcal{S}$ is defined as:

$$W := \frac{\partial^2 H_e}{\partial s^2},$$

where it is noted that the norm induced by W, i.e. $\|\delta s\|_W^2 := \delta s^T W \delta s$, has the units of energy. The new coordinate vectors for $T_s\mathcal{S}$ are now defined through the additional orthogonality constraint

$$\langle b^{\|}, b_i^{\perp} \rangle_W = 0, \quad i = 1, \ldots, n_s - 1,$$

where $\langle \cdot, \cdot \rangle_W$ denotes the inner product with respect to the metric W.

With the set $\{b^{\|}, b^{\perp}\}$ now defining a new set of coordinates for $T_s\mathcal{S}$, a change of coordinates can be defined. Let S_b be a state-dependent matrix defining the change of coordinates, i.e.

$$S_b = \begin{bmatrix} b^{\|} & b^{\perp} \end{bmatrix},$$

where the unit vectors $b^{\|}$ and $b_i^{\perp}$ are the columns of S_b, so that an element $\dot{s} \in T_s\mathcal{S}$ can be expressed in the new coordinates as

$$\dot{s}^b = S_b^{-1} \dot{s}.$$

Using the new coordinates, the power flows in the actuator model can be further analyzed by applying the coordinate change to (3.7). Expressing the flows to the $\mathbb{C}$-element in the new coordinates yields:

$$\begin{aligned} \dot{s}^b &= S_b^{-1} \dot{s} \\ &= S_b^{-1} \left(A(q,r)\dot{q} + B(q,r)\dot{r} \right) \\ &=: S_b^{-1} \left(\dot{s}_q + \dot{s}_r \right) \\ &= \begin{pmatrix} \dot{s}_q^{\|} \\ \dot{s}_q^{\perp} \end{pmatrix} + \begin{pmatrix} \dot{s}_r^{\|} \\ \dot{s}_r^{\perp} \end{pmatrix} =: \begin{pmatrix} \dot{s}^{\|} \\ \dot{s}^{\perp} \end{pmatrix}, \end{aligned} \tag{3.8}$$

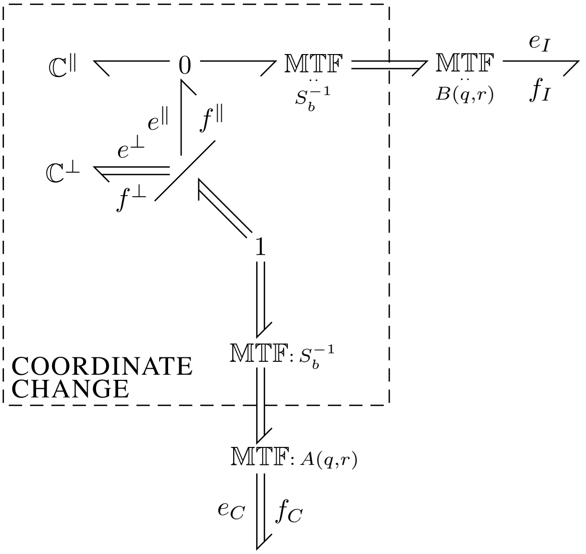

Figure 3.3: Virtual storage elements—Due to the change of coordinates, two separate $\mathbb{C}$-elements have been constructed, of which one is disconnected from the actuator output. The change of coordinates thus provides insights in the power flows of the model shown in Figure 3.1.

emphasizing that $\dot{s}_r^{\perp}$ is zero by construction of the new coordinates. By applying the change of coordinates, (3.8) defines two virtual $\mathbb{C}$-elements, replacing the original $\mathbb{C}$-element in Figure 3.1. In particular, (3.8) defines a one-dimensional element $\mathbb{C}^{\parallel}$ with state $s^{\parallel}$, and an element $\mathbb{C}^{\perp}$ of dimension $n_s - 1$, with state $s^{\perp}$. Figure 3.3 visualizes this construction by making explicit the Dirac structure and the change of coordinates using transformation elements (denoted by $\mathbb{MTF}$; see Chapter 8 for more details). It can be seen that the virtual $\mathbb{C}^{\perp}$-element is disconnected from the interaction port.

To find the power flows to $\mathbb{C}^{\parallel}$ and $\mathbb{C}^{\perp}$, the coordinate transformation needs to be applied to the efforts as well. In particular, since efforts are elements of $T_s^*\mathcal{S}$, the co-tangent space to $\mathcal{S}$ at s, the change of coordinates is applied as [42]

$$\begin{aligned}\left(\frac{\partial^T H_e}{\partial s}\right)^b &= \frac{\partial^T H_e}{\partial s} S_b \\ &=: \begin{pmatrix} e^{\parallel} & e^{\perp} \end{pmatrix}.\end{aligned} \tag{3.9}$$

It can be readily verified that the change of coordinates is power-continuous, obtaining the following equality from (3.8) and (3.9):

$$\langle e_S | \dot{s} \rangle = \langle e^{\parallel} | \dot{s}^{\parallel} \rangle + \langle e^{\perp} | \dot{s}^{\perp} \rangle.$$

Since the interaction port behavior is not explicitly modeled, $\dot{s}_r^{\|}$ in (3.8) is unknown. Instead, set

$$f^{\perp} = \dot{s}_q^{\perp} \quad \text{and} \quad f^{\|} = \dot{s}_q^{\|},$$

so that, from Figure 3.3,

$$\langle e_C | f_C \rangle = \langle e^{\|} | f^{\|} \rangle + \langle e^{\perp} | f^{\perp} \rangle, \tag{3.10}$$

or, equivalently,

$$P_C = P_C^{\|} + P_C^{\perp}. \tag{3.11}$$

With this, the power flows have been decomposed, providing a means to evaluate how much power supplied through the control port flows to the $\mathbb{C}^{\perp}$-element and the $\mathbb{C}^{\|}$ element.

Remark 3.2 Note that $P^{\|}$ is the power flow going to either the $\mathbb{C}^{\|}$-element or to the interaction port. How much power actually goes to either is dependent on the load and the task. Instead, $P^{\perp}$ will definitely not reach the interaction port. However, note that this decomposition of power flows in an instantaneous decomposition, since it is state-dependent, and thus does not provide information on the energy balance: $P^{\perp}$ may be temporarily stored and released at a later time. ◁

3.3 Measuring Energy Efficiency

The decomposition of the power flows, defined in (3.10) and (3.11), facilitates the notion of measuring energy efficiency of a variable stiffness actuator. In particular, considering that the $\mathbb{C}^{\perp}$-element is not connected to the interaction port, the quantity

$$\mu := \frac{P_C^{\perp}}{P_C},$$

can be defined, that indicates which fraction of the power P_C supplied via the control port is captured by the $\mathbb{C}^{\perp}$-element, and thus is not used to do work at the interaction port. Note that $\mu \in [0, 1]$, and that a lower value of μ indicates a higher efficiency in using the control power.

Remark 3.3 Mathematically speaking, the image of the map $B(q, r)$ defines a one-dimensional involutive distribution on $\mathcal{S}$. If the set $\{b^{\perp}\}$ is not empty, then for all configurations (q, r) the integral manifold of this distribution is a foliation on $\mathcal{S}$. On this foliation, the positive-definite energy function $H_e(s)$ will have a local minimum that does not necessarily coincide with the global minimum on $\mathcal{S}$. The difference in energy levels between the local and the global minimum is the energy captured by the $\mathbb{C}^{\perp}$-element. ◁

By calculating μ for the working principles described in Chapter 2, their performance can be compared. In particular, consider $\dot{q}$ achieving a desired rate of change $\dot{r}$ of the output position and a desired rate of change $\dot{K}$ of the apparent output stiffness. Then, given the current state s of the elastic elements, the quantity μ can be calculated. The details of these calculations can be found in Chapter 8. From these calculations is follows that the design incorporating the antagonistic springs (the principle described in Section 2.2.1) can attain lower values of μ than the designed with decoupled stiffness control (the principle described in Section 2.2.2). This can be explained by the design characteristic of the latter: by using a separate degree of freedom solely for pretensioning the internal springs, the power supplied for this degree of freedom is by definition captured by the elastic elements. Consequently, it can be concluded that this design will be less efficient when the stiffness needs to be frequently changed.

The third design principle, discussed in Section 2.2.3, provides an interesting advantage in the context of this power flow analysis. In particular, the following result is obtained.

Lemma 3.2 (Energy-efficient variable stiffness actuators) *For an actuator with* $n_q = 2$ *internal degrees of freedom, satisfying the conditions of Lemma 3.1,* $\mu = 0$ *for any choice of* $(\dot{r}, \dot{K})$*.*

Proof: For $n_q = 2$, Lemma 3.1 requires that $n_s = 1$, i.e. one internal elastic element. As a result, the image of $B(q, r)$ is the entire tangent space $T_s\mathcal{S}$, and therefore the set $\{b^\perp\}$ is empty, yielding $\mu = 0$. ☐

A prototype design for a variable stiffness actuator, satisfying Lemma 3.2 has been presented in [68, 64], and is discussed in detail in Chapter 7. The conceptual design is shown in Figure 3.4, and is based on a lever arm mechanism with variable effective lever length. If R is the radius of the pulley, let

$$s = R\varphi \tag{3.12}$$

be the elongation of the linear spring with stiffness k. For the sake of simplicity, assume that $\varphi \approx 0$, so that using the small angle approximation yields

$$\varphi = \frac{q_2 - x}{q_1}.$$

The output force F can then be approximated by

$$F = k\frac{R^2}{q_1^2}(q_2 - x),$$

from which the apparent output stiffness K is obtained as

$$K := \frac{\partial F}{\partial x} = k\frac{R^2}{q_1^2}.$$

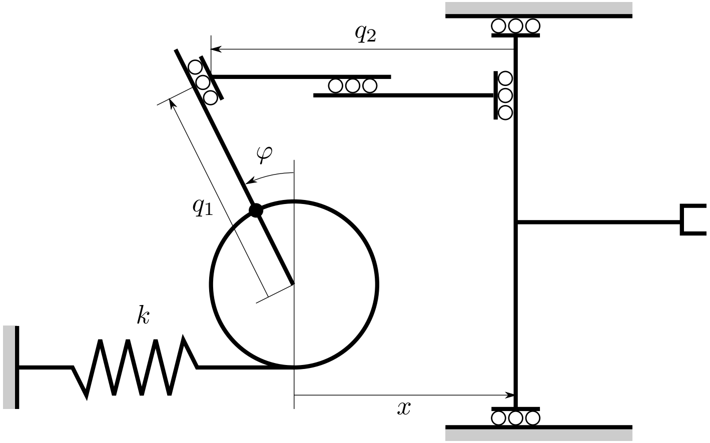

Figure 3.4: Working principle of an energy-efficient variable stiffness actuator—The effective length q_1 of the lever arm determines how the linear spring with stiffness k is perceived at the actuator output.

Indeed, this design satisfies the conditions of Lemma 3.2, because, from (3.12),

$$A(q, r) = \begin{bmatrix} -\frac{R}{q_1^2}(q_2 - x) & \frac{R}{q_1} \end{bmatrix},$$

for which a kernel exists for non-zero values of q_1. Variations on this principle are also used in the actuators presented in [34, 39], and was at the basis of the design presented in [26].

The power flow analysis presented in this chapter provides interesting insights in how energy is distributed between the variable stiffness actuator and the environment. In particular, it shows how power supplied through the control port can be captured by the internal elastic elements. Furthermore, Lemma 3.1 and Lemma 3.2 provided requirements for the designs of variable stiffness actuators, with the aim of avoiding energy being ‘locked up’. The next chapter will further explore the energetic behavior of variable stiffness actuators and present control strategies that exploit the energy-storing properties of the internal elastic elements.

CHAPTER 4

Energy-based Control Strategies

The previous chapter provided important insights in how power is distributed within a variable stiffness actuator. Given the energy-storing capabilities of elastic elements, the question arises how the power flows can be controlled in such a way that energy is internally stored by the elastic elements, for example when negative work is done at the interaction port.

The idea of including an elastic element in actuator designs, with the aim of temporary energy storage, was explored in [52, 51]. Because elastic elements store mechanical energy, there are no losses except those due to friction. Therefore, it is argued that this approach is preferable to trying to store energy in the electrical domain, since this would require a conversion step from the mechanical domain to the electrical domain, and these conversions between domains would induce additional losses. This chapter presents two control strategies for variable stiffness actuators, that take into account the energy storing capabilities of the internal elastic elements. It is shown that in this way it is possible to achieve more energy-efficient actuation, in particular for periodic motions.

4.1 Control of Power Flows

The first control strategy, discussed in detail in Chapter 9, controls the power flow through the control port. In particular, starting from the model depicted in Figure 3.1, by regulating the power flow through the control port, the control strategy regulates the energetic interaction between the internal elastic elements, represented by the $\mathbb{C}$-element, and the interaction port.

Consider a specific task that needs to be performed, e.g. tracking a reference trajectory $r^*(t)$ for a joint actuated by a variable stiffness actuator. The control objective is to find trajectories $q(t)$ for the internal degrees of freedom, such that, while performing the task, as much energy can be stored in the internal elastic elements when negative work is done at the joint side.

The dynamic behavior of the variable stiffness actuator, described by (3.1) and (3.4) can be written in state space form as follows:

$$\frac{\mathrm{d}}{\mathrm{d}t}\begin{bmatrix} s \\ q \\ r \end{bmatrix} = \begin{bmatrix} A(q,r) & B(q,r) \\ 1 & 0 \\ 0 & 1 \end{bmatrix} \begin{bmatrix} f_C \\ f_I \end{bmatrix}. \tag{4.1}$$

By defining the state $x := (s, q, r)$, (4.1) can be written more compactly as

$$\dot{x} = \sum_{i=1}^{n_q+1} g_i(x) u_i,$$

i.e. a drift-less system with input vector fields g_i and inputs u_i. In addition, define the output function

$$h_1(t) = e_I^* - e_I,$$

where e_I^* is the desired effort at the interaction port. It is assumed that the desired effort is known, for example by defining a reference trajectory $r^*(t)$ and a feedback control loop.

It can be readily verified that the relative degree of h_1 is $\rho = 1$, yielding:

$$\dot{h}_1 = \dot{e}_I^* - \sum_{i=1}^{n_q+1} \mathcal{L}_{g_i} e_I \cdot u_i, \tag{4.2}$$

where $\mathcal{L}_v f$ denotes the Lie-derivative of a function f along a vector field v. Rearranging (4.2) yields

$$\dot{h}_1 = \dot{e}_I^* - \left(\begin{bmatrix} \mathcal{L}_{g_1} e_I & \cdots & \mathcal{L}_{g_{n_q}} e_I \end{bmatrix} \dot{q} + \mathcal{L}_{g_{n_q+1}} e_I \cdot \dot{r} \right).$$

By defining

$$V = \begin{bmatrix} \mathcal{L}_{g_1} e_I & \cdots & \mathcal{L}_{g_{n_q}} e_I \end{bmatrix}, \tag{4.3}$$

and assuming that these Lie-derivatives do not vanish, the following result is obtained.

Lemma 4.1 (Nominal force control) *Given a desired interaction effort $e_I^*(t)$ and initial conditions such that $h_1(0) = 0$ and $\dot{h}_1(0) = 0$, the following control input realizes $h_1(t) = 0$:*

$$f_{C,n} = V^+ \left(\dot{e}_I^* - \mathcal{L}_{g_{n_q+1}} e_I \cdot f_I \right), \tag{4.4}$$

where V^+ denotes the Moore-Penrose pseudo-inverse of V.

The control input $f_{C,n}$ can be considered a nominal control input, as it does solve the control problem, but does not yet consider the energy stored in the elastic elements of the variable stiffness actuator. In order to investigate the regulation of the power flow through the control port, and in this way regulate the power flow between the $\mathbb{C}$-element and the interaction port, consider a variable stiffness actuator that satisfies the conditions of Lemma 3.1. Considering the state manifold $\mathcal{Q}$ for the configuration of the internal degrees of freedom, the characterizing property of these actuators is that a subspace of the tangent space to $\mathcal{Q}$ is defined by the kernel of the surjective map $A(q, r)$. Supposing the manifold $\mathcal{Q}$ to be Euclidean around q, $T_q\mathcal{Q}$ can be partitioned such that

$$T_q\mathcal{Q} = \ker A(q, r) \oplus D,$$

where D is an orthogonal subspace of $T_q\mathcal{Q}$ to $\ker A(q, r)$.[1] The dynamics of q are trivial, i.e. $\dot{q} = f_C$ for all $\dot{q} \in T_q\mathcal{Q}$, and therefore the control input f_C can be chosen such that, by Lemma 3.1, the energy in the internal elastic elements does not change.

Lemma 4.2 (Energy-efficient force control) *Consider a variable stiffness actuator satisfying the requirements of Lemma 3.1, and assume that the conditions stated in Lemma 4.1 are satisfied. Define two sets of local coordinates on* $T_q\mathcal{Q}$, *denoted by* a^1 *and* a^2, *such that:*

$$\begin{aligned} span\{a^1\} &= ker\ A(q, r), \\ span\{a^2\} &= D. \end{aligned}$$

Suppose $\mathcal{Q}$ *to be an Euclidean manifold around* q, *such that in the coordinates* $\{a^1, a^2\}$, *the metric* $\mathfrak{g}$ *has the following form:*

$$[\mathfrak{g}] = \begin{bmatrix} I^1 & 0 \\ 0 & \gamma I^2 \end{bmatrix}, \tag{4.5}$$

where I^1 *and* I^2 *are identity matrices of dimensions equal to those of ker* $A(q, r)$ *and* D *respectively, and* $\gamma : \mathcal{S} \to \mathbb{R}^+$ *is a function measuring the amount of energy stored in the elastic elements. Then, the control input*

$$f_{C,e} = V^\sharp \left(\dot{e}_I^* - \mathcal{L}_{g_{n_q+1}} e_I \cdot f_I \right), \tag{4.6}$$

where $V^\sharp$ *is the weighted pseudo inverse with respect to the metric* $\mathfrak{g}$, *tracks* $e_I^*(t)$ *while the power flow through the control port is inversely proportional to the amount of energy measured by* γ.

---

[1] The assumption of $\mathcal{Q}$ being Euclidean is necessary to weigh the elastic energy with respect to a reference. With an extension of the model with inertial properties or friction, it would be possible to make the construction completely coordinate-free without this assumption.

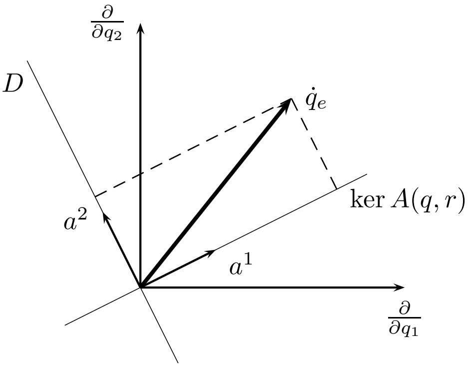

Figure 4.1: Realizing energy-efficient control—By decomposing the solution $\dot{q}_e$ in a component in the kernel of $A(q,r)$ and a component orthogonal to it, the amount of power flowing through the control port can be regulated by weighing each of these components in obtaining the solution to the control problem.

Lemma 4.2 is based on the properties of the weighted pseudo-inverse [3]. The principle is conceptually visualized in Figure 4.1, in which $(\partial/\partial q_1, \partial/\partial q_2)$ are the canonical coordinates for $T_q\mathcal{Q}$. By using the control input (4.6), the component of $\dot{q}_e = f_{C,e}$ corresponding to the coordinate a^2 will be weighed more as γ becomes larger. As a result, $\dot{q}_e$ will be closer to $\ker A(q,r)$, effectively closing off the power flow through the control port. In the limit case $\gamma \to \infty$, the flow $\dot{q}_e \in \ker A(q,r)$, and consequently $P_C = 0$. A meaningful choice for γ would be a function proportional to the value of the elastic energy function $H_e(s)$.

The control law proposed in Lemma 4.2 does achieve a control of power flows, but it does not consider the apparent output stiffness of the variable stiffness actuator. However, in some scenarios, it is required that a specific output stiffness is maintained. Given a desired stiffness K^*, a second output function can be defined:

$$h_2(t) = K^* - K. \tag{4.7}$$

It can be verified that, in general,[2] the relative degree of h_2 is $\rho = 1$, and therefore, from (4.7):

$$\begin{aligned} \dot{h}_2 &= \dot{K}^* - \sum_{i=1}^{n_q+1} \mathcal{L}_{g_i} K \cdot u_i \\ &= \dot{K}^* - \left(\begin{bmatrix} \mathcal{L}_{g_1} K & \cdots & \mathcal{L}_{g_{n_q}} K \end{bmatrix} \dot{q} + \mathcal{L}_{g_{n_q+1}} K \cdot \dot{r} \right). \end{aligned} \tag{4.8}$$

Then, the following extension is proposed.

---

[2] This is not the case only if the apparent output stiffness equals zero.

Lemma 4.3 (Stiffness regulation) *Assume initial conditions such that* $h_2(0) = 0$ *and* $\dot{h}_2(0) = 0$*. Let* $\dot{q}_k$ *be a solution to* (4.8) *for given* $\dot{K}^*$ *and* $\dot{r}$*. Then, by letting* $f_{C,k}$ *be a projection of* $\dot{q}_k$ *onto the kernel of* V*, as defined in* (4.3)*, the control law of Lemma 4.2 can be extended as follows:*

$$f_{C,e} \mapsto f_{C,e} + f_{C,k}, \tag{4.9}$$

thus regulating the stiffness towards the desired value, without interfering with the force control objective.

The essence of Lemma 4.3 is in projecting $\dot{q}_k$ onto the kernel of V. Because of this projection, K^* cannot be exactly tracked in case of disturbances. However, the extension prevents that the apparent actuator output stiffness deviates too much from the desired value, but at the cost of interfering with the metric (4.5). Chapter 9 presents numerical simulation results to illustrate these concepts. In particular, it is shown that, while all three control strategies (4.4), (4.6) and (4.9) can track a desired periodic motion and reject a disturbance, the energy-efficient control law (4.6) requires the least amount energy to do so. The controller with the stiffness regulation extension (4.9) requires less energy in rejecting the disturbance than the nominal control (4.4), but more energy than the energy-efficient control (4.6). This decrease in energy efficiency is traded-off against a regulation of the apparent output stiffness.

4.2 Embodying Desired Behavior

If a variable stiffness actuator is used to actuate periodic motions, the question arises if resonance-based control can be employed to achieve more energy efficient actuation. This idea was explored in [55], in which it was shown that the joint stiffness could be tuned to a constant optimal value to reduce energy consumption to a minimum. In Chapter 10, a control strategy is presented in which the dynamic behavior of the variable stiffness actuator is dynamically tuned to an optimal behavior, taking into account the energetic cost associated with changing the apparent output stiffness.

The proposed control strategy is based on the idea that a variable stiffness actuator basically behaves like a spring, but with variable stiffness, as illustrated in Figure 1.2. Therefore, instead of describing the configuration of the internal degrees of freedom by $q \in \mathcal{Q}$, it is shown that, under some assumptions detailed in Chapter 10, a change of coordinates exists such that the configuration of the internal degrees of freedom is described by two new quantities corresponding to the equilibrium position $\bar{r}$ and the output stiffness K. In particular, define

$$S : q \mapsto \tilde{q}, \quad \bar{q} := (\bar{r}, K),$$

where K is defined in (3.3) and $\bar{r}$ is defined as the minimizer of $H_e(s)$ through the kinematic map (3.5):

$$\bar{r} := \arg\min_r (H_e \circ \lambda)(q, r).$$

Using this change of coordinates and defining the state

$$x = (x_1, x_2, x_3, x_4) := (r, \dot{r}, \bar{r}, K),$$

the dynamics of a variable stiffness actuator, connected to a constant load of mass m, can be written in the form

$$\begin{aligned} &\dot{x} = f(x) + g_1 u_1 + g_2 u_1, \\ \text{with}\quad & \\ &\dot{x}_1 = x_2 \\ &\dot{x}_2 = \tfrac{1}{m} x_4 (x_3 - x_1) \\ &\dot{x}_3 = u_1 \\ &\dot{x}_4 = u_2 \end{aligned} \tag{4.10}$$

The control objective is to find control inputs (u_1, u_2) and initial conditions $x^\circ = x(0)$ such that

$$J = \int_0^\infty \tfrac{1}{2} \|x_3^\circ - x_3\|_{\bar{r}}^2 + \tfrac{1}{2} \|x_4^\circ - x_4\|_K^2 + \tfrac{1}{2} \|u\|_u^2 \, dt \tag{4.11}$$

is minimized for weighted 2-norms $\| \cdot \|_*$, to be defined hereafter. There are two parts to be distinguished in this criterion. The first part (the first two terms of the integrand) associates a cost to deviations of the actuator equilibrium position and stiffness from their initial conditions, while the second part (the third term) associates a cost to dynamic changes of these quantities. Essentially, minimizing J means trying to find a constant linear spring whose dynamic behavior is "close" to the desired behavior ("close" being defined by the minimum of J), and embedding this constant spring in the controlled dynamics of the variable stiffness actuator.

The norms in (4.11) should be defined by the performance limits of the variable stiffness actuator. For example, the norms $\| \cdot \|_{\bar{r}}$ and $\| \cdot \|_K$ measure displacements and could thus be based on the operational limits of the internal degrees of freedom. The norm $\| \cdot \|_u$ measures dynamic changes of the configuration of the internal degrees of freedom, and should thus have an energetic basis. In Chapter 10 it is proposed to use the mass matrix corresponding to the actuators used to control the internal degrees of freedom, expressed in the new coordinates.

Consider a desired periodic motion of the form

$$\begin{aligned} \dot{x}_1 &= x_2, \\ \dot{x}_2 &= \sigma(x_1) - \gamma, \end{aligned}$$

for some function σ and a constant γ. Defining

$$\Gamma(x) = \tfrac{1}{m} x_4 (x_3 - x_1) - \sigma(x_1),$$

it can be shown that $\Gamma(x)$ defines foliations $\mathcal{N}_\gamma$ on the state manifold $\mathcal{X}$:

$$\mathcal{N}_\gamma = \{ x \in \mathcal{X} \mid \Gamma(x) = \gamma \} .$$

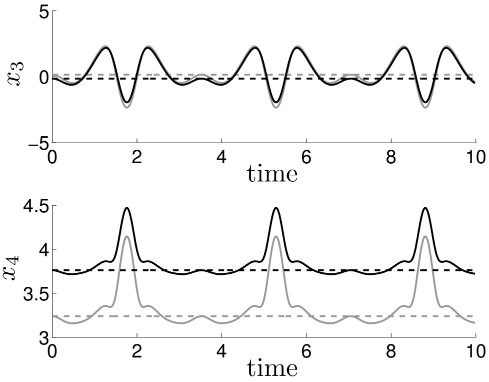

Figure 4.2: Optimal trajectories $x_3(t)$ and $x_4(t)$—The trajectories shown in black minimize the criterion J. These trajectories show smaller excursions with respect to their initial value when compared to a trajectory starting from arbitrary initial conditions (shown in grey).

By defining the error function $h_\gamma(x) = \Gamma(x) - \gamma$, the control objective can be reformulated to finding control inputs (u_1, u_2) such that, for initial conditions $x^\circ \in h_\gamma^{-1}(0) \subset \mathcal{X}$, the state trajectories $x(t)$ remain on the foliation while minimizing the criterion (4.11). By employing an output-nulling algorithm [42], it can be shown that these control inputs are given by

$$u = -A^\sharp \mathcal{L}_f \Gamma(x) + A^\perp(x) v,$$

with

$$A = \begin{bmatrix} \mathcal{L}_{g_1}\Gamma(x) & \mathcal{L}_{g_2}\Gamma(x) \end{bmatrix}.$$

The vector fields f and g_i are defined in (4.10), and the pseudo-inverse $A^\sharp$ should be calculated with respect to the metric defined through the norm $\|\cdot\|_u$. In this way the term $\|u\|_u^2$ in (4.11) is minimized. The annihilator $A^\perp$ allows the additional input v to achieve possible secondary control objectives without interfering with the main objective (see Chapter 10 for details). The two remaining terms in (4.11) must be minimized by choosing proper initial conditions x°. Unfortunately, this cannot be done analytically, and therefore it is proposed to solve this problem numerically by employing a line search along the remaining degree of freedom in choosing the control inputs to find the minimizers of J.

The proposed method is applied to a variable stiffness actuator tasked to track the trajectory generated by a Duffing oscillator of the form [27]

$$\ddot{x}_1 + \beta x_1 + \alpha x_1^3 = \gamma.$$

The norms $\|\cdot\|_{\bar{r}}$ and $\|\cdot\|_K$ were chosen identical, indicating no preference between changing $\bar{r}$ or K. However, the norm $\|\cdot\|_u$ is chosen such that dynamic changes in K are weighed four times more than dynamic changes in $\bar{r}$. Figure 4.2 shows the resulting trajectories for $x_3 = \bar{r}$ and $x_4 = K$ in black. Compared to the trajectories obtained by an arbitrary choice of initial conditions x_3° and x_4°, shown in grey, the resulting trajectories for the optimal x_3° and x_4° indeed show smaller excursions.

To evaluate the proposed optimization algorithm, the cost J defined in (4.11) is calculated over a time-span of 100 s. A value of $J = 141.374$ is found by the algorithm, while a fine-gridded brute force search over all possible initial conditions finds a minimum of $J = 141.316$, showing the effectiveness of the algorithm. To illustrate that a variable stiffness can yield more efficient actuation than a fixed stiffness actuator (i.e. a series elastics actuator), the optimization procedure is repeated with $u_2 \equiv 0$, thus enforcing a constant output stiffness. This yields a cost of $J = 158.397$ (brute force: $J = 155.998$), showing that even when a relatively higher cost is associated to changing the actuator stiffness, it is still meaningful to employ variable stiffness actuator for periodic motions.

CHAPTER 5

Application to Bipedal Walking

The previous chapters explored variable stiffness actuator design and performance through the development of a generalized model and a simplified representation of the load. This has resulted in important insights in the energetic behavior of the actuator connected to a load, although on a conceptual level.

This chapter explores the application of variable stiffness actuation to bipedal walking. It has been shown in [21] that a simple bipedal spring-mass model encodes a variety of gaits, for which it accurately reproduces the hip trajectories and ground reaction patterns observed in human walking. In further research, it was furthermore shown that the robustness of these gaits can be related to leg stiffness [44]. Since humans can also modulate their leg stiffness by muscle co-contraction, the extension of the bipedal spring-mass model with variable leg stiffness is an interesting research venue. Therefore, this chapter investigates how variable stiffness actuation can improve the robustness of the gaits of the bipedal spring-mass model. Furthermore, it will be shown that the control strategy developed for the bipedal spring-mass model is sufficiently robust to regulate the gait of extended models of bipedal walkers that include swing leg dynamics. In this way, a template controller is developed for control of bipedal walking robots.

5.1 Bipedal Walking with Compliant Legs

The model presented in [21] and shown in Figure 5.1, consists of a point mass m_h, restricted to move in the vertical plane, and two massless telescopic springs with stiffness k_0 and rest length L_0, representing the legs. It is essentially a bipedal spring-loaded inverted pendulum (SLIP) model. For appropriately chosen initial conditions, this system exhibits a passive walking gait, illustrated in Figure 5.2.

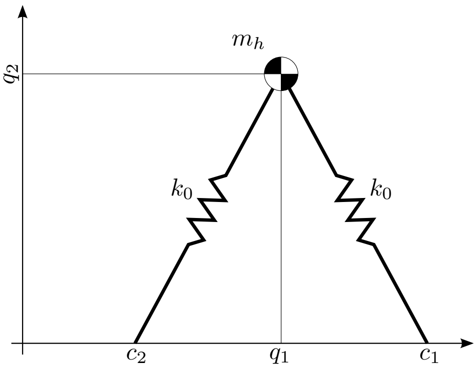

Figure 5.1: The bipedal SLIP model—The model consists of a point mass and massless telescopic springs with constant stiffness k_0, acting as legs.

During this gait, the system alternates between two phase: the single support phase, in which only one leg is in contact with the ground, and the double support phase, in which both legs are in contact with the ground.

The configuration variables $(q_1, q_2) =: q$ describe the planar position of the hip mass, and $(p_1, p_2) =: p$ the associated momentum variables. The phase, either single or double support, is determined by the vertical hip height q_2, with the transition from the single support phase to double support phase occurring when

$$q_2 = L_0 \sin(\alpha_0),$$

where α_0 is a suitably chosen angle of attack [21]. It is emphasized that the springs are massless, and thus influence the dynamics instantaneously at the moment of touchdown. The transition from the double support phase to the single support phase occurs when the trailing leg reaches its rest length, thus preventing that the springs pull from the ground, i.e. when

$$\sqrt{(q_1 - c_2)^2 + q_2^2} = L_0. \tag{5.1}$$

If the leading leg would lift-off, i.e. when the leading leg reaches its rest length, the gait is considered to have failed. The dynamic equations can be readily derived by considering the kinetic energy K and potential energy V of the hip mass, and the elastic energy stored in the springs, as detailed in Chapter 11. By defining the Hamiltonian energy function $H = K + V$, the dynamics can be written in Hamiltonian form as

$$\frac{\mathrm{d}}{\mathrm{d}t} \begin{bmatrix} q \\ p \end{bmatrix} = \begin{bmatrix} 0 & I \\ -I & 0 \end{bmatrix} \begin{bmatrix} \frac{\partial H}{\partial q} \\ \frac{\partial H}{\partial p} \end{bmatrix}. \tag{5.2}$$

Since the legs are massless, there are no energy losses associated with the phase transitions, and thus a constant energy level can be associated to a particular

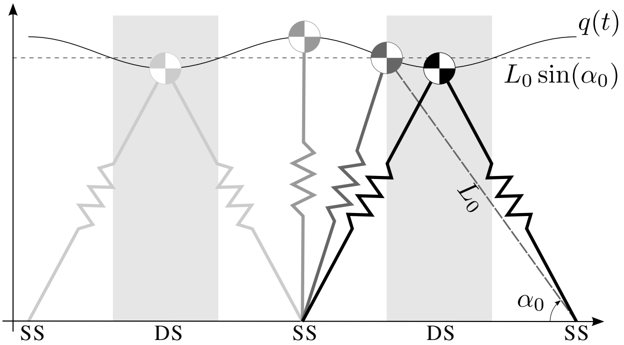

Figure 5.2: Gait trajectory of the bipedal SLIP model—For suitable initial conditions, the hip trajectory $q(t)$ results in a walking gait, alternating between single support (SS) and double support (DS) phases. The phase transitions are determined by the model parameters L_0 and α_0, corresponding to the rest length of the springs and the angle of attack at which the second leg appears upon entering the double support phase.

gait. As was shown in [21, 44], these energy levels encode the type of gait and the average walking speed. Furthermore, a constant energy level during nominal gait is interesting from a control perspective, as it implies that a gait controller can be designed that only requires to inject or remove power to the system when a disturbance occurs [69].

5.2 Gait Control using Variable Leg Stiffness

To provide the bipedal SLIP model with control inputs, consider the leg stiffness to be controllable. The extended model, called V-SLIP (for Variable SLIP), is shown in Figure 5.3. In this way, control action can be used to reach and maintain a desired gait. The total leg stiffness is $k_i = k_0 + u_i, i = 1, 2$, where k_0 is a constant leg stiffness and u_i is a controllable additional (e.g. parallel) stiffness. Note that k_i should be positive definite in order to be physically meaningful. As shown in detail in Chapter 11, the dynamics can be derived in port-Hamiltonian form analogously to the SLIP dynamics (5.2):

$$\begin{aligned} \frac{\mathrm{d}}{\mathrm{d}t}\begin{bmatrix} q \\ p \end{bmatrix} &= \begin{bmatrix} 0 & I \\ -I & 0 \end{bmatrix}\begin{bmatrix} \frac{\partial H}{\partial q} \\ \frac{\partial H}{\partial p} \end{bmatrix} + \begin{bmatrix} 0 \\ B \end{bmatrix} u \\ y &= \begin{bmatrix} 0 & B^T \end{bmatrix}\begin{bmatrix} \frac{\partial H}{\partial q} \\ \frac{\partial H}{\partial p} \end{bmatrix}, \end{aligned} \tag{5.3}$$

with $u = (u_1, u_2)$ the controlled leg stiffness. The input matrix B is given by

$$B = \begin{bmatrix} \frac{\partial \phi_1}{\partial q_1} & \frac{\partial \phi_2}{\partial q_1} \\ \frac{\partial \phi_1}{\partial q_2} & \frac{\partial \phi_2}{\partial q_2} \end{bmatrix},$$

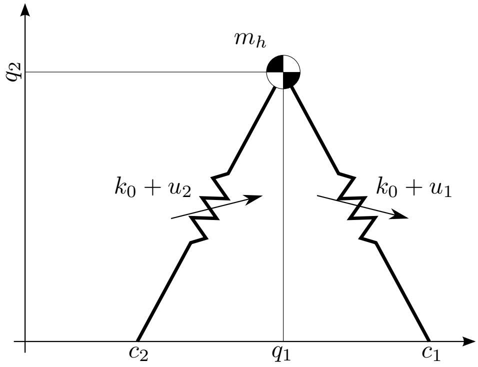

Figure 5.3: The V-SLIP model—By considering a variable leg stiffness $k_i = k_0 + u_i$, control inputs are provided that can be used to maintain a desired SLIP gait.

with

$$\phi_1 = -\tfrac{1}{2}(L_0 - L_1)^2 \quad \text{and} \quad \phi_2 = -\tfrac{1}{2}(L_0 - L_2)^2.$$

The control port is defined by the dual variables (u, y). Indeed, the dual product $\langle u|y\rangle$ has the units of power.

Since the bipedal SLIP model is energy conservative, the gait of this SLIP model is a good reference for the V-SLIP model. In particular, by the definition of the control inputs, it is possible for the controlled model to track the gait of the SLIP model with zero effort in the absence of disturbances. Defining the state $x = (q, p)$, let $x_{\text{SLIP}}(t)$ be a state trajectory of the bipedal SLIP model, i.e. a solution of (5.2). Assuming that the forward velocity $\dot{q}_1 > 0$, it is possible to parameterize $x_{\text{SLIP}}(t)$ by the forward position q_1, yielding a parameterized reference gait $(q_1^*, q_2^*, \dot{q}_1^*, \dot{q}_2^*)$, where $\dot{q}_i := \frac{1}{m_h} p_i$. It is not possible to exactly track such a reference gait, because the system is underactuated during the single support phase. However, the following result can be obtained.

Lemma 5.1 (V-SLIP Control) *Given a parameterized reference gait trajectory $(q_2^*, \dot{q}_1^*)$, define the error functions*

$$\begin{aligned} h_1 &= q_2^* - q_2, \\ h_2 &= \dot{q}_1^* - \dot{q}_1. \end{aligned}$$

A control strategy exists that, while considering the transitions between the single and double support phases, realizes:

$$\lim_{t\to\infty} q_2^*(q_1(t)) - q_2(t) = 0,$$

and, for some small $\varepsilon > 0$,

$$\lim_{t\to\infty} |\dot{q}_1^*(q_1(t)) - \dot{q}_1(t)| < \varepsilon.$$

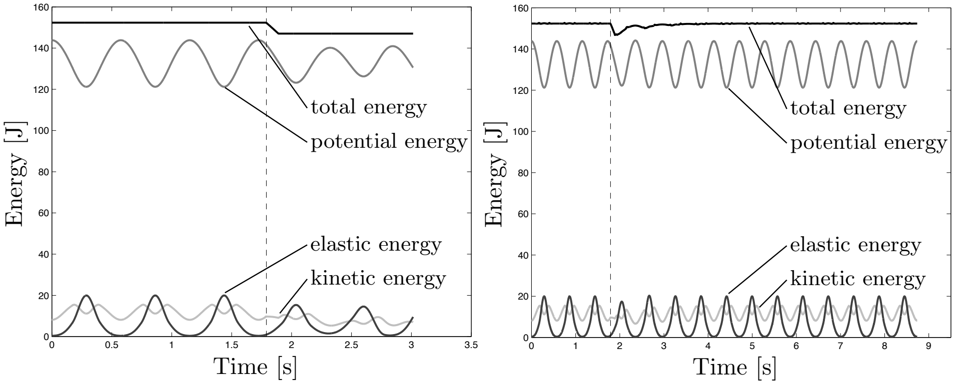

(a) Bipedal SLIP model.

(b) Bipedal V-SLIP model.

Figure 5.4: Energy balance of the SLIP and V-SLIP models—At the instance indicated by the dashed line, a disturbance is applied to both the SLIP and V-SLIP models. It can be seen that the V-SLIP model recovers successfully, returning to the constant energy level of the SLIP gait.

The details on the derivation of the control strategy and the stability proof are given in Chapter 11.

The effectiveness of this control strategy is illustrated in Figure 5.4. The plots show the energy balance of the bipedal SLIP and V-SLIP models, subjected to a disturbance. It can be seen that the disturbance is successfully rejected. The energy balance shows that indeed control effort is only required in rejecting the disturbance, not in nominal conditions, as exemplified by the constant energy levels before and after the disturbance. This result has been further investigated by applying varying disturbances at different moments throughout the gait [69]. It was shown that the control strategy is able to reject larger disturbances than the uncontrolled bipedal SLIP model.

While the proposed control strategy indeed realizes improved robustness levels for the bipedal SLIP model with variable leg stiffness, the model itself is still conceptual. In particular, since the legs are assumed to be massless springs, the dynamics of the swing leg are not considered. Therefore, more refined models are explored hereafter, which do incorporate swing leg dynamics. It will be shown that the control strategy presented in Lemma 5.1 can be easily extended to cope with the more complex dynamics of these models.

5.3 Influence of Swing Leg Dynamics

Just as the bipedal SLIP model, the V-SLIP model is purely conceptual. In particular, by assuming massless legs, the dynamics of the single support phase are not realistic, because influence of a swinging leg is not considered. To investigate how

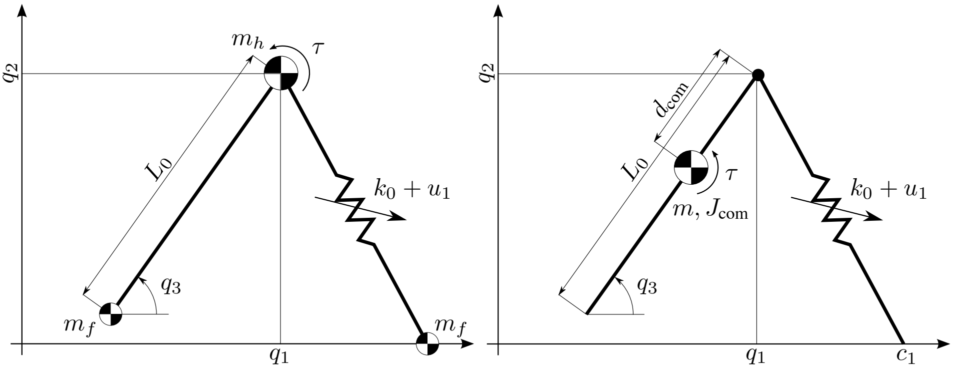

(a) V-SLIP model with feet (b) Simplified model

Figure 5.5: The V-SLIP model with swing leg—The V-SLIP model is extended with feet, modeled as a point mass m_f. Assuming that the swing leg is rigid, the swing leg dynamics can be modeled as a link with mass $m = m_h + m_f$ and a moment of inertia J_{com}.

swing leg dynamics influence the gait of the V-SLIP model, the model is extended to have feet, modeled as point masses with mass $m_f < m_h$. It is assumed that the feet do not slip or bounce once in contact with the ground, so that during the double support phase the V-SLIP dynamics (5.3) accurately describe the system behavior. During the single support phase, assuming that the swing leg can be considered a rigid link of length L_0, the system can be modeled as shown in Figure 5.5. The foot mass is taken together with the hip mass to a combined mass $m = m_h + m_f$ at a distance d_{com} from the hip, and an associated moment of inertia J_{com}. A torque τ provides an additional input during this phase, so the orientation q_3 of the swing leg can be controlled. The transition from the single support phase to the double support phase is now initiated when the foot touches the ground, i.e. when

$$q_2 = L_0 \sin(q_3).$$

The dynamic equations for the double support phase are the same as for the V-SLIP model, i.e. (5.3). With $(q_1, q_2, q_3) =: q$, $(p_1, p_2, p_3) =: p$, and the Hamiltonian energy function H, the dynamic equations for the single support phase can be derived using the Boltzmann-Hamel equations [15], yielding dynamic equations of the form

$$\begin{aligned} \frac{\mathrm{d}}{\mathrm{d}t}\begin{bmatrix} q \\ p \end{bmatrix} &= J \begin{bmatrix} \frac{\partial H}{\partial q} \\ \frac{\partial H}{\partial p} \end{bmatrix} + \begin{bmatrix} 0 \\ B \end{bmatrix} u \\ y &= \begin{bmatrix} 0 & B^T \end{bmatrix} \begin{bmatrix} \frac{\partial H}{\partial q} \\ \frac{\partial H}{\partial p} \end{bmatrix}, \end{aligned} \tag{5.4}$$

with $u = (u_1, \tau)$ the controlled leg stiffness and swing leg torque. The derivation

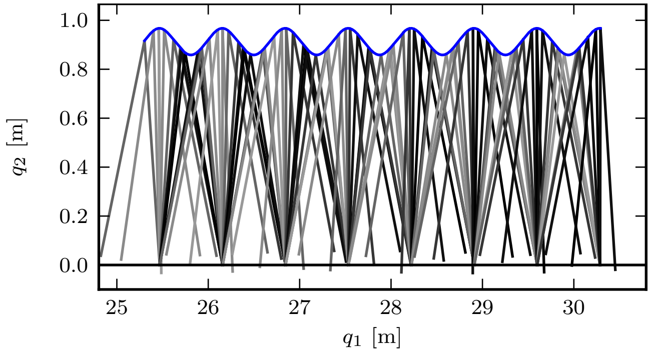

Figure 5.6: V-SLIP model with swing leg dynamics—The extended control strategy is able to stabilize the system to a SLIP reference gait, despite the disturbance introduced by the dynamics of the swing leg.

of the skew-symmetric matrix J and the input matrix B are explained in detail in Chapter 11. It is noted that the pair (u, y) again defines a power port for control action.

Let q_3^* be a reference function for the swing leg orientation, defined during the time interval

$$t_{\mathrm{lo}} \leq t < t_{\mathrm{lo}} + T_{\mathrm{swing}}, \tag{5.5}$$

with t_{lo} the time instant of lift-off defined by (5.1), and T_{swing} the nominal duration of the single support phase. Then, the result presented in Lemma 5.1 can be extended as follows.

Lemma 5.2 (Swing Leg Control) *Given reference state trajectories $(q_2^*, \dot{q}_1^*, q_3^*)$, define the error functions*

$$\begin{aligned} h_1 &= q_2^* - q_2, \\ h_2 &= \dot{q}_1^* - \dot{q}_1, \\ h_3 &= q_3^* - q_3. \end{aligned}$$

A control strategy exists that, while considering the transitions between the single and double support phases, realizes for some small $\varepsilon_1 > 0$:

$$\lim_{t\to\infty} |q_2^*(t) - q_2(t)| < \varepsilon_1,$$

and for some small $\varepsilon_2 > 0$,

$$\lim_{t\to\infty} |\dot{q}_1^*(t) - \dot{q}_1(t)| < \varepsilon_2,$$

and, during $t_{lo} \leq t < t_{lo} + T_{swing}$, for some suitable $\delta > 0$,

$$|q_3^*(t_{lo} + T_{swing}) - q_3(t_{lo} + T_{swing})| < \delta.$$

The reader is referred to Chapter 11 for details on the derivation of the control strategy. Figure 5.6 illustrates that the control strategy is indeed able to stabilize the gait of the walker.

As can be seen from Figure 5.6, the swing leg is allowed to swing through the ground, which is not realistic. To further refine the model, a knee is introduced, as shown in Figure 5.7. The knee introduces an additional degree, allowing the leg to be retracted during the single support phase, thus avoiding foot scuffing. Because the knee introduces only a kinematic relation between the hip and the foot, the leg configuration can be equivalently described by an orientation q_3, corresponding to the model depicted in Figure 5.5, and a length q_4.

Under the same assumption of no slip or bouncing occurring in the foot contact point, the V-SLIP dynamic equations (5.3) are still sufficient to describe the system behavior during the double support phase. Defining $q := (q_1, q_2, q_3, q_4)$, $p := (p_1, p_2, p_3, p_4)$, and the Hamiltonian energy function H, the dynamic equations for the single support phase take the form

$$\begin{aligned} \frac{\mathrm{d}}{\mathrm{d}t}\begin{bmatrix} q \\ p \end{bmatrix} &= \begin{bmatrix} 0 & I \\ -I & 0 \end{bmatrix}\begin{bmatrix} \frac{\partial H}{\partial q} \\ \frac{\partial H}{\partial p} \end{bmatrix} + \begin{bmatrix} 0 \\ B \end{bmatrix} u \\ y &= \begin{bmatrix} 0 & B^T \end{bmatrix}\begin{bmatrix} \frac{\partial H}{\partial q} \\ \frac{\partial H}{\partial p} \end{bmatrix}, \end{aligned} \tag{5.6}$$

where $u = (u_1, \tau_1, \tau_2)$, i.e. the controllable parts of the stance leg stiffness, and the torques collocated with q_3 and q_4. The input matrix B is given by

$$B = \begin{bmatrix} \frac{\partial \phi_1}{\partial q_1} & 0 & 0 \\ \frac{\partial \phi_1}{\partial q_2} & 0 & 0 \\ 0 & 1 & 0 \\ 0 & 0 & 1 \end{bmatrix},$$

with

$$\phi_1 = -\tfrac{1}{2}(L_0 - L_1)^2.$$

The pair (u, y) defines again the control port. The reader is referred to Chapter 11 for further details on the derivation of the dynamic equations.

In addition to q_3^*, let q_4^* be a reference function for the swing leg length, defined on the time interval (5.5). The result presented in Lemma 5.2 can be further extended as follows.

Lemma 5.3 (Swing Leg Control with Leg Retraction) *Given reference trajectories* $(q_2^*, \dot{q}_1^*, q_3^*, q_4^*)$*, define the error functions*

$$\begin{aligned} h_1 &= q_2^* - q_2, \\ h_2 &= \dot{q}_1^* - \dot{q}_1, \\ h_3 &= q_3^* - q_3, \\ h_4 &= q_4^* - q_4. \end{aligned}$$

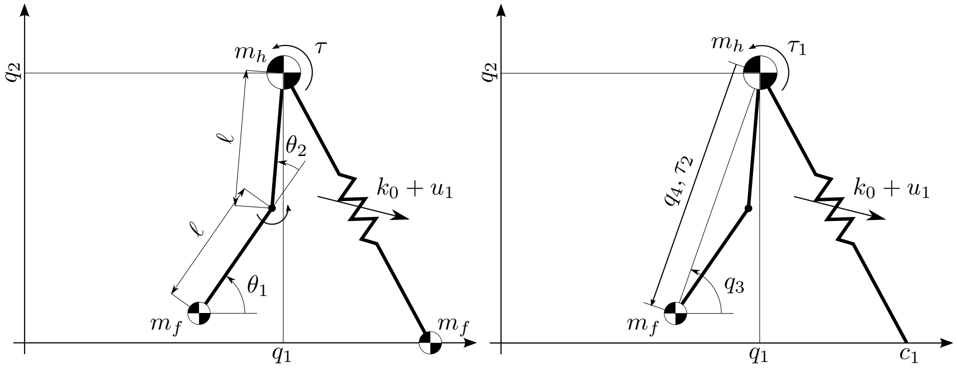

(a) V-SLIP model with feet and knee

(b) Simplified model

Figure 5.7: The V-SLIP model with retracting swing leg—The model is further extended with a knee, allowing the leg to be retracted during the swing and thus avoid scuffing the floor.

A control strategy exists that, while considering the transitions between the single and double support phases, realizes for some small $\varepsilon_1 > 0$*:*

$$\lim_{t \to \infty} |q_2^*(t) - q_2(t)| < \varepsilon_1,$$

and for some small $\varepsilon_2 > 0$*,*

$$\lim_{t \to \infty} |\dot{q}_1^*(t) - \dot{q}_1(t)| < \varepsilon_2,$$

and, during $t_{lo} \leq t < t_{lo} + T_{swing}$*, for some suitable* $\delta_1, \delta_2 > 0$*,*

$$\begin{aligned} |q_3^*(t_{lo} + T_{swing}) - q_3(t_{lo} + T_{swing})| &< \delta_1 \\ |q_4^*(t_{lo} + T_{swing}) - q_4(t_{lo} + T_{swing})| &< \delta_2 \end{aligned}$$

Chapter 11 provides more details on the derivation of the control strategy. Figure 5.8 illustrates the effectiveness of the control strategy.

5.4 Cost of Transport

The V-SLIP model was motivated by the energy-conserving properties of this model. In particular, the control strategy of Lemma 5.1 is formulated in such a way that, in nominal conditions, the natural dynamics of the SLIP model are reproduced, so that no control action is required. This is theoretically energy-efficient, but in extending the model with feet, this property has been lost. However, since the bipedal SLIP model is still anchored in the extended models, the control strategies for the extended models are still energy-efficient, because they exploit these

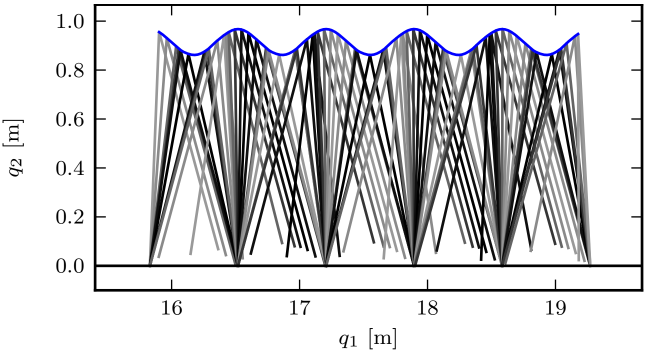

Figure 5.8: V-SLIP model with swing leg dynamics including leg retraction—The control strategy is further extended to retract the leg during swing, thus avoiding foot-scuffing, while still stabilizing the system to a SLIP reference gait.

embodies SLIP dynamics. This claim is illustrated by calculating the cost of transport [23, 30]. The cost of transport C, as defined in [30], is readily obtained trough the port-Hamiltonian formulation of the dynamic behavior (5.4) and (5.6):

$$C = \frac{1}{m_{\text{total}} g_0 \Delta x} \int_T |\langle u|y\rangle| \, \mathrm{d}t,$$

where m_{total} denotes the total mass, g_0 the gravitational acceleration, and Δx the distance travelled during the time interval T. Since the V-SLIP model is energy conservative, it can achieve $C \equiv 0$ in nominal conditions if the reference gait exactly matches the natural dynamics of the system. When the swing leg dynamics are included, the system is no long energy conservative. For the model shown in Figure 5.5, $C = 0.32$, and for the model of Figure 5.7, $C = 0.34$. Both these values are in the range of human cost of transport for various gaits [23]. This shows that bipedal gait control based on variable stiffness actuation, based on the template model shown in Figure 5.7, can serve as a template for energy-efficient control strategies for bipedal robots.

CHAPTER 6

CONCLUSIONS

Variable stiffness actuators form a class of actuators characterized by the property that their apparent output stiffness can be changed independently from the output position. This is realized by a number of internal elastic elements, and a number of internal degrees of freedom that determine how these elastic elements are perceived at the actuator output. This enables a robot equipped with such actuators to adapt to the environment by modifying their output impedance, while the integrated elastic elements open possibilities for temporary energy storage.

This thesis investigated models and analysis methods for variable stiffness actuators, presented new control strategies, and explored the application of variable stiffness actuation to bipedal locomotion. This chapter summarizes the results obtained in these three research areas, and provides an outlook for future work.

6.1 Discussion and Conclusions

Modeling and Analysis of Variable Stiffness Actuators

A generic port-based model for variable stiffness actuators has been presented. It was shown that this model can be applied to a variety of variable stiffness actuators designs, thus providing a uniform model for this class of actuators. Based on this model, an analysis method was developed, which provides insights on how the kinematics of the actuator design determines the power flows between the control port of the actuator, its internal elastic elements, and the environment. In particular, it was shown how three different working principles, that are at the basis of many variable stiffness actuator designs, perform in dynamically changing the apparent output stiffness. Furthermore, it was shown that using a variable transmission ratio to implement the stiffness regulation enables energy-efficient actuation by using the internal elastic elements for energy storage.

In deriving the model, a number of simplifying assumptions were made, which put the focus purely on the actuator kinematics. Furthermore, not all actuator designs can be readily captured by the model, due to strong nonlinearities in the design. Nonetheless, the model and the power flow analysis provided the basis for a comparison of energy-efficiency of actuator designs. Important insights in actuator design principles were gained, which resulted in paradigms for designing energy-efficient variable stiffness actuators.

Energy-Efficient Control Strategies

Based on the generic model for variable stiffness actuators, two novel control strategies have been presented, which exploited the energy storage capabilities of the internal elastic elements of the actuator. It was shown that it is possible to use these elastic elements as temporary energy storage when negative work is done at the actuator output. Specifically, one control strategy regulates the power flow through the control port, dependent on the amount of elastic energy available, while the second control strategy takes a resonance-like approach to controlling periodic motions by embodying the desired behavior as much as possible into the passive dynamics of the actuator.

Both control strategies have been demonstrated in numerical simulations, using simple models of variable stiffness actuators. As such, their practical applicability has not yet been proven. Therefore, these control strategies should be seen as a proof-of-concept, providing a basis for further development.

Bipedal Locomotion with Variable Stiffness Actuation

The bipedal spring-loaded inverted pendulum (SLIP) model, consisting of a point mass and massless telescopic springs representing the legs, accurately reproduces human gait characteristics. However, the model only captures autonomous, steady-state walking behavior. In this thesis it was proposed to make the leg stiffness variable (the V-SLIP model, for Variable SLIP), mimicking the human musculoskeletal capabilities, to provide the model with control inputs. Furthermore, a control strategy was presented that significantly improves the robustness of the gait against external disturbances, while maintaining the energy-conserving properties of the model.

By extending the V-SLIP model to include swing leg dynamics, a more realistic model was derived. The control strategy for the V-SLIP model has been extended to control the swing leg motion. This has shown that robust and energy-efficient locomotion is achievable using variable stiffness actuation. The extended model and corresponding control strategy provide a template for further research in this direction. A first attempt of applying these control strategies to an experimental setup are described in Appendix A.

6.2 Recommendations for Future Work

While this thesis aims to provide a complete line of research, the research in the field of variable stiffness actuation is far from finished. Variable stiffness actuators and their applications is a fairly new field, with many open questions. In the context of this thesis, a number of questions stand out, providing leads for future work.

Modeling and Analysis

- This thesis presented a generic port-based model, and it was shown that a large set of variable stiffness actuator designs can be fitted in this model by categorizing these designs on basis of their working principles. However, there are many more actuator designs that are not based on one of the three working principles identified in Section 2.2. Further research must reveal if these designs can also be accurately represented in the model, and if the power flow analysis can be applied.

- In the derivation of the port-based model, the focus has been on the working principles of the variable stiffness actuators. As such, internal friction, inertia, and other non-ideal effects have not been incorporated in the model. The model should be extended to incorporate these effects, and their influence of the actuator performance should be investigated in the context of the power flow analysis.

Control Methods

- The effectiveness of the control methods presented in this thesis has been demonstrated in numerical simulations. Experimental validation of these methods is an essential next step in their application to energy-efficient actuation methods using variable stiffness actuators.

- The control method presented in Section 4.1 does allow negative work to be done by one or more of the internal degrees of freedom. Nonetheless, it was shown that the control strategy is energy efficient. However, it should be investigated how this situation can be improved, for example by designing mechanisms that kinematically link internal degrees of freedom in a way that altogether avoids that negative work is done.

- The control method proposed in Section 4.2 is based on a coordinate transformation, relating the configuration of the internal degrees of freedom to the apparent output stiffness and equilibrium position of the actuator. In deriving the control strategy and the optimization criterion, it has been assumed that this change of coordinates is constant, which allowed the minimization of the proposed cost criterion. It should be investigated how this approach can be applied to variable stiffness actuator designs for which this change of coordinates is not constant.

Bipedal Locomotion

- Humans are capable of robust and energy-efficient locomotion on a wide variety of terrains. Prior research and the work presented in this thesis suggest that the compliancy of the human musculoskeletal system plays an important role in this, but further research is required to gain more knowledge. In particular, a better biomechanical understanding should be developed in how humans achieve energy-efficient walking on different terrains, while maintaining robust gaits.

- The template model of a bipedal walker, derived in Chapter 5, and the corresponding control strategy, assume walking in the sagittal plane. Extension to 3D walking is a logical next step, possibly also including other control approaches like foot placement strategies.

Other Recommendations

- Varying stiffness in real-time introduces very complex dynamics that are not yet fully understood. If variable stiffness actuators are to be applied reliably, a better understanding of these dynamics is required. In particular, if variable stiffness actuators are used in interacting robotic systems, it must be understood how stiffness variations influence the global dynamic behavior and the interaction behavior, and how nonlinear control techniques can be applied to shape these behaviors.

- Many of the ideas and concepts described in this thesis are theoretical in nature, demonstrated in numerical simulations. While many prototype variable stiffness actuators have been presented in literature, these actuators are still under development. In particular, dynamically changing the actuator output stiffness is difficult to achieve in highly-dynamic systems, mostly due to friction. Therefore, engineering effort should be directed to realizing more advanced prototypes, focussing on performance and reliability.

Part II

Selected Papers

CHAPTER 7

ENERGY-EFFICIENT VARIABLE STIFFNESS ACTUATORS

Ludo C. Visser, Raffaella Carloni, Stefano Stramigioli

in: *IEEE Transactions on Robotics*, 2011

7.1 Introduction

Humans can perform tasks in an unstructured and unknown environment, because, by tensioning the muscles, they can adjust the stiffness of their joints to a level appropriate for the task and the environment. In contrast, robots do not have this capability, which, in general, restricts them to perform predefined tasks in structured environments. However, in emerging robotic applications, in which robots need to cooperate with humans, such as prosthetics, rehabilitation devices, wearable and social robots, traditional stiff robot actuation is not suitable anymore. In particular, when the robot interacts with an unknown environment, instability can occur when the actuation of the robot is too stiff, leading to damage or even to injuries if humans are involved [28, 29].

Robots can be given similar capabilities as humans by using *variable stiffness actuators*. Variable stiffness actuators are characterized by the property that their apparent output stiffness, and thus the stiffness of the actuated joint, can be changed independently from the actuator output position. This is achieved by means of a number of internal compliant elements, such as springs, and a number of internal degrees of freedom that determine how the compliance is sensed at the actuator output. The internal mechanical compliance is important in realizing safe human-robot interaction, because it decouples the actuator inertia from the actuator output [5]. Moreover, in case of an impact, the elastic elements can absorb the impact energy, which gives the controller time to respond to the collision [13]. The energy storing properties of the elastic elements can also be used to achieve energy efficient actuation, by storing negative work [52, 51, 55].

Considering the wide range of possible applications of variable stiffness actuators, research effort in designing such actuators is increasing and various designs have been presented in the literature. In applications where the variable output stiffness is only considered for planned interaction with the environment, the compliance can be emulated by software, i.e., active compliance or impedance control [45]. On the other hand, passive (i.e., mechanical) compliance can be implemented in many ways. In the 'Jack Spring'$^{\text{TM}}$ actuator [32], the apparent output stiffness is varied by changing the number of active coils of the internal spring. Other actuators, e.g., VSA-II [46] and VS-Joint [75], change the apparent output stiffness by varying the pretension of the internal nonlinear springs. Other actuators, including the vsaUT, presented in earlier work [68], [64], the AwAS [34], the AwAS-II [35] and the HDAU [39], change the apparent output stiffness by changing the transmission ratio between the internal linear springs and the actuator output. In [9], the configuration of permanent magnets is used to emulate the compliance.

The paper is organized as follows. In Section 7.2, we give a motivation for our work, which aims at the realization of a new class of energy efficient variable stiffness actuators. In Section 7.3, we briefly introduce the port-based modeling framework, and, in Section 7.4, we use it to derive a generic port-Hamiltonian model for variable stiffness actuators. From the analysis of the model, in Section 7.5, we derive a number of kinematic properties that variable stiffness actuators should have in order to be energy efficient. We present a conceptual design and a prototype realization, that satisfies these properties, in Section 7.6. Simulation and experimental results, presented in Section 7.7, validate the working concept. In Section 7.8, a discussion on the results is given and concluding remarks are drawn in Section 7.9.

7.2 Motivation

In this work, we consider a class of variable stiffness actuators that have internally a number of elastic elements, usually springs, and a number of actuated degrees of freedom. It is this mechanical characteristic that allows to change the apparent output stiffness of the actuator independently from its output position. The apparent output stiffness K is defined as the ratio of the infinitesimal change of the actuator output force δF as a result of an infinitesimal displacement of the actuator output position δr, i.e.,

$$K := \frac{\delta F}{\delta r} \tag{7.1}$$

If we consider a variable stiffness actuator as a collection of elastic elements and ideal actuated degrees of freedom, i.e., the degrees of freedom are without mass and without friction, then the electrical energy supplied to the internal actuators can either be used to do work at the actuator output, or it can be internally stored in the elastic elements. For example, the energy is stored when the internal degrees of freedom are used to change the pretension of internal springs to achieve a different apparent output stiffness. However, in this case, the energy is irreversibly stored, in the sense that it cannot be used to do work at the output. This means that changing the apparent output stiffness has a negative impact on the energy efficiency of the actuator, as already observed in [62].

In robotic applications in which energy efficiency is of particular concern, all power supplied to a variable stiffness actuator should be used only to do work at the actuator output, and not to change the apparent output stiffness. Following this argument, by *energy efficient variable stiffness actuators*, we mean actuators for which the apparent output stiffness can be changed without injecting or extracting energy to and from the internal elastic elements.

The aim of this work is to find which kinematic properties variable stiffness actuators must satisfy to be energy efficient, according to the definition above. We use the port-based approach as a tool for this search, because it reveals how the kinematics determine the power flows inside the actuator, i.e., the power flows between the internal degrees of freedom, the internal elastic elements, and the actuator output. Moreover, the state of the elastic elements, from which we derive the definition of energy efficiency, is explicitly described in the model and can be intuitively used to derive the requirements on the kinematic structure. The analysis of the port-based model allows for the introduction of a conceptual design based on these requirements and for the realization of a prototype.

7.3 Port-based Modeling Framework

In this Section, we intend to briefly introduce the port-based modeling framework, which we use with the aim of providing more insights in the energy flows in variable stiffness actuators. For a more comprehensive treatment of port-based modeling and bond graphs, the reader is referred to e.g. [14, 50].

7.3.1 Port-based Modeling

Any physical system can be modeled in a port-based framework. A key element in this modeling framework is the concept of power conjugate variables, called *efforts* and *flows*. In the mechanical domain, flows are physically interpreted as velocities and efforts as forces. The dual product $\langle e|f\rangle$ of an effort e and a flow f yields power. A pair of effort and flow variables thus defines a power flow.

If f is an element of a real vector space $\mathcal{V}$, and e is an element of the dual vector space[1] $\mathcal{V}^*$, then we can define a subspace $\mathcal{D} \subset \mathcal{V} \times \mathcal{V}^*$, called *Dirac structure*, such

---

[1] Under coordinate transformations, efforts behave as co-vectors. However, for notational convenience, we write them as vectors in this work.

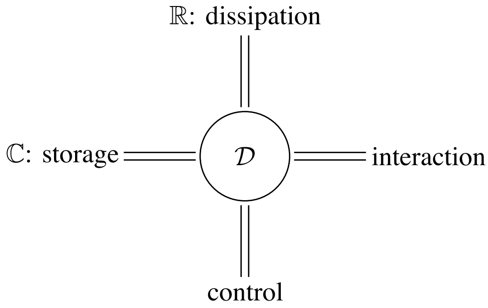

Figure 7.1: Network structure of a generic physical system—The Dirac structure $\mathcal{D}$ defines a power continuous connection between the ports. Internal energy storage is represented by the ℂ-element, and energy dissipation by the ℝ-element. The system interacts with the environment via the control port and the interaction port.

that

$$\langle e|f\rangle = 0, \quad \forall\,(f,e) \in \mathcal{D} \tag{7.2}$$

A Dirac structure defines a network topology, i.e., a distribution of power flows among the ports of the structure, and from (7.2) it follows that a Dirac structure is power continuous. Note that a Dirac structure is allowed to vary in time, as long as the power continuity is preserved.

Using a Dirac structure, we can model the behavior of the system by making explicit its network topology. The generic network topology is shown in Figure 7.1, where four separate power ports can be distinguished. The *interaction port* is available for interaction with the environment, i.e., (a composition of) other systems. The associated port variables are denoted by the pair (f_I, e_I). The *control port* is used for control action, with associated port variables (f_C, e_C). The port variables of the *storage port* are denoted by the pair (f_S, e_S) and are associated with the internal energy storage of the system, represented by a Hamiltonian energy function H. At this port, the power conjugate variables satisfy the energy balance

$$\frac{\mathrm{d}H}{\mathrm{d}t} = \langle e_S|f_S\rangle \tag{7.3}$$

Energy is dissipated via the *dissipation port*, with associated port variables (f_R, e_R) satisfying

$$\langle e_R|f_R\rangle \leq 0 \tag{7.4}$$

Often, a linear model of the dissipative element is used, and then the port variables are related as

$$f_R = -Re_R \tag{7.5}$$

with a positive semi-definite matrix $R = R^T \geq 0$.

The Dirac structure $\mathcal{D}$ defines the power continuous port interconnection. From the definition of a Dirac structure (7.2), it follows that

$$\langle e_S|f_S\rangle + \langle e_R|f_R\rangle + \langle e_I|f_I\rangle + \langle e_C|f_C\rangle = 0$$

Substituting (7.3), we have

$$\frac{\mathrm{d}H}{\mathrm{d}t} = -\langle e_R | f_R \rangle - \langle e_I | f_I \rangle - \langle e_C | f_C \rangle \tag{7.6}$$

i.e., the rate of change of the internal energy is determined by the amount of energy dissipated, and the power flow through the control and the interaction ports. It follows that the system is passive with respect to the input ports, i.e., the control port and the interaction port.

7.3.2 Input/Output Representation of Port-Hamiltonian Systems

The Dirac structure representation of a system, as given in the previous Section, does not consider causality. This representation is close to the physical reality, since causality is an artificial concept. However, often it is more convenient to consider a causal representation of the system dynamics, with respect to the *input port*, i.e., the composition of the interaction port and the control port. Therefore, we define the system state manifold $\mathcal{X}$, with coordinates x, and assume that it is a Poisson manifold and satisfies the integrability conditions [50]. Under these conditions, we can derive the input/output representation of the port-Hamiltonian system.

The Hamiltonian energy function $H : \mathcal{X} \to \mathbb{R}$ is defined as a smooth function on the state manifold $\mathcal{X}$. In addition, we consider the port interaction space W_x, which is a vector bundle over $\mathcal{X}$. The power conjugate variables (u, y) of the input port then belong to $W_x \times W_x^*$. Let ϕ_x denote a linear map from W_x to $T_x\mathcal{X}$ and ϕ_x^* its dual, and let $\mathcal{J}_x$ denote a Poisson tensorfield, which defines a fibre bundle morphism from $T_x^*\mathcal{X}$ to $T_x\mathcal{X}$. The port-Hamiltonian system can then be represented as

$$\begin{aligned} \dot{x} &= \mathcal{J}_x \,\mathrm{d}H(x) + \phi_x \, u \\ y &= \phi_x^* \,\mathrm{d}H(x) \end{aligned} \tag{7.7}$$

where $\mathrm{d}H(x)$ denotes the differential of the Hamiltonian energy function $H(x)$. The coordinate function x is the state of the system, and the port variables u and y can be considered as inputs and outputs of the system, respectively.

If we choose local coordinates on $\mathcal{X}$, we can write (7.7) as

$$\begin{aligned} \dot{x} &= J(x)\frac{\partial H}{\partial x}(x) + g(x)u \\ y &= g^T(x)\frac{\partial H}{\partial x}(x) \end{aligned} \tag{7.8}$$

where the skew-symmetric matrix $J(x)$ represents the network topology between the ports, and thus represents the Dirac structure. In local coordinates, it is also more apparent how the dissipative element defined in (7.5) can be included into the system dynamics. Indeed, by letting the pair (u, y) only represent the ports by

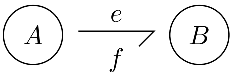

Figure 7.2: Interconnection of two port-Hamiltonian systems A and B - The power flow $\langle e|f\rangle$ is defined positive in the direction of the bond, i.e., the half arrow.

which the system interacts with other systems, i.e., the composition of the control port and the interaction port, the system dynamics are given by

$$\begin{aligned} \dot{x} &= \big(J(x) - R(x)\big)\frac{\partial H}{\partial x}(x) + g(x)u \\ y &= g^T(x)\frac{\partial H}{\partial x}(x) \end{aligned} \tag{7.9}$$

with $R(x) = R^T(x) \geq 0$ a positive semi-definite matrix.

7.3.3 Bond Graph Representation

The concept of power conjugate variables, and thus of power flows, lends itself for a compact graphical representation. In Figure 7.2, the interconnection of two port-Hamiltonian systems A and B is shown. The power flow between the two systems is represented by a *bond*, i.e., the half arrow. In particular, the power flow $\langle e|f\rangle$ is defined positive in the direction of the half arrow. In this example, the systems A and B can be port-Hamiltonian systems, as given in (7.9), or, on a more conceptual level, power continuous interconnection structures as defined in (7.2), energy storing elements as defined in (7.3) or energy dissipating elements as defined in (7.4).

Using the concept of bond graphs, we can graphically represent the concept of a port-Hamiltonian system of Figure 7.1, as shown in Figure 7.3, in which the multi-bonds indicate a multidimensional interconnection. Note that in order to comply with the power continuity constraint (7.2), all bonds must have the same orientation with respect to the Dirac structure.

7.4 Variable Stiffness Actuators as Port-Hamiltonian Systems

With the aim of getting more insights into the power flows between the variable stiffness actuator, the controller, and the actuator output, in this Section, we present a port based model of variable stiffness actuators. This model was first presented in [68], but we provide here an extension to include a load, and a more detailed analysis of its properties and behavior.

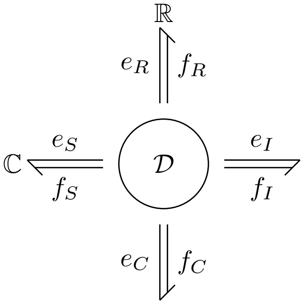

Figure 7.3: Bond graph representation of a port-Hamiltonian system—The $\mathcal{D}$ is the Dirac structure, the ℂ-element represents energy storage and the ℝ-element energy dissipation.

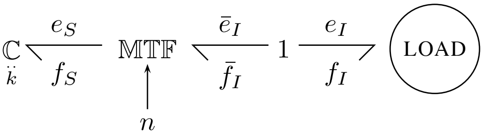

Figure 7.4: Model of a variable stiffness port—The external variable n modulates the transformer MTF and, therefore, determines how the linear spring, represented by the ℂ-element with elastic constant k, is sensed by the load.

7.4.1 Variable Stiffness Port

To get a better understanding of variable stiffness actuators, we first model the concept of a *variable stiffness port.* In this concept, the behavior of a linear spring is modulated by an external variable, so that at the port the spring appears to have a variable stiffness.

The concept is shown, using bond graphs, in Figure 7.4. The ℂ-element represents a linear spring and, therefore, a storage of elastic energy. Let s denote the state of the spring, i.e., its elongation or compression, then the elastic energy is given by $H_s(s) = \frac{1}{2}ks^2$, where k is the elastic constant of the spring. The power conjugate variables are

$$f_S = \dot{s}, \quad e_S = \frac{\partial H_s}{\partial s}(s) \tag{7.10}$$

The interaction port is characterized by the power conjugate variables (f_I, e_I), corresponding to the rate of change of the actuator output position r and the generated output force F, i.e., $(\dot{r}, F)$. The storage element and the interaction port are connected by means of a Dirac structure, realized by the combination of a MTF-element, i.e., a modulated transformer, and a 1-junction, a common flow connection.

The behavior of the $\mathbb{MTF}$-element is described by the relations

$$\begin{aligned} f_S &= n\,\bar{f}_I \\ \bar{e}_I &= n\,e_S \end{aligned} \tag{7.11}$$

where $n \in \mathbb{R}^+$ is the modulation variable. The $\mathbb{MTF}$-element is power continuous, i.e., $\langle \bar{e}_I | \bar{f}_I \rangle = \langle e_S | f_S \rangle$. The behavior of the 1-junction is given by

$$\begin{aligned} \bar{f}_I &= f_I \qquad (= \dot{r}) \\ \bar{e}_I &= -e_I \quad (= -F) \end{aligned} \tag{7.12}$$

Combining (7.10), (7.11) and (7.12), we can write

$$\begin{aligned} \dot{s} &= f_S = n\,f_I && (= n\,\dot{r}) \\ e_I &= -n\,e_S = -n\,\frac{\partial H_s}{\partial s} = -n\,k\,s && (= F) \end{aligned} \tag{7.13}$$

By considering infinitesimal changes in the actuator output force and position, from (7.13), we obtain that

$$\delta F = n^2 k\,\delta r$$

Using the definition of the stiffness given in (7.1), we obtain that the apparent output stiffness, as it is sensed by the load, is given by

$$K = n^2 k$$

It is observed that the apparent output stiffness is the constant stiffness of the spring, modulated by the external variable n. Thus, the output behavior can be modulated by changing n appropriately. Moreover, since n is an external variable and not a power variable, the output stiffness is changed in an energy free way, i.e., the energy stored in the spring is not changed due to modulation of n. It is this kind of behavior we wish to achieve with a variable stiffness actuator. However, it should be noted that, in this model, the maximum energy flow through the interaction port is limited by the initial energy present in the storage element. Therefore, in order to derive a model for an actuator with variable stiffness port behavior, a model with an additional power port is needed, so that additional energy can be supplied to do work on the load.

7.4.2 Variable Stiffness Actuators

In deriving a generic model for variable stiffness actuators, without loss of generality, we consider that:

- the actuator has a number n_s of internal elastic elements, described by state variables s and energy function $H_e(s)$, which describes the storage of elastic energy;

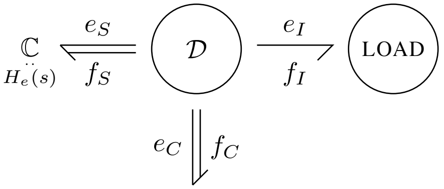

Figure 7.5: Generalized model of a variable stiffness actuator—The $\mathcal{D}$ is the Dirac structure, the internal elastic elements are represented by the multidimensional $\mathbb{C}$-element, described by the energy function $H_e(s)$. The internal degrees of freedom are actuated via the control port (f_C, e_C), while the interconnection with the load is via the output port (f_I, e_I).

- internally, there are a number $n_q \geq n_s$ of actuated degrees of freedom, with configuration variables q;
- the stiffness K, sensed at the actuator output port, is determined by the intrinsic properties, the state of the elastic elements and by the configuration of the internal degrees of freedom.

Moreover, in our model, internal friction and inertia are neglected, since the focus of the analysis is on the working principles of variable stiffness actuators and not on the optimization of the implementation.

In Figure 7.5, a bond graph representation of a generic model of a variable stiffness actuator is shown. In comparison with the model shown in Figure 7.4, some differences can be observed. The $\mathbb{C}$-element is now multidimensional and its port behavior is characterized by power conjugate variables

$$f_S = \dot{s}, \quad e_S = \frac{\partial H_e}{\partial s}(s) \tag{7.14}$$

where $H_e(s)$ is the storage of the elastic energy due to the internal elastic elements. The $\mathbb{MTF}$-element and 1-junction have been replaced by a generic Dirac structure, which determines how the power is distributed between the $\mathbb{C}$-element, the *interaction* or *output port* (f_I, e_I), and the *control port* (f_C, e_C). In particular, the output port is characterized by two power conjugate variables, which correspond to $(\dot{r}, F)$, i.e., the rate of change of the actuator output position r and the force F that the actuator exerts on the load. The control port is characterized by two power conjugate variables, which correspond to $(\dot{q}, \tau)$, i.e., the rate of change of the configuration of the internal degrees of freedom q and the torque τ generated by them.

Note that, via the control port, the configuration of the internal degrees of freedom q is controlled, which, together with the actuator output position r, determine the behavior of the Dirac structure. Using the internal degrees of freedom, power can be used to do work at the output port, while at the same time the apparent output stiffness can be changed.

Since the Dirac structure realizes a power continuous interconnection of the ports, it defines a constrained relation between the power conjugate variables. This constrained relation can be represented in a matrix expression as

$$\begin{bmatrix} f_S \\ e_C \\ e_I \end{bmatrix} = \underbrace{\begin{bmatrix} 0 & A(q,r) & B(q,r) \\ -A^T(q,r) & 0 & C(q,r) \\ -B^T(q,r) & -C^T(q,r) & 0 \end{bmatrix}}_{D(q,r)} \begin{bmatrix} e_S \\ f_C \\ f_I \end{bmatrix} \tag{7.15}$$

where the skew-symmetric matrix $D(q,r)$ represents the Dirac structure $\mathcal{D}$. Note that the Dirac structure may depend on the configuration variables q and r, but this is not necessary.

The sub-matrix $A(q,r)$ defines the relation between the rate of change of the configuration of the internal degrees of freedom q and the rate of change of the state s of the elastic elements. Similarly, the sub-matrix $B(q,r)$ defines the relation between the rate of change of the output position r and the rate of change of the state s of the elastic elements. In particular, if the state s is determined by the configuration q of the internal degrees of freedom and the actuator output position r via the kinematic relation

$$\lambda : (q,r) \mapsto s \tag{7.16}$$

then, by using (7.10), it follows that

$$A(q,r) := \frac{\partial \lambda}{\partial q}(q,r), \quad B(q,r) := \frac{\partial \lambda}{\partial r}(q,r) \tag{7.17}$$

The sub-matrix $C(q,r)$ defines a gyration effect between forces and velocities. However, such a gyration effect does not exist in the mechanical domain and, without loss of generality, it is assumed $C(q,r) = 0$. This implies that the Dirac structure (7.15) becomes

$$\begin{bmatrix} f_S \\ e_C \\ e_I \end{bmatrix} = \underbrace{\begin{bmatrix} 0 & A(q,r) & B(q,r) \\ -A^T(q,r) & 0 & 0 \\ -B^T(q,r) & 0 & 0 \end{bmatrix}}_{D(q,r)} \begin{bmatrix} e_S \\ f_C \\ f_I \end{bmatrix} \tag{7.18}$$

Observe that the skew-symmetry of the matrix $D(q,r)$ is a necessary condition for power continuity, as stated in (7.2)

$$\begin{bmatrix} e_S & f_C & f_I \end{bmatrix} \begin{bmatrix} f_S \\ e_C \\ e_I \end{bmatrix} = 0 \quad \Leftrightarrow \quad D(q,r) = -D^T(q,r)$$

As a result, via the matrices $A(q,r)$ and $B(q,r)$ the dual relations between the forces exerted by the internal elastic elements and the forces acting on the internal degrees of freedom and the output are defined.

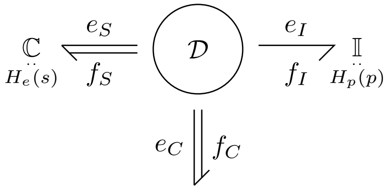

Figure 7.6: Generalized model of a variable stiffness actuator with a load—The internal elastic elements are represented by the multidimensional $\mathbb{C}$-element, described by the energy function $H_e(s)$. The internal degrees of freedom are actuated via the control port (f_C, e_C), while the interconnection with the load is via the output port (f_I, e_I). The $\mathbb{I}$-element represents the load with kinetic energy function $H_p(p)$, i.e., it models the inertial properties.

From (7.18), the rate of change of the energy is

$$\begin{aligned}\frac{\mathrm{d}H_e}{\mathrm{d}t}(s) &= \langle \frac{\partial H_e}{\partial s} | \dot{s} \rangle \\ &= \langle e_S | f_S \rangle \\ &= e_S^T \big(A(q,r) f_C + B(q,r) f_I \big) \\ &= -e_C^T f_C - e_I^T f_I\end{aligned}$$

Indeed, the rate of change of energy is determined by the power supplied via the control port and the output port, as stated in (7.6).

7.4.3 Variable Stiffness Actuator and a Load

To investigate the behavior of a variable stiffness actuator connected to a load, we use the port-based model shown in Figure 7.6. The $\mathbb{C}$-element, together with its power conjugate variables, and the control port are defined as in Section 7.4.2. The $\mathbb{I}$-element models the inertial properties of the load. In particular, it represents a storage of kinetic energy, given by the energy function $H_p(p) = \frac{1}{2m}p^2$, where p is the momentum of the load and m its mass. By the interconnection of this element to the output port, the port behavior is now given by

$$\begin{aligned} f_I &= \frac{\partial H_p}{\partial p}(p) \quad &(= \dot{r}) \\ e_I &= \dot{p} \quad &(= F) \end{aligned} \tag{7.19}$$

Note that, from (7.18),

$$\dot{p} = -B^T(q,r) e_S = -B^T(q,r) \frac{\partial H_e}{\partial s}(s) \tag{7.20}$$

In order to describe the Dirac structure of the variable stiffness actuator and the load in an input/output port-Hamiltonian system representation, as state of the system, we take

$$x = (s, p, q, r)$$

i.e., the state of the elastic elements, the momentum of the mass, the configuration of the internal degrees of freedom, and the actuator output position, respectively. If we consider the control port (f_C, e_C) as the input/output port of the system, i.e., $(u, -y)$, we can model this system in a input/output port-Hamiltonian form. We then obtain

$$\begin{aligned}\begin{bmatrix}\dot{s}\\ \dot{p}\\ \dot{q}\\ \dot{r}\end{bmatrix} &= \underbrace{\begin{bmatrix}0 & B(q,r) & 0 & 0\\ -B^T(q,r) & 0 & 0 & -1\\ 0 & 0 & 0 & 0\\ 0 & 1 & 0 & 0\end{bmatrix}}_{J(x)}\begin{bmatrix}\frac{\partial H}{\partial s}\\ \frac{\partial H}{\partial p}\\ \frac{\partial H}{\partial q}\\ \frac{\partial H}{\partial r}\end{bmatrix} + \underbrace{\begin{bmatrix}A(q,r)\\ 0\\ 1\\ 0\end{bmatrix}}_{g(x)} u \\ y &= \underbrace{\begin{bmatrix}A^T(q,r) & 0 & 1 & 0\end{bmatrix}}_{g^T(x)}\begin{bmatrix}\frac{\partial H}{\partial s}\\ \frac{\partial H}{\partial p}\\ \frac{\partial H}{\partial q}\\ \frac{\partial H}{\partial r}\end{bmatrix}\end{aligned} \tag{7.21}$$

where $H(s,p) := H_e(s) + H_p(p)$, i.e., the sum of the energy stored in the elastic elements and the kinetic energy stored in the mass.

The rate of change of the energy is given by

$$\begin{aligned}\frac{\mathrm{d}}{\mathrm{d}t}H(x) &= \frac{\partial^T H}{\partial x^T}\frac{\mathrm{d}x}{\mathrm{d}t}\\ &= \frac{\partial^T H}{\partial x^T}J(x)\frac{\partial H}{\partial x} + \frac{\partial^T H}{\partial x^T}g(x)u\\ &= \frac{\partial^T H}{\partial s^T}A(q,r)u\\ &= y^T u = -e_C^T f_C\end{aligned} \tag{7.22}$$

where we used the skew-symmetry of $J(x)$ and that $\frac{\partial H}{\partial q} = 0$. It is observed that indeed energy can be added to the system only via the control port (f_C, e_C).

7.5 Kinematic Properties of Energy Efficient Variable Stiffness Actuators

In this Section, we analyze the port-Hamiltonian model of a variable stiffness actuator, as given in (7.21), with the aim of deriving the kinematic properties that the actuator should have to be energy efficient. In particular, we derive the kinematic properties that allow the apparent output stiffness to be changed without changing the stored elastic energy.

Since the stored energy is a function of the state s of the elastic elements, we investigate the properties of the kinematic map (7.16). In particular, from (7.17) we have:

$$\dot{s} = A(q,r)\dot{q} + B(q,r)\dot{r}$$

that shows how the inputs $\dot{q}$ and the motion of the load $\dot{r}$ affect the state s. Therefore, in the next subsections, we investigate the influences of the matrices $A(q,r)$ and $B(q,r)$ on the energy of the system and on the apparent output stiffness.

7.5.1 Properties and Requirements for $A(q,r)$

When the variable stiffness actuator is connected to a load, the total energy of the system is determined by its initial energy and the energy supplied via the control port, as described by (7.22). From (7.22), if $\dim(\ker A(q,r)) \neq 0$, it follows that

$$\dot{H} = 0 \;\Leftarrow\; \dot{q} \in \ker A(q,r) \tag{7.23}$$

This condition states that, if the actuator has a mechanical structure such that the dimension of $\ker A(q,r)$ is not zero, some trajectories of the configuration variables q do not change the total energy of the system. In particular, these trajectories do not change the state s of the internal elastic elements. As shown in [66], if these trajectories of q do change the apparent output stiffness, then the actuator is energy efficient.

Mathematically, it is thus needed that the design of the actuator is such that there exist trajectories of q in the kernel of $A(q,r)$ that change the apparent output stiffness as desired. This implies that the mechanical design should include a redundancy in the kinematic structure that links the internal degrees of freedom to the elastic elements.

Note that condition (7.23) does not mean that changing the configuration variable q requires no energy at all. It is possible that in the actuation of the internal degrees of freedom opposite work is done, e.g., a positive power flow for actuating one degree of freedom is exactly balanced by a negative power flow for actuating a second degree of freedom. Therefore, even if (7.23) is satisfied, the negative work is lost due to dissipation, but the variable stiffness actuator is still energy efficient, according to the definition given in Section 7.2.

7.5.2 Properties and Requirements for $B(q,r)$

By using the kinematic map (7.16), the elastic energy $H_e(s)$ can be expressed in terms of the variables q and r, i.e.,

$$\bar{H}_e(q,r) := (H_e \circ \lambda)(q,r)$$

Using (7.20), the force F exerted on the load can therefore also be written in terms of q and r as

$$\begin{aligned}\bar{F}(q,r) &= -B^T(q,r)\frac{\partial \bar{H}_e}{\partial \lambda} \\ &= -\left(\frac{\partial \lambda}{\partial r}\right)^T \frac{\partial \bar{H}_e}{\partial \lambda}\end{aligned}$$

The apparent output stiffness (7.1) is a local property, i.e., it is defined only for a fixed $r = \bar{r}$ and, therefore, it is given by

$$\begin{aligned} K(q, r = \bar{r}) &= \left(\frac{\partial \bar{F}}{\partial \lambda} \frac{\partial \lambda}{\partial r} \right) \Big|_{r=\bar{r}} \\ &= B^T(q, \bar{r}) \frac{\partial^2 \bar{H}_e}{\partial \lambda^2} B(q, \bar{r}) \end{aligned} \tag{7.24}$$

where we used that $B(q, \bar{r})$ is not a function of r, and the minus sign is omitted by convention.

By inspecting (7.24), it can be seen that the apparent output stiffness can be varied by changing the configuration variables q if either $\frac{\partial^2 \bar{H}_e}{\partial \lambda^2}$ depends on q, or if $B(q, r)$ depends on q. However, the former option implies that the stored elastic energy changes to achieve a change of stiffness, which contradicts the requirements of energy efficiency. Hence, the latter option should be achieved [66].

From a mathematical point of view, the requirement on $B(q, r)$ implies that it should strictly depend on q for all configurations (q, r), i.e., the actuator must implement a variable transmission ratio. This means that the mechanical design should be such that the internal degrees of freedom modulate the transmission between the internal elastic elements and the output.

7.6 Design of an Energy Efficient Variable Stiffness Actuator

In this Section, we present the design of an energy efficient variable stiffness actuator, which satisfies the properties given in the previous Section, and thus is able to change the apparent output stiffness without changing the energy stored in the internal elastic elements. First, the working concept is explained, and then a prototype is presented.

7.6.1 Conceptual Design

The proposed design, depicted in Figure 7.7, realizes a variable stiffness actuator with a translational output motion. The functional principle is based on a linear spring, which is connected to the output via a lever arm of variable length. The effective length of the lever arm is controlled by the linear degree of freedom q_1, and thus q_1 determines how the spring is sensed at the output. The linear degree of freedom q_2 is used to control the actuator output position r. The design and control of this concept has been extensively described in [68].

The working principle satisfies the kinematic properties presented in the previous Section. The design is such that it presents a redundancy in how the two internal degrees of freedom are connected to the spring, i.e., $\operatorname{rank}(A(q, r)) < 2$, and the matrix $B(q)$ strictly depends on q, since the internal degrees of freedom modulate the transmission between the internal spring and the output.

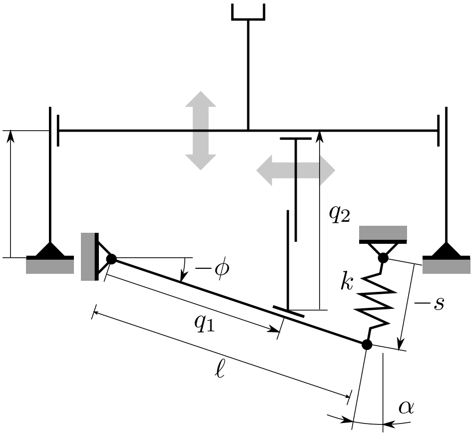

Figure 7.7: Conceptual design—The functional principle of the concept is a lever arm of variable length q_1, which connects the zero free length linear spring, with elastic constant k, to the output. The effective length of the lever arm, determined by the linear degree of freedom q_1, determines how the spring is sensed at the output. The actuator output position r is controlled by the linear degree of freedom q_2.

In order to build the port-based model of this actuator design, we analyze the kinematics. Let s denote the state of the linear zero free length spring, i.e., its compression or elongation, and be given by

$$s = \ell \sin\phi = \ell \, \frac{r - q_2}{q_1} \tag{7.25}$$

It is assumed that the design is such that it is allowed to take $\alpha = 0$, i.e., the length ℓ is large compared to s. Because the spring is linear, the energy function describing the energy stored in the spring is given by $H_e(s) = \frac{1}{2}ks^2$, where k is the elastic constant of the spring. Substituting (7.25) yields

$$\bar{H}_e(q, r) = \frac{1}{2}k\left(\ell \, \frac{r - q_2}{q_1}\right)^2$$

The rate of change of the state s is given by

$$\begin{aligned} \dot{s} &= \frac{\mathrm{d}}{\mathrm{d}t}\left(\ell \, \frac{r - q_2}{q_1}\right) \\ &= -\frac{\ell}{q_1}\begin{bmatrix}\sin\phi & 1\end{bmatrix}\begin{bmatrix}\dot{q}_1 \\ \dot{q}_2\end{bmatrix} + \frac{\ell}{q_1}\dot{r} \\ &= f_S \end{aligned}$$

As in (7.14), we define $e_S = \frac{\partial H_e}{\partial s}$, i.e., the force exerted by the spring. Then, the Dirac structure can be expressed by the skew-symmetric matrix $D(q, r)$ as (7.18)

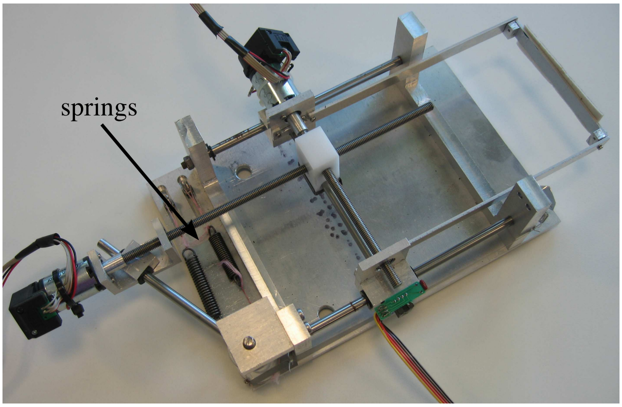

Figure 7.8: Prototype realization—The prototype is designed to closely resemble the concept shown in Figure 7.7. The zero free length linear spring has been replaced by an antagonistic spring setup acting directly on the rotation point of the lever arm, yielding the same desired behavior.

with

$$\begin{aligned} A(q,r) &= -\frac{\ell}{q_1}\begin{bmatrix}\sin\phi & 1\end{bmatrix} \\ B(q) &= \frac{\ell}{q_1} \end{aligned}$$

It can be seen immediately that the matrices $A(q,r)$ and $B(q)$ satisfy the properties listed in Section 7.5.

By using (7.20) and the kinematic map (7.16), the output force $\bar{F}(q,r)$ is given by

$$\bar{F}(q,r) = -\frac{\ell}{q_1}\,k\,\ell\frac{r-q_2}{q_1}$$

Using the definition of the actuator output stiffness (7.1) and (7.24), we find that, for this design, the output stiffness K is given by

$$K = \frac{\partial \bar{F}}{\partial r} = k\left(\frac{\ell}{q_1}\right)^2 \tag{7.26}$$

Equation (7.26) shows that the apparent output stiffness only depends on the degree of freedom q_1, i.e., the effective length of the lever arm. Therefore, the stiffness can be varied without changing the energy stored in the spring.

7.6.2 Prototype Realization

The conceptual design has been realized into a prototype, with the only aim of validating the functional principle, and therefore it is not optimized for performance [64].

The realization of the prototype, as depicted in Figure 7.8, closely corresponds to the concept depicted in Figure 7.7. The zero free length linear spring has been replaced by two extension springs, connected in an antagonistic setup to the rotation axis of the lever arm. The springs appear as a rotational spring at the rotation point, with an elastic constant $k = 0.68$ Nm/rad. Even if the behavior is the same as the zero free length spring, the added advantage is that the assumption $\alpha \approx 0$ is no longer necessary. Moreover, since the force exerted by the springs is applied to the rotation point, the actual length ℓ of the lever arm no longer appears in the kinematic equations.

The two linear internal degrees of freedom q_1 and q_2 are actuated by spindle drives with Maxon A-max brushed DC motors (Maxon Motor AG, Sachseln, Switzerland), so not to have motors exerting static torques. The kinematically constrained motions, as indicated in the conceptual design in Figure 7.7, are implemented using sliders. In particular, aluminum bars with teflon based sliding bearings are used.

7.6.3 Dynamic Model

For the prototype, a dynamic model is derived. Using this model, simulations can be performed to validate the concept, and can be compared with the experimental results. The dynamic model is derived using bond graphs and is shown in Figure 7.9, in which the generic Dirac structure of Figure 7.6 has been detailed. The multidimensional control port has been split into two separate control ports, each controlling one of the degrees of freedom q_1 and q_2. The lower two $\mathbb{MTF}$-elements implement the matrix $A(q,r)$ as

$$A(q,r) := \begin{bmatrix} A_1(q,r) & A_2(q,r) \end{bmatrix} = \frac{\ell}{q_1} \begin{bmatrix} \sin\phi & 1 \end{bmatrix}$$

The subsystems labeled M_1 and M_2 model the relevant dynamics of the spindle drives, including the dynamic properties of the Maxon motors powering them, as specified by the data sheets. The third $\mathbb{MTF}$-element implements the matrix $B(q) = -\frac{\ell}{q_1}$.

The 0-junction represents a power continuous common effort connection and, for N connected bonds, is described by

$$e_1 = \cdots = e_N, \quad \sum_{i=1}^{N} f_i = 0,$$

Together with the three $\mathbb{MTF}$-elements, the 0-junction implements the Dirac structure as it is given in (7.18). We note that, in Figure 7.9, the minus signs are introduced to comply with (7.18) and the causality of the 0-junction, but this does not affect the behavior described by the bond graph.

As was done in Section 7.4, the load is modeled as a mass, rigidly connected to the actuator output. The 1-junction represents a power continuous common flow

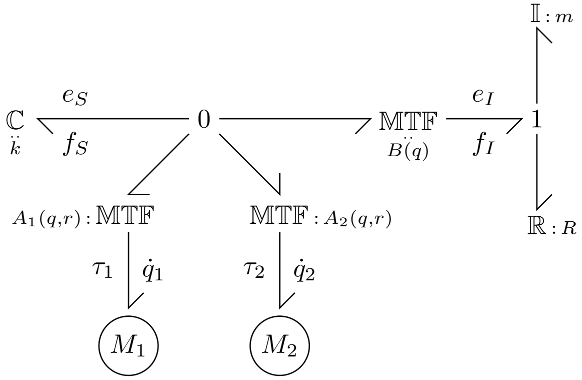

Figure 7.9: Bond graph based model of the prototype design—The various $\mathbb{MTF}$-elements and the 0-junction implement the Dirac structure, as given in (7.18). The $\mathbb{I}$-element and $\mathbb{R}$-element model the inertial and frictional properties, respectively. The subsystems M_1 and M_2 model the dynamic properties of the spindles drives that actuate the degrees of freedom q_1, q_2.

connection and, for N connected bonds, is described by

$$f_1 = \cdots = f_N, \quad \sum_{i=1}^{N} e_i = 0$$

The inertial properties of the load are modeled with the $\mathbb{I}$-element, defined in (7.19), with $m = 0.06$ kg. In addition, the frictional properties are modeled by a linear $\mathbb{R}$-element, as defined in (7.5). The friction coefficient is experimentally estimated to be $R = 20$ Ns/m. The value of the friction coefficient is high due to friction of the sliders that constrain the output motion.

7.7 Simulation and Experiments

In this Section, we validate the working principle of the prototype design, both in simulations and in experiments.

In order to have commensurable data, the same controllers for the degrees of freedom q_1 and q_2 are used both in simulation and in the experiments. In particular, the dynamic model presented in Figure 7.9 has been implemented in the 20-sim simulation software (Controllab Products, Enschede, The Netherlands), and using this model, PID controllers are designed to control the velocities $\dot{q}_1$ and $\dot{q}_2$. Using the 20-sim 4C tool-chain, these controllers can be directly exported to C code, which can run on an external controller board to actuate the experimental setup.

Two experiments are performed. The first one aims at showing that the kinematic structure of the actuator is energy efficient, and therefore that the apparent output stiffness of the actuator can be varied without changing the energy in the internal springs. In the second experiment, the aim is to show that the mechanical design of the actuator is such that the control energy, corresponding to the power flow in the control port, is used only to realize the motion of the output, without storing any energy in the internal springs.

7.7.1 Static Output Stiffness

In order to show the efficiency of the kinematic structure, the actuator is required to vary the apparent output stiffness, while the energy in the springs remains constant. This can be achieved by loading the springs and then varying the internal degrees of freedom while satisfying (7.23).

Due to its definition (7.1), the stiffness cannot be measured directly. However, as the stiffness is defined as a small variation of the output force due to a small variation of the output position, stiffness can be experienced by measuring the output force $\bar{F}$ for various settings of q_1 at fixed output positions. Indeed, for the specific design, due to (7.26), a change in q_1 corresponds in a change in the apparent output stiffness.

The experiment is as follows. The actuator output r is fixed and the degree of freedom q_1 is set to a distance of 0.076 m from the rotation point of the lever arm. Then, the degree of freedom q_2 is set such that the springs are loaded and $\phi = 0.15$ rad. Then, q_1 is moved towards the rotation point in 5 mm increments, until the final position of $q_1 = 0.026$ m is reached. Simultaneously, q_2 is actuated satisfying (7.23), so that ϕ and thus $\sin\phi$ are constant. After each increment of q_1, the output force is measured. From (7.18), and the actual dimensions of the prototype, the output force is given by

$$\bar{F}(q_1, r = \bar{r}) = \gamma \cdot q_1^{-1} \tag{7.27}$$

with $\gamma = k \sin\phi = 0.101$ obtained from analyzing the kinematics of the design. A typical experiment is shown in Figure 7.10, where we plot the measured values of ϕ and q in solid lines and the set-points for ϕ and q_1 in thick grey lines.

Figure 7.11 presents the results. The solid line represents the theoretic output force curve, given by (7.27). The open square markers represent the simulation results. Since the output force is measured in steady state conditions, only the kinematic parameters of the mechanism are relevant, and thus it is expected that simulation and theory give the same results.

The solid markers represent the experimental results. At each of the eleven set-point positions q_1, fifteen independent force measurements have been performed in steady state conditions. The markers represent the average of the measurements at a particular position q_1, and the vertical bars indicate the $1\,\sigma$ standard deviation of the measurements. It can be seen that, except for the measurements for $q_1 = 0.076$ m, the measurements are within $1\,\sigma$ of the theoretic curve. The deviation for $q_1 = 0.076$ m can be explained by the stiction present in the system, which causes the output slider to remain in a certain position for small output forces $\bar{F}$. By

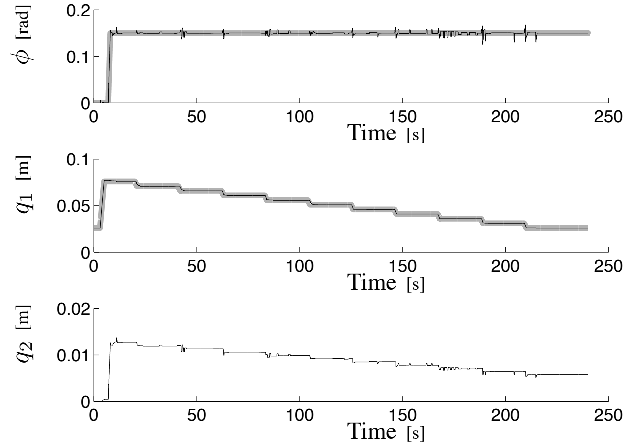

Figure 7.10: Output force measurement experiment—The internal springs of the actuator are loaded, such that $\phi = 0.15$ rad. The degree of freedom q_1 is varied along its configuration range, while q_2 is varied while satisfying (7.23). The result is that ϕ is kept constant and thus that the energy stored in the springs does not change during the experiment. The thick grey lines indicate the set-point values for ϕ and q_1, while the solid black lines represent the measured values.

this observation, the measurements for $q_1 = 0.076$ m are discarded. Then, for the remaining measurements, a least square curve fit to the averaged values results in

$$\bar{F}(q_1, r = \bar{r}) = 0.107 \cdot q_1^{-0.99} \tag{7.28}$$

with a residual of $\rho^2 = 0.97$. The experimental curve closely matches the theoretic curve (7.27). These results show that the prototype works in an energy efficient way as was derived from theory, and that indeed the apparent output stiffness can be changed without changing the energy stored in the internal springs.

7.7.2 Dynamic Actuation

In the second experiment, a load is connected to the actuator. The aim is to show that, when the apparent output stiffness is kept constant, work can be done on the load while no energy is stored or extracted from the springs. This implies that, when the load is not accelerated, there is no power flow to the springs.

The experiment is as follows. A mass of $m = 0.06$ kg is rigidly attached to the actuator output. Then, starting from the initial output position $r = 0$ m, a desired set-point value of $r = 0.03$ m is provided. The degree of freedom q_2 is used to achieve this displacement, while q_1 is kept constant so the apparent output stiffness is constant.

The results of both simulation and experiment are presented in Figure 7.12. The dashed lines represent simulation data, obtained using the dynamic model

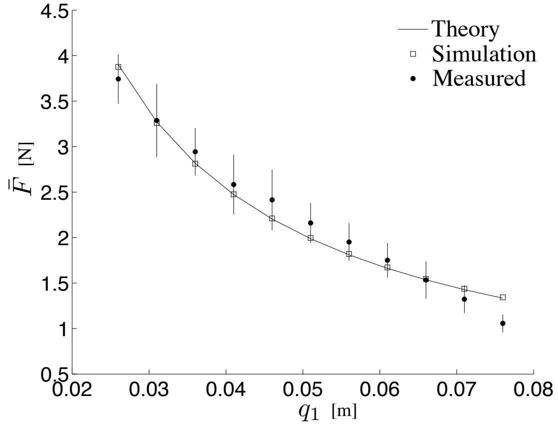

Figure 7.11: Measured output force—The solid curve is the theoretic curve (7.27). The open squares represent the measurements performed in simulation, using the dynamic model derived in Section 7.6. The solid dots indicate the average of experimentally measured values, and the vertical bars indicate the measurement standard deviation.

presented in Section 7.6, while the solid lines indicate data obtained from experiments with the prototype setup. When the mass is accelerated, the springs are compressed due to the inertial properties of the load. However, when the mass reaches the desired position, and is no longer accelerated, the springs have also returned to their rest length and thus no energy is left in the springs. The oscillations in the experimental curve for ϕ are due to stiction in the sliders supporting the output motion.

It can be observed that, although in simulation the device responds faster to the set-point change, the response is similar and the settling time is of the same order of magnitude for both the model and the prototype. Despite the differences in performance, the results confirm the working principle of the concept design.

7.7.3 Results

The experimental results validate the working principle of the conceptual design presented in Section 7.6. In particular, the first experiment has shown that indeed the concept is able to change the apparent output stiffness while keeping the energy stored in the springs constant. Even if this test was performed in static conditions, the results clearly validate the concept, as is illustrated by the close match between the theoretic curve (7.27) and the experimentally obtained curve (7.28). The high stiction forces present in the current realization did not allow for dynamic stiffness changes.

In the dynamic experiment, it was shown that when a load is actuated, all the power supplied by the controllers of the internal degrees of freedom is used to do

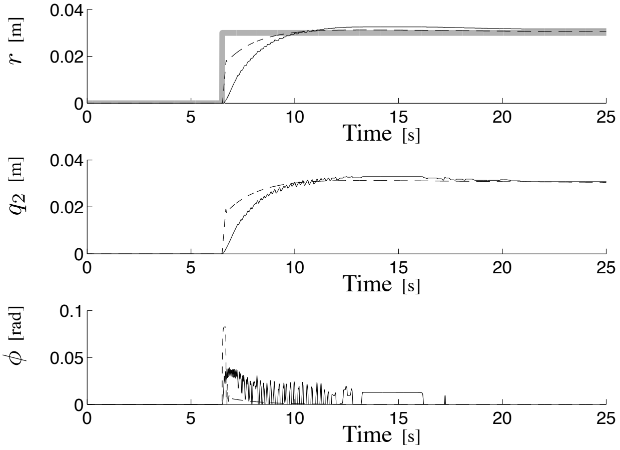

Figure 7.12: Output displacement experiment—A load of $m = 0.06$ kg is displaced from $r = 0$ m to $r = 0.03$ m, using the degree of freedom q_2. The grey thick line is the desired output position, while the simulation and experimental results are shown using the dashed lines and continuous lines, respectively. While the mass is accelerated, some energy is stored in the springs, but this energy is completely released after acceleration.

work at the output.

The two experiments show that a proof of concept of an energy efficient variable stiffness actuator design has been realized.

7.8 Discussion

In this work, we started from a formal mathematical model of variable stiffness actuators. From there, we derived kinematic properties, which guarantee that the apparent output stiffness can be changed without changing the energy stored in the internal elastic elements. In particular, it was found that there should be an internal redundancy and a modulated transmission between the internal elastic elements and the output. This was illustrated with a conceptual design, based on a lever arm of variable length. The realized prototype validated the working principle of the concept.

The analysis of Section 7.5 can also be applied to variable stiffness actuator designs presented in literature. In a previous work, we showed that, for actuator designs that use a pretension mechanism, the change of the apparent output stiffness is not energy efficient [66]. Any design based on the antagonistic principle, e.g. the actuator presented in [46], does not satisfy the requirements on the matrices $A(q, r)$ and $B(q, r)$, and is thus not energy efficient. Also the design presented in [75], which also uses pretension to change the apparent output stiffness, does not achieve energy efficiency for the same reasons. The designs presented in [34, 35] and [39] do satisfy the conditions for both $A(q,r)$ and $B(q,r)$. In fact, these designs present a variation of the lever arm concept presented in Section 7.6.

An important observation we made regarding the prototype concerns stiction. Even though performance was not a criterion in designing the prototype, and hence it may be assumed that friction and stiction may be reduced by an improved design, the concept of the lever arm of variable length is inherently hindered by stiction and friction forces, which are magnified by the springs forces. Therefore, any design based on the lever arm concept will suffer from stiction and friction, especially in loaded conditions. This can be avoided by using a rotational equivalent of the lever arm, i.e., a continuous variable transmission. Using such a transmission in combination with a rotational spring also avoids the transformation between linear and rotational motion.

7.9 Conclusions

In this work, we presented and validated a design concept for an energy efficient variable stiffness actuator. Starting from the port-Hamiltonian modeling paradigm, a generic port-based model of variable stiffness actuators was derived, which provides valuable insights in the power flows between the controller, the actuator and the load. From an analysis of this model, kinematic properties were derived that a variable stiffness actuator design must satisfy to allow changes of the apparent output stiffness without any variation of the energy in the internal elastic elements. Based on these properties, a concept design was presented. The working principle of the concept was validated both in simulation and in experiments with a prototype realization. Analysis of the prototype revealed how improvements in performance can be made, and some considerations for future designs were presented.

CHAPTER 8

VARIABLE STIFFNESS ACTUATORS: A PORT-BASED POWER FLOW ANALYSIS

Raffaella Carloni, Ludo C. Visser, Stefano Stramigioli

in: *IEEE Transactions on Robotics*, 2012

8.1 Introduction

In applications, in which robots need to interact with the environment or with humans, if the actuation is too stiff, instability can occur during the interaction, leading to possible damage of the robot, or even to injuries to humans. The instability can be effectively dealt with by using impedance control strategies [31]. However, since the reliability of this approach depends on software implementation, a mechanical compliance can be added in the robot actuation to ensure intrinsic safe interaction. By making this compliance variable, and thus realizing *variable stiffness actuators*, the apparent stiffness of the robot can be tuned to a specific task, and it is possible to achieve the trade-off between precision of motion and robustness [5, 1]. Given the broad range of possible applications of variable stiffness actuators, the research efforts in designing such actuators is increasing.

Many different designs have been presented, based on different working principles [59]. For example, 'Jack Spring'$^{\mathrm{TM}}$ varies the number of active coils of an internal spring [32], and the actuator presented in [9] changes the configuration of permanent magnets to achieve a variable stiffness. However, most variable stiffness actuator designs internally present a set of elastic elements, usually springs, and a set of actuated degrees of freedom. The mechanics is such that the apparent output stiffness is determined by the intrinsic properties of the elastic elements and by the configuration of the internal degrees of freedom. For example, in VSA [54], VSA-II [46] and VS-Joint [75], the change of the stiffness is realized by changing the pretension of the internal nonlinear springs. In other actuators, including vsaUT [68, 67], AwAS [34], AwAS-II [35] and HDAU [39], the change of the apparent output stiffness is obtained by changing the transmission ratio between the internal linear springs and the actuator output by implementing a lever arm with variable effective length.

By comparing different working principles and, therefore, different kinematic structures, it can be observed that, during a dynamic behavior of the actuators, part of the power flow from the internal degrees of freedom is directed to the internal elastic elements, instead of to the load. This implies that potential energy is undesirably stored in the elastic elements.

In this paper, we evaluate the power flow in variable stiffness actuators with main focus on the amount of energy captured by the internal elastic elements during a nominal functioning of the actuator. In particular, the aim of this work is to analyze the influence of the actuator kinematics on the power flow in the system. This allows an evaluation of the topology of the actuator without considering the internal friction or dissipation due to specific realization choices. In an earlier work, we already defined a measure of energy consumption during the change of the apparent stiffness [66]. We showed that, in static conditions, the amount of energy used by a variable stiffness actuator to change the apparent output stiffness is strongly influenced by its kinematic properties.

We define a power flow ratio in dynamic conditions that measures how much power can be transferred from the internal degrees of freedom to the output, due to the actuator kinematic design, irrespective of the dynamic behavior of the load. We show that, for different principle designs, this power flow ratio is strictly related to the kinematic properties of the actuator and it is independent of the task realized by the load. The power flow ratio is derived from the analysis of a port-based model of variable stiffness actuators, introduced in [68, 67], which highlights the power flows inside the actuator structure and of the actuator towards the external environment.

The paper is organized as follows. In Section 8.2, we describe a port-based framework of variable stiffness actuators, which provides the necessary background for the power flow analysis and the derivation of the power flow ratio. In Section 8.3, a port-based model of variable stiffness actuators is presented, with particular attention to the analysis of the actuator kinematics. Section 8.4 presents a power flow analysis, which highlights how the power from the control port is distributed between the internal elastic elements and the output port, and we define the power flow ratio, which is then computed for some variable stiffness actuator design principles in Section 8.5. Concluding remarks are given in Section 8.6.

8.2 Port-based Modeling Framework

In this Section, we briefly describe the port-based modeling framework and the bond-graph representation. Further reading can be found in [14, 50].

8.2.1 Port-based Modeling

The fundamental concept behind the port-based modeling framework is that any physical system can be seen as the interconnection of simple elements, which are characterized by a specific energetic behavior. The interconnections are realized by ports, which are defined by a pair of power conjugate variables, namely *flows* and *efforts*. For example, in the mechanical domain, the flows are interpreted as velocities and the efforts as forces.

Let f be an element of the linear space of flows $\mathcal{F}$ and e be an element of the dual linear space of efforts[1] $\mathcal{E} := \mathcal{F}^*$. The dual product $\langle e|f\rangle$ yields power and, therefore, a pair of conjugate variables defines a power flow P on the total space of port variables, i.e.,

$$P = \langle e|f\rangle, \quad (f, e) \in \mathcal{F} \times \mathcal{E}$$

The distribution of power flow among the different ports of the physical system is described by a power continuous network topology. A *Dirac structure* on $\mathcal{F} \times \mathcal{E}$ is a subspace $\mathcal{D} \subset \mathcal{F} \times \mathcal{E}$, with dim $\mathcal{D}$ = dim $\mathcal{F}$, such that

$$\langle e|f\rangle = 0 \quad \forall\, (f, e) \in \mathcal{D} \tag{8.1}$$

This relation defines power-conservation and, therefore, it implies that the total power entering, or leaving, a Dirac structure is zero. The behavior of any physical system can be modeled by making explicit its network topology, i.e., its Dirac structure.

The generic network topology is shown in Figure 8.1, where four separate power ports can be distinguished:

- the *storage port* interconnects the internal energy storage elements $\mathbb{C}$, which represents storage of either generalized potential or generalized kinetic energy. If H is the Hamiltonian energy function of the system, the power conjugate variables (f_S, e_S) at this port satisfy the energy balance

$$\frac{\mathrm{d}H}{\mathrm{d}t} = \langle e_S|f_S\rangle \tag{8.2}$$

- the *dissipative port* interconnects the energy dissipation element $\mathbb{R}$ and is characterized by power conjugate variables (f_R, e_R);
- the *control port*, characterized by power conjugate variables (f_C, e_C), is used for the control actions;

---

[1] Under coordinate transformations, efforts behave as co-vectors. However, for notational convenience, we write them as vectors in this work.

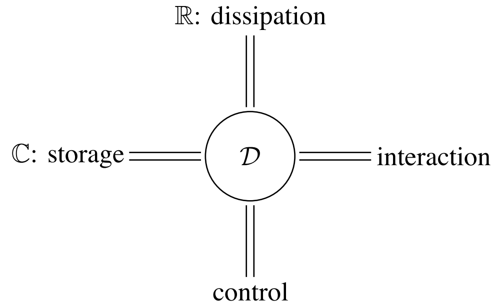

Figure 8.1: Generic network structure of a physical system—The Dirac structure $\mathcal{D}$ defines a power continuous interconnection between the ports. Internal energy storage is represented by a ℂ-element, and energy dissipation by the ℝ-element. The system interacts with the environment via the control port and the interaction port.

- the *interaction port*, characterized by power conjugate variables (f_I, e_I), represents the interactions with the environment, i.e. (a composition of) other physical systems.

Since from the definition in (8.1) the Dirac structure $\mathcal{D}$ is a power continuous network topology, it follows that

$$\langle e_S | f_S \rangle + \langle e_R | f_R \rangle + \langle e_I | f_I \rangle + \langle e_C | f_C \rangle = 0 \tag{8.3}$$

and, by substituting (8.2),

$$\frac{\mathrm{d}H}{\mathrm{d}t} = -\langle e_R | f_R \rangle - \langle e_I | f_I \rangle - \langle e_C | f_C \rangle$$

i.e., the rate of change of the internal energy is determined by the amount of dissipated energy, and the power flow through the interaction and the control ports. This means that the system is passive with respect to these input ports.

A Dirac structure can describe any power continuous network topology, which can be either constant or configuration dependent. Therefore, it provides a complete way to describe any physical system dynamics. In particular, it highlights the power flows inside the system itself and of the system towards the external environment. With respect to variable stiffness actuators, by describing each actuator in terms of its Dirac structure, it is possible to identify both common components and different dynamic behaviors among the various designs. This means that, by deriving for each actuator the corresponding Dirac structure, the different actuators kinematics can be thoroughly analyzed and compared.

8.2.2 Bond Graph Representation

The concept of network topologies, and thus of Dirac structures, allows a compact graphical representation. Using bond graphs, we can represent the generic physical

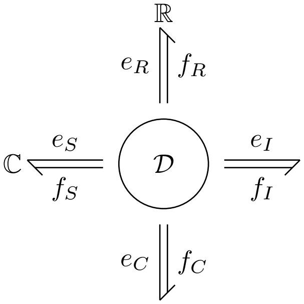

Figure 8.2: Bond graph representation of a generic physical system—The $\mathcal{D}$ is the Dirac structure, the $\mathbb{C}$ represents the energy storage element and the $\mathbb{R}$ the energy dissipation element.

system of Figure 8.1 as in Figure 8.2, where the half arrows are *multi-bonds* and denote the multidimensional interconnections between the different parts of the system. Note that the power flow $\langle e|f\rangle$ is defined positive in the direction of the half-arrow, and, in order to comply with the power continuity constraint (8.1), all bonds must have the same orientation with respect to the Dirac structure.

Throughout the paper, some fundamental interconnection elements are used to detail the Dirac structure that models the variable stiffness actuators. Essentially, these elements are examples of Dirac structures and, since a composition of Dirac structures is again a Dirac structure, these basic elements can give more insights when modeling the behavior of a complex system. Specifically,

- a 1-*junction* defines a common flow interconnection, e.g. a rigid connection between two masses such as the actuator output port and a load. In order to satisfy (8.1), the behavior of a 1-junction, with N connected bonds, satisfies

$$f_1 = \cdots = f_N, \quad \sum_{i=1}^{N} e_i = 0 \tag{8.4}$$

- the dual of a 1-junction is a 0-*junction*, which defines a common effort interconnection. The behavior of a 0-junction, for N connected bonds, is given by

$$\sum_{i=1}^{N} f_i = 0, \quad e_1 = \cdots = e_N \tag{8.5}$$

- a $\mathbb{MTF}$-element (Modulated TransFormer) defines a power continuous transformation between two ports. An example is an ideal gearbox: if the input and the output of the gearbox are characterized by power conjugate variables $(f_{\text{in}}, e_{\text{in}})$ and $(f_{\text{out}}, e_{\text{out}})$ and α is the transformation ratio (either a scalar or a matrix), the behavior for the two ports is described by

$$f_{\text{out}} = \alpha\, f_{\text{in}}, \quad e_{\text{in}} = \alpha^T e_{\text{out}}$$

It is readily verified that any combination of these elements again yields a power continuous interconnection structure.

8.3 Port-based Model of Variable Stiffness Actuators

In this Section, we describe a generic port-based model of variable stiffness actuators. This is possible by identifying common components of the actuators, and describing the interconnection among these components by means of a generic Dirac structure. For any actuator, a specific representation of the Dirac structure can be found by explicitly describing the kinematics of its design. Dynamic properties of different designs can then be derived by analyzing the respective Dirac structures. The generic port-based model has been introduced in [68, 67], and here we intend to revisit the aspects relevant for the remainder of this paper.

8.3.1 Variable Stiffness Actuators as Dirac Structures

In deriving a generic model for variable stiffness actuators, we assume that:

- the actuator output is one dimensional, and is characterized by the generalized configuration variable $r \in \mathcal{R}$;
- the actuator has a number n_s of internal elastic elements, e.g. springs, which can be either linear or nonlinear. The elastic elements are characterized by state $s \in \mathcal{S}$, and by the positive semidefinite energy function $H(s) : \mathcal{S} \to \mathbb{R}$ that describes the amount of stored elastic energy;
- internally, there are $n_q \geq n_s$ actuated degrees of freedom, characterized by the generalized configuration variables $q \in \mathcal{Q}$. These degrees of freedom determine how the elastic elements are sensed at the output and, in particular, they determine the apparent output stiffness K of the actuator, locally defined as

  $$K := \frac{\delta F}{\delta r}$$

  i.e., the ratio of the infinitesimal change of the actuator generalized output force δF as a result of an infinitesimal displacement of the actuator output position δr.

Moreover, in our model, we ignore internal friction and inertias, since we focus on the working principles and on the kinematics of the actuator design, rather than on the details of the implementation.

By these assumptions, we identify the common components of the different variable stiffness actuator designs, i.e. the elastic elements, the internal degrees of freedom, and the interaction port. From the analysis of the kinematics, we derive

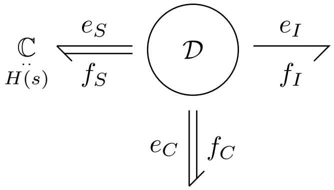

Figure 8.3: Port-based representation of variable stiffness actuators—The $\mathcal{D}$-element represents the Dirac structure. The internal elastic elements are represented by the multidimensional $\mathbb{C}$-element, with state s and elastic energy function $H(s)$. The internal degrees of freedom are actuated via the control port (f_C, e_C), while the interconnection with the load is via the output port (f_I, e_I).

how the different components are interconnected and how the power flows among them.

The generic model of a variable stiffness actuator is depicted, by means of bond graphs, in Figure 8.3. The $\mathbb{C}$-element represents the storage of elastic energy by the internal elastic elements. The power conjugate variables (f_S, e_S) are

$$\dot{s} = f_S, \quad e_S = \frac{\partial H}{\partial s}(s)$$

The control port is characterized by the power conjugate variables (f_C, e_C), which correspond to $(\dot{q}, \tau)$, i.e. the rate of change of the configuration variables q of the internal degrees of freedom and the collocated generalized forces τ, respectively. The interaction port is characterized by the power conjugate variables (f_I, e_I), which correspond to $(\dot{r}, F)$, i.e. the rate of change of the actuator output position r and the generalized output force F. The Dirac structure $\mathcal{D}(q,r)$ defines the interconnection and it is explicitly allowed to depend on the configuration variables q and r. The requirement of power continuity imposes a constraint relation between the power conjugate variables, that can be expressed in a matrix form as

$$\begin{bmatrix} f_S \\ e_C \\ e_I \end{bmatrix} = \underbrace{\begin{bmatrix} 0 & A(q,r) & B(q,r) \\ -A^T(q,r) & 0 & 0 \\ -B^T(q,r) & 0 & 0 \end{bmatrix}}_{D(q,r)} \begin{bmatrix} e_S \\ f_C \\ f_I \end{bmatrix} \tag{8.6}$$

in which the matrix $D(q,r)$ represents the Dirac structure. The skew-symmetry of $D(q,r)$ establishes the power continuity of the interconnection, as stated in (8.1).

The Dirac structure of Figure 8.3 is made explicit in Figure 8.4. The $\mathbb{MTF}$-elements implement the maps $A(q,r)$ and $B(q,r)$, such that

$$\bar{f}_C = A(q,r)\, f_C, \qquad e_C = A^T(q,r)\, \bar{e}_C$$
$$\bar{f}_I = B(q,r)\, f_I, \qquad e_I = B^T(q,r)\, \bar{e}_I$$

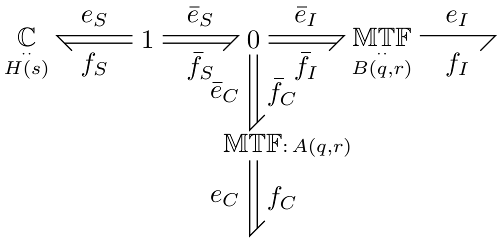

Figure 8.4: Variable stiffness actuators—The Dirac structure expressed in (8.6) can be detailed by using two MTF-elements, which implement the maps defined by $A(q,r)$ and $B(q,r)$. The 1- and 0-junctions implement power continuous connections, with common flow and common effort, respectively.

where the port variables $(\bar{f}_C, \bar{e}_C)$, $(\bar{f}_I, \bar{e}_I)$ and $(\bar{f}_S, \bar{e}_S)$ are introduced on the corresponding bonds. The 0-junction represents a power continuous common effort connection, defined in (8.5), such that

$$\bar{f}_S = \bar{f}_I + \bar{f}_C, \quad \bar{e}_S = \bar{e}_I = \bar{e}_C$$

The Dirac structure representation is completed with the 1-junction, which realizes a power continuous common flow connection as defined in (8.4), such that

$$f_S = \bar{f}_S, \quad \bar{e}_S = -e_S$$

It is readily verified that Figure 8.4 implements (8.6).

The sub-matrix $A(q,r)$ defines the relation between the rate of change of the state s of the elastic elements and the rate of change of the configuration of the internal degrees of freedom q. Similarly, the sub-matrix $B(q,r)$ defines the relation between the rate of change of the state s of the springs and the rate of change of the output position r. Hence, the exact structure of $A(q,r)$ and $B(q,r)$ can be derived from a kinematic analysis of the actuator design.

8.3.2 Kinematic Structure of Variable Stiffness Actuators

It is assumed that the state s of the internal elastic elements is determined by the configuration q of the internal degrees of freedom and the output position r via the kinematic relation

$$\begin{array}{rccc} \lambda: & \mathcal{Q} \times \mathcal{R} & \rightarrow & \mathcal{S} \\ & (q,r) & \mapsto & s \end{array} \tag{8.7}$$

Note that the variables q and r are independent from each other and their configuration determines the state of the internal elastic elements.

The tangent map $\lambda_* : T_q\mathcal{Q} \times T_r\mathcal{R} \rightarrow T_s\mathcal{S}$ and the cotangent map $\lambda^* : T_s^*\mathcal{S} \rightarrow T_q^*\mathcal{Q} \times T_r^*\mathcal{R}$ are naturally defined [42], where $T_q\mathcal{Q}$ $(T_q^*\mathcal{Q})$, $T_r\mathcal{R}$ $(T_r^*\mathcal{R})$ and $T_s\mathcal{S}$ $(T_s^*\mathcal{S})$ are the tangent (cotangent) spaces to the manifolds $\mathcal{Q}$, $\mathcal{R}$ and $\mathcal{S}$ at q, r and s, respectively.

The tangent maps can be expressed in the natural coordinates on the tangent space as

$$\lambda_* = \left(\frac{\partial \lambda}{\partial q}(q,r), \frac{\partial \lambda}{\partial r}(q,r) \right) =: (A(q,r), B(q,r))$$

Dually, the cotangent map can be expressed in the natural coordinates as

$$\lambda^* = \left(\frac{\partial^T \lambda}{\partial q^T}(q,r), \frac{\partial^T \lambda}{\partial r^T}(q,r) \right) =: \left(A^T(q,r), B^T(q,r) \right)$$

which completes the mathematical representation of the Dirac structure (8.6).

As observed already from (8.6), the tangent maps define the rate of change of the state s of the elastic elements as a result of the flows f_C and f_I. In particular, considering the natural coordinates on the tangent spaces, we have

$$\dot{s} = A(q,r)\dot{q} + B(q,r)\dot{r} \tag{8.8}$$

In Figure 8.5, the tangent map λ_* is visualized. More specifically, note that each one of the maps defined by $A(q,r)$ and $B(q,r)$ have an image space, which is a subspace of the tangent space $T_s\mathcal{S}$. The dimensions of the image of $A(q,r)$ depend on the number of internal elastic elements and the number of internal degrees of freedom, while the image of $B(q,r)$ is always one-dimensional, since the actuator output is assumed to have only one degree of freedom.

Under the map λ^*, it follows that $e_C = -A^T(q,r)e_S$ and $e_I = -B^T(q,r)e_S$, which state that the efforts τ and F depend on the effort e_S generated by the elastic elements. In particular, considering the natural coordinates on the cotangent space, the effort e_S is given by $\frac{\partial H}{\partial s}$ and, through the map $A^T(q,r)$ and the map $B^T(q,r)$ respectively, we obtain

$$\tau = -A^T(q,r)\frac{\partial H}{\partial s}, \quad F = -B^T(q,r)\frac{\partial H}{\partial s}$$

We use this kinematic analysis to compute the power flows in variable stiffness actuators and, more specifically, in the various bonds of the model depicted in Figure 8.4.

8.4 Power Flow Analysis

In this Section, we provide a detailed study of the power flows in variable stiffness actuators using the port-based model presented in the previous Section 8.3. By analyzing the kinematic structure of the actuators, we highlight the power transferred from the control port, i.e. the internal degrees of freedom, to the internal elastic elements and to the output port. This analysis is facilitated by a change of coordinates on $T_s\mathcal{S}$ and $T_s^*\mathcal{S}$ that makes these power flows explicit. In particular, while the Dirac structure (8.6) describes the power distribution inside the variable stiffness actuator, it does not explicitly quantify the power exchange between the

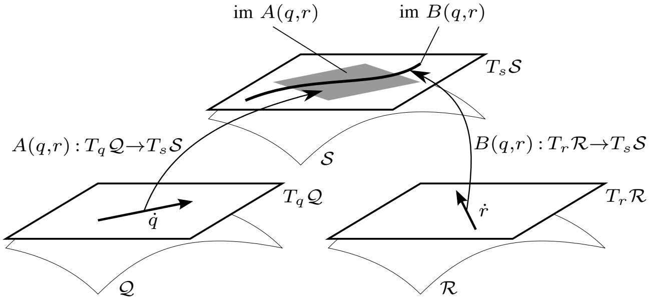

Figure 8.5: Maps between the tangent spaces $T_q\mathcal{Q}$, $T_r\mathcal{R}$ and $T_s\mathcal{S}$—The image spaces of the maps $A(q,r)$ and $B(q,r)$ are subspaces of $T_s\mathcal{S}$.

control and the output ports. A proper change of coordinates, as detailed in this Section, allows to determine how much control power can reach the output port. This is based on an analysis of the kinematics of the actuator and, more specifically, by examining the relation between the rate of change of the configuration variables of the actuation system, i.e., $\dot{s}$, $\dot{q}$, $\dot{r}$, as defined by the maps between the tangent spaces described in Section 8.3.2.

8.4.1 Change of Coordinates

The power flow between the internal elastic elements, the control and the interaction ports is implicitly described by (8.3) and, in natural coordinates, is given by

$$\langle \frac{\partial H}{\partial s} | \dot{s} \rangle = \langle \frac{\partial H}{\partial s} | A(q,r)\dot{q} \rangle + \langle \frac{\partial H}{\partial s} | B(q,r)\dot{r} \rangle$$

in which we assume that no dissipation is internally present. This means that the power flows are determined by the tangent maps $A(q,r)$ and $B(q,r)$. To further investigate the power flows, we define a new set of coordinates on $T_s\mathcal{S}$ and $T_s^*\mathcal{S}$ by using the image of the map $B(q,r)$.

Since the actuator output has only one degree of freedom, i.e., r is one dimensional, the image of the tangent map $B(q,r)$ is also one dimensional and, in particular, it defines a line on $T_s\mathcal{S}$. Let $b^{\|}$ be a unit vector such that

$$\text{im } B(q,r) = \text{span } \{b^{\|}\}$$

Then, a set of $n_s - 1$ unit vectors $b^{\perp}$ exists, such that

$$\text{span } \{b^{\perp}\} = \text{im } B^{\perp}(q,r)$$

The subspace im $B^{\perp}(q,r)$ is the orthogonal complement to im $B(q,r)$ and, therefore, it is of dimension $n_s - 1$. This means that $\{b^{\|}, b^{\perp}\}$ form a set of coordinate vectors that spans the tangent space $T_s\mathcal{S}$, i.e., $T_s\mathcal{S} = \text{im } B(q,r) \oplus \text{im } B^{\perp}(q,r)$.

Orthogonality on the tangent space $T_s\mathcal{S}$ is only defined if a proper metric is defined on it. Elements from $T_s\mathcal{S}$ represent the rate of change of the state s of the elastic elements, which may be equivalently considered as infinitesimal displacements δs. A physically meaningful metric to measure δs is the stiffness matrix [25, 24]. As stated in [76], in a conservative system, the stiffness matrix in configuration space coordinates is given by the Hessian of the potential energy function, and can be shown to be a symmetric $(0, 2)$-tensor, and is thus a valid metric on $T_s\mathcal{S}$. In our case, if we consider the natural coordinates on $T_s\mathcal{S}$, the metric M is therefore given by

$$M = \frac{\partial^2 H}{\partial s^2}$$

where $H(s)$ describes the amount of elastic energy stored in the elastic elements. Note that the norm $\|\delta s\|_M^2 = \delta s^T M \delta s$, induced by the metric M, has the unit of energy. If friction in the system is modeled, a different metric should be considered since the hypothesis of a conservative system is not valid anymore.

As the metric M defines the inner product on $T_s\mathcal{S}$, the set $b^\perp$ is found by requiring

$$\langle b^{\|}, b_i^\perp \rangle_M = 0, \qquad i = 1, \ldots, n_s - 1$$

where $\langle \cdot, \cdot \rangle_M$ denotes the inner product with respect to the metric M.

We can now define a change of coordinates from the natural coordinates on $T_s\mathcal{S}$ to the new defined coordinates. Let S_b be a matrix describing the change of coordinates as

$$S_b = \begin{bmatrix} b^{\|} & b^\perp \end{bmatrix} \tag{8.9}$$

Note that S_b depends on the state s of the elastic elements. If $\dot{s}$ is an element of $T_s\mathcal{S}$, expressed in the natural coordinates, and $\dot{s}^b$ the same element, expressed in the coordinates $\{b^{\|}, b^\perp\}$, it follows that

$$\dot{s} = S_b \dot{s}^b \tag{8.10}$$

and, since the change of coordinates is by construction invertible, it follows that $\dot{s}^b = S_b^{-1} \dot{s}$.

The elements on $T_s\mathcal{S}$ defined in (8.8) can be expressed in the new coordinates. In particular, we have

$$\begin{aligned}
\dot{s}^b &= S_b^{-1} \dot{s} \\
&= S_b^{-1} \left(A(q, r)\dot{q} + B(q, r)\dot{r} \right) \\
&=: S_b^{-1} \left(\dot{s}_q + \dot{s}_r \right) \\
&=: \begin{pmatrix} \dot{s}_q^{\|} \\ \dot{s}_q^\perp \end{pmatrix} + \begin{pmatrix} \dot{s}_r^{\|} \\ \dot{s}_r^\perp \end{pmatrix} =: \begin{pmatrix} \dot{s}^{\|} \\ \dot{s}^\perp \end{pmatrix}
\end{aligned} \tag{8.11}$$

The element $\dot{s}_r^\perp$ is zero by construction of the coordinate set.

Essentially, with this change of coordinates, from the real elastic element $\mathbb{C}$ with state s, we create two virtual storage elements $\mathbb{C}^{\|}$ and $\mathbb{C}^\perp$, with states $s^{\|}$ and

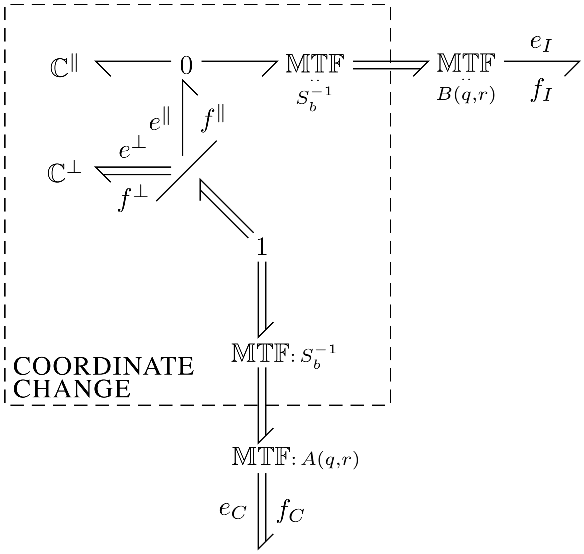

Figure 8.6: Visualization of the virtual storage elements—The change of coordinates S_b^{-1} can be realized by two $\mathbb{MTF}$-elements and a power splitter (the diagonally-oriented line). The two $\mathbb{C}$-elements, i.e., $\mathbb{C}^{\|}$ and $\mathbb{C}^{\perp}$, represent the virtual storage elements.

$s^{\perp}$, respectively. By construction, the state $s^{\|}$ is one-dimensional, and the state $s^{\perp}$ has dimension $n_s - 1$. This scenario is depicted in Figure 8.6. From (8.11), it can be noted that the virtual storage elements $\mathbb{C}^{\perp}$ is not connected to the output, i.e., it captures the energy supplied via the control port without redistributing it to the output.

8.4.2 Power Flows

Only when the change of coordinates (8.10) is also applied to elements of the cotangent space $T_s^*\mathcal{S}$, the power flows to $\mathbb{C}^{\|}$ and $\mathbb{C}^{\perp}$ can be analyzed. On $T_s^*\mathcal{S}$, the change of coordinates results in the transformation of efforts as [42]

$$\frac{\partial^T H}{\partial s^T} S_b =: \begin{pmatrix} F_S^{\|} & F_S^{\perp} \end{pmatrix} \tag{8.12}$$

The port behavior of the two virtual storage elements $\mathbb{C}^{\|}$ and $\mathbb{C}^{\perp}$ can now be properly defined by using (8.11) and (8.12), i.e.,

$$\begin{aligned} \dot{s}^{\|} &= \dot{s}_q^{\|} + \dot{s}_r^{\|}, & e_S^{\|} &= F_S^{\|} \\ \dot{s}^{\perp} &= \dot{s}_q^{\perp}, & e_S^{\perp} &= F_S^{\perp} \end{aligned}$$

The power supplied via the control port is given by

$$P_C = \langle e_C | f_C \rangle = -\langle A^T(q,r)\, e_S | \dot{q} \rangle = -\langle \frac{\partial H}{\partial s} | \dot{s}_q \rangle$$

and expressions for the power flows from the control port toward the two virtual storage elements are

$$P_C^{\|} = -\langle F_S^{\|} | \dot{s}_q^{\|} \rangle \tag{8.13}$$

$$P_C^{\perp} = -\langle F_S^{\perp} | \dot{s}_q^{\perp} \rangle \tag{8.14}$$

It is readily verified that the change of coordinates is power continuous, i.e.,

$$P_C^{\|} + P_C^{\perp} = P_C$$

Remark 8.1 Note that the dynamical behavior of the load is not modeled and, therefore, the proposed analysis is task-independent. The power flow P_L to the load is given by $P_L = P_C - P^{\|} - P^{\perp}$, in which $P^{\|}$ cannot be computed. However, since there is a direct connection between $\mathbb{C}^{\|}$ and the output, by means of the 0-junction, the power flow $P^{\|}$ can be used to do work on the output. On the other hand, the power flow $P^{\perp}$ is completely captured by $\mathbb{C}^{\perp}$. It represents the power supplied by the control port, which cannot be used to do any work on the output, but is instead internally stored in the actuator due to its kinematic structure. $\lhd$

Remark 8.2 The image of the map $B(q,r)$ defines an involutive distribution on $\mathcal{S}$ with dimension one, since the output has only one degree of freedom. If the set $\{b^{\perp}\}$ is not empty, then, for any configuration (q,r), there exists a foliation $\mathcal{S}_r$ that is the integral manifold of this distribution [42]. This integral manifold is also one-dimensional. Since the energy function $H(s)$ is positive semidefinite by definition, it has a minimum on $\mathcal{S}_r$, which defines how much energy can go out from the elastic elements via the output port. This minimum is however, in general, not the same as the global minimum of $H(s)$ on $\mathcal{S}$. Hence, there is energy stored in the elastic elements that cannot be used to do work on the output. $\lhd$

8.4.3 Power Flow Ratio

The change of coordinates and the subsequent definition of power flows in (8.13) and (8.14), as visualized in Figure 8.6, give rise to the definition of a power flow ratio. As already observed, the virtual power flow $P_C^{\perp}$ is disconnected from the output, and thus it cannot be used to do work at the output. Intuitively, the ratio

$$\mu = \frac{P_C^{\perp}}{P_C} \tag{8.15}$$

indicates how much of the power supplied via the control port is, in fact, captured by the virtual storage element $\mathbb{C}^{\perp}$ and, therefore, lost: the lower this measure is, the less energy is captured by the elastic elements. Note that $\mu \in [0,1]$.

Since the coordinate change is configuration dependent, the power flow ratio μ is a dynamic measure of power flows. The rationale in this analysis is that instantaneous power provided by the controller should provide an instantaneous power flow to the output and should closely match the provided power flow from the controller.

8.5 Analysis of Conceptual Variable Stiffness Actuator Designs

In this Section, we analyze the working principles of three designs of variable stiffness actuators, which realize a variable output stiffness by means of different kinematic structures. As follows from the previous Sections, the power flows to the virtual storage elements are defined by the maps $A(q, r)$ and $B(q, r)$, i.e., by the kinematic properties of the actuator design. First, we present the model of the designs in a port-based formalism, and then we proceed by evaluating the power flow ratio μ, as defined in (8.15).

8.5.1 Design Based on a Lever Arm of Variable Length

In some designs, such as the vsaUT [68, 67], AwAS [34], AwAS-II [35] and HDAU [39], the change of the output stiffness is realized through a change of the transmission ratio between the internal springs and the actuator output by means of a lever arm of variable length.

As an example of this category of variable stiffness actuators, we analyze the vsaUT, which is conceptually depicted in Figure 8.7. The working principle is based on one zero free length linear spring, characterized by elastic constant k. The spring is connected to the output via a lever arm of variable length, controlled by the linear degree of freedom q_1, and thus q_1 determines how the spring is sensed at the output. The linear degree of freedom q_2 is used to control the actuator output position, i.e. the configuration variable r. The design is such that the maximum length ℓ of the lever arm is sufficiently large compared to the maximum elongation of the spring, so that we can assume $\alpha \approx 0$.

In order to build the port-based model of this actuator design, we analyze its kinematics, described by (8.7). We observe that the state s of the linear zero free length spring is given by

$$s = \ell \sin\phi = \ell \frac{r - q_2}{q_1} \tag{8.16}$$

By taking the total derivative of (8.16), it follows

$$\dot{s} = -\frac{\ell}{q_1} \begin{bmatrix} \frac{r-q_2}{q_1} & 1 \end{bmatrix} \begin{bmatrix} \dot{q}_1 \\ \dot{q}_2 \end{bmatrix} + \frac{\ell}{q_1} \dot{r} =: f_S$$

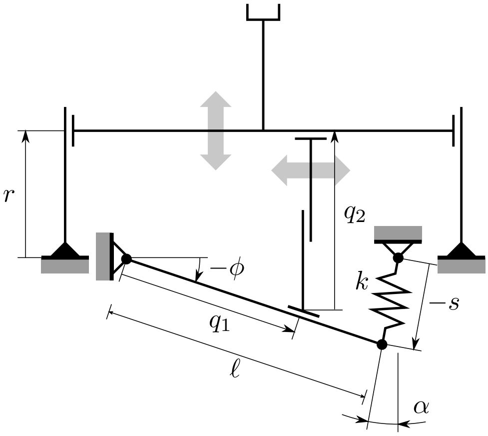

Figure 8.7: Variable stiffness actuator using a lever arm of variable length—The functional principle of the concept is a lever arm of variable length q_1, which connects the zero free length linear spring, with elastic constant k, to the output. The effective length of the lever arm is determined by the linear degree of freedom q_1. The actuator output position r is controlled by the linear degree of freedom q_2 [68, 67].

From this equation, we can identify the matrices $A(q,r)$ and $B(q,r)$, i.e.,

$$A(q,r) = -\frac{\ell}{q_1}\begin{bmatrix} \frac{r-q_2}{q_1} & 1 \end{bmatrix}, \quad B(q) = \frac{\ell}{q_1}$$

with which it is possible to build the skew-symmetric matrix $D(q,r)$ that represents the Dirac structure, as defined in (8.6).

Since only one spring is present, the tangent space $T_s\mathcal{S}$ is one-dimensional. The image of $B(q,r)$ is given by

$$\text{im } B(q,r) = T_s\mathcal{S}, \qquad \forall (q,r) \in \mathcal{Q} \times \mathcal{R}$$

It follows that the virtual storage element $\mathbb{C}^{\perp}$ has zero dimension, i.e., it does not appear in the diagram of Figure 8.6. Therefore, all the power P_C, supplied via the control port during any nominal behavior of the actuator, goes either to $\mathbb{C}^{\parallel}$ or to the output. This means that no power is lost, i.e., no energy is captured by the internal springs. This means that, for this principle design, the power flow ratio μ, as defined in (8.15), is

$$\mu = 0$$

This observation is in accordance with the static analysis presented in [66], where it was shown that the designs based on a variable length lever arm do not require any storage of energy in the internal springs when the apparent output stiffness is changed.

8.5.2 Design Based on an Antagonistic Spring Setup

Variable stiffness actuators, based on an antagonistic spring setup, have been proposed in different realizations, such as the AMASC [33], VSA [54], VSA-II [46]. In general, the designs use nonlinear springs, that act in opposite directions on the output. The internal degrees of freedom change the elongation of the springs, and, in this way, they indirectly change the actuator output position and the apparent output stiffness.

The conceptual design of a generic antagonistic variable stiffness actuator is depicted in Figure 8.8. The working principle is based on two identical nonlinear quadratic springs, characterized by elastic constant k. The springs are in series with two linear motors M_1 and M_2, which generate the two linear displacements q_1 and q_2, respectively. When the motors are operated in common mode, the actuator output stiffness is changed. When the motors are operated in differential mode, the actuator output position r is changed.

In order to build the port-based model of this actuator design, we analyze its kinematics, described by (8.7). We observe that the states $s_i > 0$, with $i = 1, 2$, of the nonlinear springs are given by

$$s = \begin{bmatrix} s_1 \\ s_2 \end{bmatrix} = \begin{bmatrix} q_1 - Rr \\ q_2 + Rr \end{bmatrix} \tag{8.17}$$

where R is the radius of the pulley and the restriction $s_i > 0$ is assumed to simplify the equations involving the force generated by the quadratic springs. By taking the total derivative of (8.17), we obtain

$$\dot{s} = \begin{bmatrix} \dot{s}_1 \\ \dot{s}_2 \end{bmatrix} = \begin{bmatrix} \dot{q}_1 - R\dot{r} \\ \dot{q}_2 + R\dot{r} \end{bmatrix} =: \begin{bmatrix} f_{S_1} \\ f_{S_2} \end{bmatrix}$$

From this, we can identify the matrices $A(q, r)$ and $B(q, r)$, i.e.,

$$A(q, r) = \begin{bmatrix} 1 & 0 \\ 0 & 1 \end{bmatrix}, \quad B(q, r) = \begin{bmatrix} -R \\ R \end{bmatrix}$$

with which it is possible to build the skew-symmetric matrix $D(q, r)$ that represents the Dirac structure, as defined in (8.6).

As this design presents two springs, the tangent space $T_s\mathcal{S}$ is two-dimensional. Let the metric M be

$$M = \frac{\partial^2 H}{\partial s^2} = \begin{bmatrix} 2ks_1 & 0 \\ 0 & 2ks_2 \end{bmatrix}$$

where $H(s) = \frac{1}{3}ks_1^2 + \frac{1}{3}ks_2^2$ is the elastic energy of the nonlinear quadratic springs. The unit vector $b^{\|}$, computed with respect to the metric M such that $\|b^{\|}\|_M = 1$, is

$$b^{\|} = \frac{1}{\sqrt{2k(s_1 + s_2)}} \begin{bmatrix} -1 \\ 1 \end{bmatrix}$$

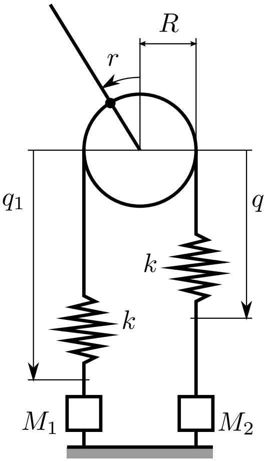

Figure 8.8: Variable stiffness actuator using an antagonistic spring setup—This design is based on two series elastic actuators in an antagonistic setup. The linear motors M_1 and M_2 generate linear displacements q_1 and q_2. The nonlinear quadratic springs have elastic constant k. By operating the motors in common mode, the apparent output stiffness of the actuator changes, while by operating the motors in differential mode the equilibrium of the actuator output position r changes.

Using the constraints on the orthogonality, i.e., $\langle b^{\|}, b^{\perp}\rangle_M = 0$, the unit vector $b^{\perp}$, computed with respect to the metric M such that $\|b^{\perp}\|_M = 1$, is

$$b^{\perp} = \frac{1}{\sqrt{2k(s_1+s_2)}} \begin{bmatrix} \sqrt{\frac{s_2}{s_1}} \\ \sqrt{\frac{s_1}{s_2}} \end{bmatrix}$$

The change of coordinates, as defined in (8.9), follows

$$S_b = \begin{bmatrix} b^{\|} & b^{\perp} \end{bmatrix} = \frac{1}{\sqrt{2k(s_1+s_2)}} \begin{bmatrix} -1 & \sqrt{\frac{s_2}{s_1}} \\ 1 & \sqrt{\frac{s_1}{s_2}} \end{bmatrix}$$

In order to continue the power analysis presented in Section 8.4, we calculate

$$\begin{aligned} \begin{pmatrix} \dot{s}_q^{\|} \\ \dot{s}_q^{\perp} \end{pmatrix} &= S_b^{-1} A(q,r)\dot{q} \\ &= \frac{\sqrt{2k(s_1+s_2)}}{s_1+s_2} \begin{bmatrix} -s_1 & s_2 \\ \sqrt{s_1 s_2} & \sqrt{s_1 s_2} \end{bmatrix} \begin{bmatrix} 1 & 0 \\ 0 & 1 \end{bmatrix} \begin{bmatrix} \dot{q}_1 \\ \dot{q}_2 \end{bmatrix} \\ &= \frac{\sqrt{2k(s_1+s_2)}}{s_1+s_2} \begin{bmatrix} -s_1\dot{q}_1 + s_2\dot{q}_2 \\ \sqrt{s_1 s_2}(\dot{q}_1 + \dot{q}_2) \end{bmatrix} \end{aligned}$$

The quadratic spring generate forces $e_S = \frac{\partial H}{\partial s} = \begin{bmatrix} ks_1^2 & ks_2^2 \end{bmatrix}^T$, from which we obtain

$$\begin{aligned} \begin{pmatrix} F_S^{\parallel} & F_S^{\perp} \end{pmatrix} &= \frac{\partial^T H}{\partial s^T} S_b \\ &= \begin{bmatrix} ks_1^2 & ks_2^2 \end{bmatrix} \frac{1}{\sqrt{2k(s_1+s_2)}} \begin{bmatrix} -1 & \sqrt{\frac{s_2}{s_1}} \\ 1 & \sqrt{\frac{s_1}{s_2}} \end{bmatrix} \\ &= \frac{1}{\sqrt{2k(s_1+s_2)}} \begin{bmatrix} k\left(-s_1^2+s_2^2\right) & k\left(\sqrt{s_1^3 s_2} + \sqrt{s_1 s_2^3}\right) \end{bmatrix} \end{aligned} \tag{8.18}$$

The power flow ratio μ, as defined in (8.15), is given by

$$\mu = \frac{P_C^{\perp}}{P_C} = \frac{\langle F_S^{\perp} | \dot{s}_q^{\perp} \rangle}{\langle \frac{\partial H}{\partial s} | \dot{s}_q \rangle}$$

Since μ is a dynamic measure, we can compute it during any nominal behavior of the variable stiffness actuator. The power flow ratio is visualized in Figure 8.9, where $\dot{q}$ has been chosen such to achieve certain desired changes in output position ($\dot{r}$) and stiffness ($\dot{K}$). The areas indicate that, for a particular $(\dot{r}, \dot{K})$, the value of μ is in the corresponding area. For example, the power flow ratio μ is in the area denoted by μ_1 when the output stiffness is changed with $\dot{K} = 0.2$ Nm/rad/s and the output position r is changed simultaneously. The actual value of μ depends on the load of the springs, i.e., (s_1, s_2), and it is negatively affected by higher preloads, which is in agreement with [66]. From (8.18), it can be seen that $P^{\parallel} = \langle F_S^{\parallel} | \dot{s}_q^{\parallel} \rangle = 0$ if $s_1 = s_2$, and hence, due to power continuity, $\mu = 1$. Finally, note that the power flow ratio increases when the stiffness change is faster.

For this particular design principle, Remark 8.2 can be illustrated visually. In Figure 8.10, the surface represents the energy function $H(s) = \frac{1}{3}ks_1^3 + \frac{1}{3}ks_2^3$ on the manifold $\mathcal{S}$ and the black curves represent the energy function on the integral manifolds $\mathcal{S}_r$ of $B(q,r)\dot{r}$. Restricted to these foliations, $H(s)$ has a minimum indicated by the dashed line. Since the matrix $A(q,r)$ is full rank for this design, the integral manifold of $A(q,r)\dot{q}$ is in fact equal to $\mathcal{S}$. This means that, using the control input $\dot{q}$ with its corresponding control energy, it is possible to go from any configuration on $\mathcal{S}$ to any other configuration. However, through the output port, the configuration change is restricted to lie on the foliation $\mathcal{S}_r$ that has been reached. Therefore, the minimum energy level, that the system can reach, is in a local minimum of $H(s)$. This is illustrated via the solid black curve, which represents a generic change of configuration of the actuator. It can be seen that in general the energy, which has been supplied via the control port, cannot be provided completely to the output port. The actual amount of energy that is internally stored is equal to the difference in energy levels at the end points of the solid curve, i.e., $H_2 - H_1$.

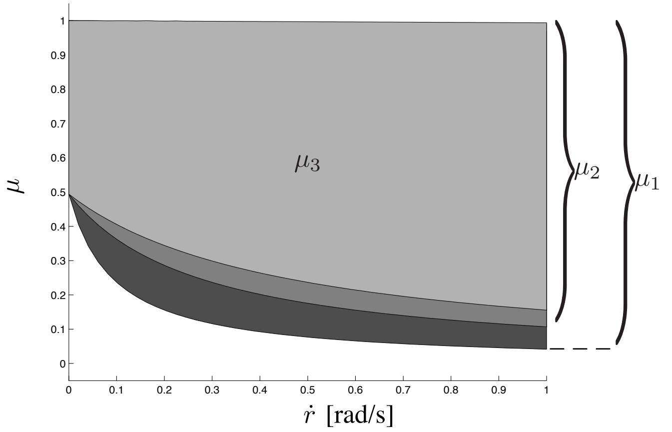

Figure 8.9: Power flow ratio μ for the design based on an antagonistic spring setup—The rate of change of the configuration variable $\dot{q}$ of the internal degrees of freedom is chosen so to achieve the desired changes in output position ($\dot{r}$) and stiffness ($\dot{K}$). The indicated areas μ_1, μ_2, μ_3 correspond to $\dot{K} = 0.2$ Nm/rad/s, $\dot{K} = 0.6$ Nm/rad/s and $\dot{K} = 1.0$ Nm/rad/s, respectively.

Example

The simple structure of this type of actuator allows to illustrate the theory with a straightforward simulation experiment. We assume that a mass is attached to the output and that, starting from a zero velocity, it should achieve a constant $\dot{r}$, while the apparent output stiffness is changed simultaneously with constant $\dot{K}$. It follows that the control input $\dot{q}$ is also constant.

Figure 8.11 presents the power flow $P^{\parallel}$ to the virtual storage element $\mathbb{C}^{\parallel}$, the power flow $P^{\perp}$ to the virtual storage element $\mathbb{C}^{\perp}$, the total power flow P_C from the control port, and the power flow P_L to the load.

Initially, all power is stored as potential energy in $\mathbb{C}^{\parallel}$ and $\mathbb{C}^{\perp}$, due to the inertia of the load, and, therefore, the power flows $P^{\parallel}$ and $P^{\perp}$ increase. While $P^{\parallel} > P_L$, the mass accelerates and the power P_C is diverted to $\mathbb{C}^{\parallel}$ and stored as potential energy. When $P^{\parallel} \leq P_L$, this potential energy is started to be released to the load. Note that $P^{\perp}$ is always increasing, which means that part of the control power P_C is captured by the internal springs and not used to accelerate the mass.

Figure 8.12 presents the energy balance between the energy H_C supplied by the controller and the kinetic energy H_L of the load. Because, throughout the experiment, $P_C > P^{\parallel}$ the controller supplies much more energy than is converted to kinetic energy of the load. In fact, the difference $H_C - H_L$ is stored internally in the springs.

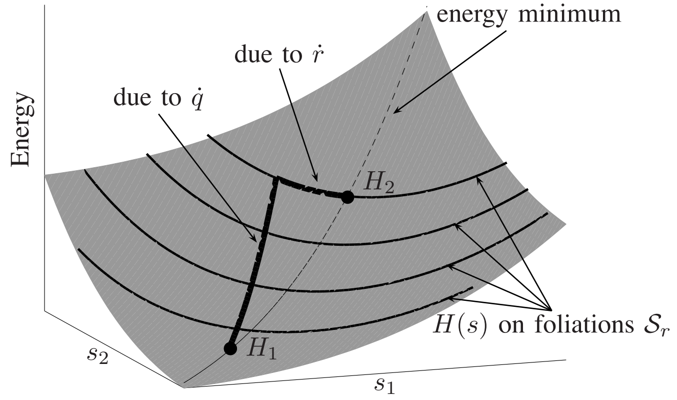

Figure 8.10: Energy function on $\mathcal{S}$—The surface represents the energy function $H(s)$ on $\mathcal{S}$. Since the image of $A(q,r)$ spans the entire tangent space $T_s\mathcal{S}$, any arbitrary point $s \in \mathcal{S}$ can be reached by a proper $\dot{q}$. However, restricted to the foliations $\mathcal{S}_r$ (indicated by the black lines), only a local minimum of $H(s)$ can be reached (indicated by the dashed line). The difference in energy levels between the end points of the thick black curve, i.e., $H_2 - H_1$, indicates how much energy cannot be used to do work on the output.

8.5.3 Design based on a Mechanical Decoupling

In other designs, such as the VS-Joint [75], the change of the apparent output stiffness and the change of the output joint position is completely mechanically decoupled. The conceptual design of this kind of actuators is depicted in Figure 8.13. The working principle is based on two identical nonlinear quadratic springs, characterized by elastic constant k. The linear motor M_2 generates a linear displacement q_2 and is used for changing the apparent output stiffness of the actuator. The output position r is determined by the rotational motor M_1, which directly controls the degree of freedom q_1. Note that thus the end effector can rotate independently from the pulley. Compared with the antagonistic design presented in Section 8.5.2, the degree of freedom q_1 realizes the differential mode of operation of the motors M_1 and M_2 in the antagonistic design, and the degree of freedom q_2 the common mode operation.

In order to build the port-based model of this actuator design, we analyze its kinematics, described by (8.7). We observe that the states $s_i > 0$, with $i = 1, 2$, of the nonlinear spring are given by

$$s = \begin{bmatrix} s_1 \\ s_2 \end{bmatrix} = \begin{bmatrix} q_2 - R\alpha \\ q_2 + R\alpha \end{bmatrix} \tag{8.19}$$

where R is the radius of the pulley, $\alpha = -q_1 + r + \frac{\pi}{2}$ and the restriction $s_i > 0$ is assumed to simplify the equations involving the force generated by the quadratic

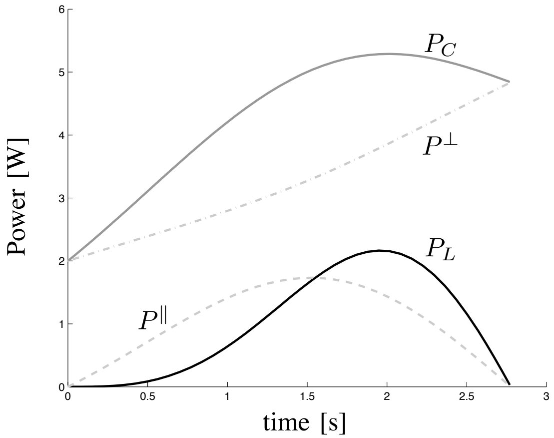

Figure 8.11: Power flow—The power supplied via the control port is used to accelerate the mass. Initially, all the power is stored in $\mathbb{C}^\parallel$ and $\mathbb{C}^\perp$, i.e. $P_L = 0$, due to the inertia of the load. When $P^\parallel > P_L$, power is flowing towards $\mathbb{C}^\parallel$ and stored, but later, when $P^\parallel < P_L$, power is flowing from $C^\parallel$ to the load.

springs. By taking the total derivative of (8.19), we obtain

$$\dot{s} = \begin{bmatrix} \dot{s}_1 \\ \dot{s}_2 \end{bmatrix} = \begin{bmatrix} \dot{q}_2 + R\dot{q}_1 - R\dot{r} \\ \dot{q}_2 - R\dot{q}_1 + R\dot{r} \end{bmatrix} =: \begin{bmatrix} f_{S_1} \\ f_{S_2} \end{bmatrix}$$

From this, we identify the matrices $A(q,r)$ and $B(q,r)$, i.e.,

$$A(q,r) = \begin{bmatrix} R & 1 \\ -R & 1 \end{bmatrix}, \quad B(q,r) = \begin{bmatrix} -R \\ R \end{bmatrix}$$

with which the Dirac structure, as defined in (8.6), can be represented.

The matrix $B(q,r)$ for this design is the same as for the previous design. Hence, the image is exactly the same, and the same change of coordinates S_b is obtained. We then have

$$\begin{aligned} \begin{pmatrix} \dot{s}_q^\parallel \\ \dot{s}_q^\perp \end{pmatrix} &= S_b^{-1} A(q,r)\dot{q} \\ &= \frac{\sqrt{2k(s_1+s_2)}}{s_1+s_2} \begin{bmatrix} \frac{-s_1}{\sqrt{s_1 s_2}} & \frac{s_2}{\sqrt{s_1 s_2}} \end{bmatrix} \begin{bmatrix} R & 1 \\ -R & 1 \end{bmatrix} \begin{bmatrix} \dot{q}_1 \\ \dot{q}_2 \end{bmatrix} \\ &= \frac{\sqrt{2k(s_1+s_2)}}{s_1+s_2} \begin{bmatrix} -R\dot{q}_1(s_1+s_2) - \dot{q}_2(s_1-s_2) \\ 2\sqrt{s_1 s_2}\dot{q}_2 \end{bmatrix} \end{aligned}$$

The forces $e_S = \frac{\partial H}{\partial s}$ are the same as in the antagonistic design, and hence we can compute μ according to (8.15)

$$\mu = \frac{P_C^\perp}{P_C} = \frac{\langle F_S^\perp | \dot{s}_q^\perp \rangle}{\langle \frac{\partial H}{\partial s} | \dot{s}_q \rangle}$$

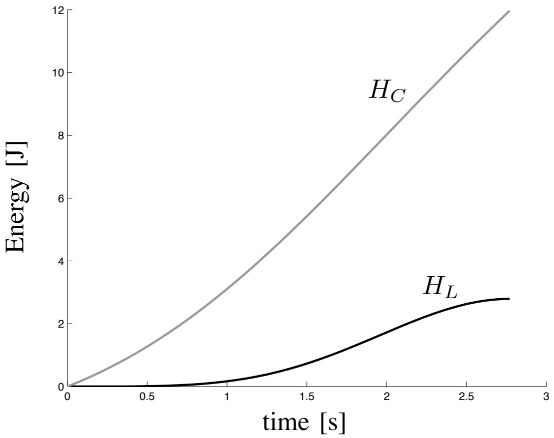

Figure 8.12: Energy balance—During the acceleration of the mass the energy supplied by the controller is bigger than the energy converted to kinetic energy of the load.

Figure 8.14 presents a visualization of the power flow ratio, where $\dot{q}_1$ has been used to achieve the indicated $\dot{r}$, and $\dot{q}_2$ to achieve $\dot{K}$. The areas indicate that, for a particular $(\dot{r}, \dot{K})$, the value of μ will be in the corresponding area. Also for this design, the actual value of μ depends on the load of the springs, i.e., (s_1, s_2), and it is negatively affected by higher preloads. As in the previous design, it can be noted that the power flow ratio increases when the stiffness change is faster. However, because of the mechanical decoupling of the position and stiffness change, this influence is bigger than in the previous design.

8.6 Conclusions

In this paper, we defined a power flow ratio for variable stiffness actuators, derived by using a port-based modeling framework. The power flow ratio is computed in dynamic conditions and determines how the working principle of the actuator allows in transferring the power from the internal degrees of freedom to the output, irrespectively of the dynamic behavior of the load. We showed in three different principle designs that the power flow ratio is strictly related to the kinematic properties of the actuator, i.e., to its topological structure.

It was observed that the pretension of the internal elastic elements has a negative influence on the power flow ratio. This can be explained by observing the relation between the output motion and the state of the internal springs. We have shown that this effect becomes more prominent when the rate of change of the stiffness increases.

From the power flow analysis, it can be concluded that for variable stiffness actuators, realized by a variable transmission ratio between the output and the internal springs, all the power supplied by the control port can be used to do work

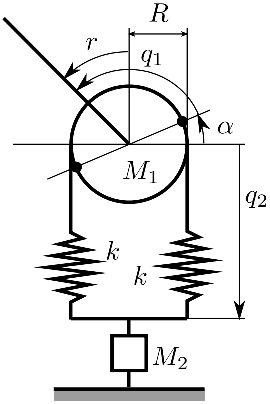

Figure 8.13: Variable stiffness actuator using an antagonistic spring configuration and based on mechanical decoupling—In this design, the change of the stiffness and the actuator output position r is decoupled. The linear motor M_2 generates a linear displacement q_2 and is used for changing the apparent output stiffness of the actuator. The output joint position r is determined by the rotational motor M_1.

on the output without being captured by the internal elastic elements. Therefore, this working principle allows a more efficient distribution of the power flow from the control port.

The power flow analysis and the definition of the power flow ratio, as presented in this work, give important insights for the design of variable stiffness actuator and for the design of control laws.

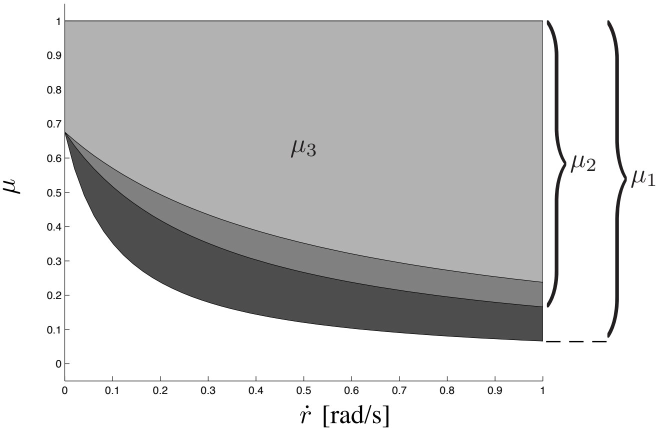

Figure 8.14: Power flow ratio μ for the design based on mechanical decoupling—The rate of change of the configuration variable $\dot{q}$ of the internal degrees of freedom is chosen so to achieve the desired changes in output position ($\dot{r}$) and stiffness ($\dot{K}$). The indicated areas μ_1, μ_2, μ_3 correspond to $\dot{K} = 0.2$ Nm/rad/s, $\dot{K} = 0.6$ Nm/rad/s and $\dot{K} = 1.0$ Nm/rad/s, respectively.

CHAPTER 9

ENERGY-EFFICIENT CONTROL OF ROBOTS WITH VARIABLE STIFFNESS ACTUATORS

Ludo C. Visser, Raffaella Carloni, Stefano Stramigioli

in: *Proceedings of the 8th IFAC Symposium on Nonlinear Control Systems*, 2010

9.1 Introduction

The research interests and efforts in variable stiffness actuators are increasing in recent years due to their broad range of possible applications. The main characteristic property of a variable stiffness actuator is that the output stiffness can be varied independently from the output position, thanks to the presence of internal actuated degrees of freedom and internal springs. This means that, if the joints of a robot are actuated by means of this class of actuators, it is possible for the robot to perform different tasks while appearing more or less compliant.

Recently, various designs of variable stiffness actuators have been introduced, for example AMASC [33], VSA [54], VS-Joint [75] and MACCEPA [61]. All these actuators use a number of internal springs with a fixed elastic constant, and the output stiffness is varied by changing the configuration of some internal degrees of freedom. In the context of safe interaction, the mechanical compliance is controlled only if an unexpected collision occurs and it is used to reduce the impact force [13].

Besides using the internal springs of a variable stiffness actuator solely to introduce a mechanical compliance to the joints for safety reasons [5], they can also be exploited to achieve more energy efficient actuation by storing negative work [52] or to change the natural frequencies of the system to match the periodicity of the motion [55]. In recent work, we presented a novel energy efficient variable stiffness actuator, characterized by the property that the output position and output stiffness are decoupled on a mechanical level [68]. This property allows the internal springs to be used as buffers to temporarily store potential energy. For example, when a disturbance occurs, the springs can store the disturbance energy, which then can be reused to bring the robot back to the desired trajectory. In particular, this approach can have big advantages in trajectory tracking [40, 17]. In such applications, the desired joint trajectories do not depend on time, and hence the potential energy stored in the springs can be used efficiently. This approach can be beneficial to walking robots, where energy efficiency is of paramount concern and trajectory tracking controllers can improve the robustness [16].

Building on our previous work, in this paper we establish a formal, port-based mathematical model for the analysis and the control of variable stiffness actuators. The port-based framework not only provides valuable insights on energy flows between the internal actuators, the springs and the robot, but it is also a solid foundation for research on innovative control methods. With the aim of achieving energy efficiency, we derive a control architecture that uses the potential energy stored in the springs to actuate the robot, instead of supplying this energy by controlling the internal degrees of freedom. We demonstrate the effectiveness of the proposed controller for a one degree of freedom system, under influence of a disturbance. In particular, if a disturbance occurs, the corresponding energy is stored in the internal springs and used for actuation. The insights gained will form a basis for future work, in which we aim to develop energy efficient coordinated control methods for a robot with multiple degrees of freedom.

9.2 Port-based Modeling of Variable Stiffness Actuators

In this Section, we intend to briefly recall the port-based generalized model of variable stiffness actuators, introduced in our previous work [68, 66], and to provide a more solid mathematical foundation, which is the basis for both the present paper and future research. The port-based framework gives valuable insights in the power flows between the controller, the variable stiffness actuator and the actuated system. Therefore, it realizes an appropriate tool for the analysis, modeling and control of systems in which energy efficiency is the main concern.

Without loss of generality, we assume that a variable stiffness actuator has the following properties:

- $n \geq 2$ internal degrees of freedom, denoted by $q \in \mathcal{Q}$, can be actuated;
- $m \geq 1$ springs, either linear or nonlinear, are internally present;
- the apparent output stiffness K of the actuator depends on both the configuration of the internal degrees of freedom and of the internal springs.

Since the aim of the model is to analyze the functional principle of a variable stiffness actuator, rather than evaluating the mechanical design, internal friction and inertias are neglected. The generic model of a variable stiffness actuator is depicted in Figure 9.1, using a bond graph representation. Each bond represents a power flow, defined positive in the direction of the half arrow and characterized by two power conjugate variables, called efforts e and flows f. If $\mathcal{F}$ is the linear space of admissible flows, then the dual space $\mathcal{E} := \mathcal{F}^*$ is the linear space of admissible efforts. For $e \in \mathcal{E}$ and $f \in \mathcal{F}$, the dual product $\langle e|f \rangle$ yields power. The Dirac structure $\mathcal{D}$ defines the interconnection of the bonds and, thus, defines how power flows from one bond to the others. The Dirac structure is power continuous, as follows from its formal definition [58]:

$$\mathcal{D} = \{\mathcal{D} \subset \mathcal{E} \times \mathcal{F} \mid \langle e|f \rangle = 0 \quad \forall\, (e, f) \in \mathcal{D}\}$$

The multidimensional $\mathbb{C}$-type *storage element* represents the springs in the device. Springs are characterized by the state $s \in \mathcal{S}$, i.e. their elongation or compression, and by the energy they store, described by the function $H : \mathcal{S} \to \mathbb{R}$. The effort e_s and flow f_s are, respectively, the forces generated by the springs and the rate of change of the states. The multidimensional *control port* is characterized by power conjugate variables τ and $\dot{q}$, i.e. the generalized forces that actuate the internal degrees of freedom and the generalized rate of change of the configuration variables. The *output port* is characterized by power conjugate variables F and $\dot{x}$, i.e. the generalized output force and the generalized output velocity, and, since it is assumed that the variable stiffness actuator is connected to a joint with one degree of freedom, it is one-dimensional. Depending on the type of actuator, the output force can be either a linear force or a torque and, correspondingly, the output position $x \in \mathcal{X}$ can either be a linear displacement or an angle. Note that the efforts τ and F do not depend on the flows $\dot{q}$ and $\dot{x}$ since a *power continuous transformation* between forces and velocities, called gyration, does not regularly exist in the mechanical domain.

The stiffness K at the output is given by

$$K = \frac{\delta F}{\delta x}$$

where δF and δx denote infinitesimal changes.

Before entering into the details of the design of the energy based control law, we further analyze this model and derive the formal mathematical structure that gives more insight into the Dirac structure and its properties.

Following the arguments above, there exists a map

$$\Gamma_{(q,x)} : \mathcal{Q} \times \mathcal{X} \to \mathcal{S}$$

that defines how the configuration of the internal degrees of freedom $q \in \mathcal{Q}$ and the output position $x \in \mathcal{X}$ determine the states $s \in \mathcal{S}$ of the springs. The tangent map $\Gamma_{(q,x)*} : T\mathcal{Q} \times T\mathcal{X} \to T\mathcal{S}$ and cotangent map $\Gamma^*_{(q,x)} : T^*\mathcal{S} \to T^*\mathcal{Q} \times T^*\mathcal{X}$

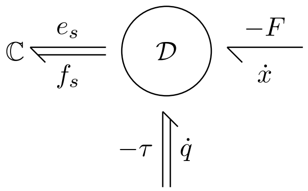

Figure 9.1: Generalized representation of a variable stiffness actuator—The Dirac structure defines the interconnection between the different bonds and, therefore, how power is distributed among the ports. The multi-bonds allow any number of springs, i.e. the $\mathbb{C}$-element, and any number of external inputs $(\tau, \dot{q})$. The output port $(F, \dot{x})$ is one-dimensional and thus a single-bond.

are naturally defined [42]. The fiber bundle $\pi_u : \mathcal{U}_q \times \mathcal{U}_x \to \mathcal{Q} \times \mathcal{X}$ has fibers $\pi_u^{-1}(q, x)$ that denote the input spaces $U_q \times U_x$. Given an input $(u_q, u_x) \in U_q \times U_x$, the internal configuration q and the output position x are subject to the dynamics $G : \mathcal{U}_q \times \mathcal{U}_x \to T\mathcal{Q} \times T\mathcal{X}$ given by

$$\dot{q} = u_q, \quad \dot{x} = u_x \tag{9.1}$$

Equation (9.1) can be written as

$$\dot{q} = \sum_{i=1}^{n} v_{q,i} u_{q,i}, \quad \dot{x} = v_x u_x \tag{9.2}$$

where

$$\begin{aligned} v_{q,i} &= (\; \underbrace{0 \;\; \cdots \;\; 0}_{i-1 \text{ elements}} \;\; 1 \;\; \underbrace{0 \;\; \cdots \;\; 0}_{n-i \text{ elements}} \;)^T \\ v_x &= 1 \end{aligned} \tag{9.3}$$

define constant input vector fields on $T\mathcal{Q} \times T\mathcal{X}$, i.e. the canonical basis for the tangent space. Since these dynamics are trivial, we allow abuse of notation and consider $\dot{q}$ and $\dot{x}$ as inputs to the system. These relations are summarized in the commutative diagram in Figure 9.2.

The dynamics of the variable stiffness actuator are

$$\begin{aligned} \dot{s} &= \Gamma_{(q,x)*}\,(\dot{q}, \dot{x}) \\ (\tau, F) &= \Gamma^*_{(q,x)}\,(\mathrm{d}H) \end{aligned} \tag{9.4}$$

where $\mathrm{d}H$ denotes the differential of the energy function H. We can see that flows are elements of the tangent spaces and efforts elements of the cotangent spaces. The Dirac structure is in the tangent maps $\Gamma_{q*} : T\mathcal{Q} \to T\mathcal{S}$, $\Gamma_{x*} : T\mathcal{X} \to T\mathcal{S}$ and the corresponding cotangent maps Γ^*_q, Γ^*_x. Via these maps, the velocities on $T_s\mathcal{S}$ at $s \in \mathcal{S}$ are defined by the velocities on $T_q\mathcal{Q} \times T_x\mathcal{X}$ at $(q, x) \in \mathcal{Q} \times \mathcal{X}$, and correspondingly the forces on $T^*_q\mathcal{Q} \times T^*_x\mathcal{X}$ by the forces on $T^*_s\mathcal{S}$, such that power continuity is preserved.

$$\begin{tikzcd}
T\mathcal{S} \arrow[d] & T\mathcal{Q} \times T\mathcal{X} \arrow[l, "\Gamma_{(q,x)*}"'] \arrow[d] & \mathcal{U}_q \times \mathcal{U}_x \arrow[l, "G"'] \arrow[dl, "\pi_u"] \\
\mathcal{S} & \mathcal{Q} \times \mathcal{X} \arrow[l, "\Gamma_{(q,x)}"'] & \\
T^*\mathcal{S} \arrow[u] \arrow[r, "\Gamma^*_{(q,x)}"] & T^*\mathcal{Q} \times T^*\mathcal{X} \arrow[u] &
\end{tikzcd}$$

Figure 9.2: Commutative diagram for a variable stiffness actuator—$\mathcal{Q}$ is the configuration manifold of the internal degrees of freedom, $\mathcal{S}$ of the state of the internal springs, and $\mathcal{X}$ of the output position.

The rate of change of the energy stored in the springs is given by [7]:

$$\dot{H} = \mathrm{d}H \ \dot{s} = \mathrm{d}H \ \Gamma_{(q,x)*}(\dot{q}, \dot{x}) \tag{9.5}$$

From (9.4) and (9.5), it can be immediately observed how the output force and the energy stored in the mechanism are related to each other, and how the rate of change of the stored energy depends on the output ports. In particular, from (9.5) it follows that the energy stored in the springs does not change due to the control input if

$$\dot{q} \in \ker \Gamma_{q*} \tag{9.6}$$

where $\ker \Gamma_{q*}$ denotes the kernel of the map Γ_{q*}. Note that the existence of this kernel depends on the mechanical design of the variable stiffness actuator [68].

9.3 Energy Efficient Control

In this Section, an energy efficient control law for variable stiffness actuators is derived. This means that, in order to achieve the energy efficiency of the controller, we intend to use the energy stored in the internal springs, if present, for the actuation of the robotic joint. First, we formulate the problem statements and, then, derive a solution that accomplishes the energy efficiency requirements. Moreover, since the fundamental demand of variable stiffness actuators is the capability of changing the output stiffness, we extend the control law with stiffness regulation.

9.3.1 Problem Statement

As depicted in Figure 9.1, the variable stiffness actuator is connected to a robotic joint with one degree of freedom. This connection is explicitly shown in Figure 9.3 by a 1-junction representing the power continuous connection

$$\dot{x} = y, \quad u = -F$$

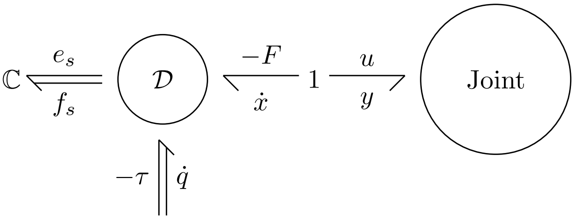

Figure 9.3: Generalized representation of a variable stiffness actuator interconnected with a robotic joint.

where (u, y) is the *interaction port* of the joint. In particular, u denotes the input force (or torque) applied to the joint, and y its velocity. We assume that full state measurement is available, i.e. for both joint and variable stiffness actuator all positions and velocities can be measured.

We now design an energetically efficient control architecture for the variable stiffness actuator, by using both the internal springs and internal actuated degrees of freedom, so that the actuator is able to apply a desired force (or torque) u_d to the joint and so that the output stiffness is regulated at a desired value. These goals are formally contained in the following problem statements.

Problem 9.1 *Consider a variable stiffness actuator, described by an energy function H and the dynamics* (9.4)*, connected to a robotic joint by a power continuous connection. Assume that full state measurement is available. How can the control inputs $\dot{q}$ to the variable stiffness actuator be designed such that the desired joint input u_d is achieved in an energy efficient way?*

Problem 9.2 *How can the control inputs $\dot{q}$ to the variable stiffness actuator be designed such that a desired joint input u_d is achieved in an energy efficient way, while at the same time the output stiffness is controlled?*

In the solutions of these two problems, we aim to exploit the internal springs of the variable stiffness actuator as buffers for storing potential energy and to use this energy to actuate the joint. In the remainder of the Section, we first derive a control law that solves Problem 9.1 in a nominal case, i.e., without considering energy efficiency. Then, we focus on refining the control law by efficiently using any potential energy stored in the springs to reduce the energy supply via the control port. Finally, we derive the stiffness control law for Problem 9.2.

9.3.2 Output Force Control

Before proceeding with the formulation of the control law, it is necessary to highlight that, if a desired input force (torque) u_d is required at the robotic joint, also the desired output force F_d of the actuator is known due to the power continuous connection. Moreover, from (9.4), the output force F, generated by the variable stiffness actuator, can be determined once the current values for q and x are given. This means that it is possible to find a control law $g_F(\cdot)$ such that the evolution in time of the force F is given by

$$\dot{F} = g_F(F_d, F)$$

as a function of the actual and the desired output force. We can then formulate a nominal control law as follows.

Lemma 9.1 (Nominal control) *Consider a variable stiffness actuator described by an energy function H and the dynamics* (9.4)*, connected to the joint of a robot through a power continuous connection. Let the vector valued function $V(q, x)$ be:*

$$V(q, x) := (L_{v_{q,1}} F, \dots, L_{v_{q,n}} F) \tag{9.7}$$

where $L_{v_{q,i}} F$ denotes the Lie-derivative of F along the vector field $v_{q,i}$. Define a subset $\mathcal{M}$ of $\mathcal{Q} \times \mathcal{X}$ as:

$$\mathcal{M} = \{(q, x) \in \mathcal{Q} \times \mathcal{X} \mid V(q, x) \neq 0\}$$

By using the control law $\dot{F} = g_F(F_d, F)$, the nominal control input

$$\dot{q}_n = V^+ \left(\dot{F} - (L_{v_x} F)\, \dot{x}\right) \tag{9.8}$$

where $^+$ denotes the Moore-Penrose pseudo inverse, solves Problem 9.1 for (q, x) in $\mathcal{M}$.

Proof: Since we defined the exact one-form $\mathrm{d}H$ on $T_s^* \mathcal{S}$, we have that (τ, F) is an exact one-form on $T_q^* \mathcal{Q} \times T_x^* \mathcal{X}$, defined by the map $\Gamma^*_{(q,x)}$ [42]. Moreover, since the input vector fields, as defined in (9.2) and (9.3) are constant, the rate of change of the one-form (τ, F) is given by

$$\frac{\mathrm{d}}{\mathrm{d}t}(\tau, F) = \begin{pmatrix} \dot{q}_1 & \cdots & \dot{q}_n & \dot{x} \end{pmatrix} \begin{pmatrix} L_{v_{q,1}}(\tau, F) \\ \vdots \\ L_{v_{q,n}}(\tau, F) \\ L_{v_x}(\tau, F) \end{pmatrix} \tag{9.9}$$

where we allowed some abuse of notation, as in (9.1). Since dim $\mathcal{X} = 1$, from (9.9) it follows that:

$$\dot{F} = V \dot{q} + (L_{v_x} F)\, \dot{x} \tag{9.10}$$

with V given in (9.7). Finally, from (9.10), the nominal controller $\dot{q}_n$ in (9.8) follows.

Note that the restriction of the solution to $\mathcal{M}$ follows from the Moore-Penrose pseudo inverse for the full row-rank matrix V [3]:

$$V^+ = V^T \left(V V^T\right)^{-1}$$

i.e., the pseudo inverse is only defined for (q, x) in $\mathcal{M}$. □

9.3.3 Energy Efficient Control

The solution derived in Lemma 9.1 is not energy efficient, since the energy stored in the springs is not taken into account. If a disturbance is present on the output port, we intend to direct the corresponding energy to the springs so to use them as energy buffer. Since our goal is to obtain solutions that efficiently use energy stored in the springs, if there is energy stored in the springs, there is, in general, no need to supply more energy via the control port.

For a particular class of variable stiffness actuators, the solution (9.8) can be modified such that any potential energy stored in the springs is efficiently used to actuate the robot. This class of actuators has the property that output position and output stiffness are decoupled on a mechanical level and, therefore, the kernel in (9.6) exists. This means that the map Γ_{q*} is surjective onto $T_s\mathcal{S}$:

$$\operatorname{rank} \Gamma_{q*} < n, \quad \forall (q,x) \in \mathcal{Q} \times \mathcal{X}$$

This property allows for a partitioning of the tangent space $T_q\mathcal{Q}$, i.e. the tangent space to $\mathcal{Q}$ at q, as:

$$T_q\mathcal{Q} = \ker \Gamma_{q*} \oplus D$$

where $\oplus$ is the direct sum and D is such that the tangent space $T_q\mathcal{Q}$ is complete. In particular, since $T_q\mathcal{Q}$ is a $\mathbb{R}$-vector space [7], we require D to be orthogonal to $\ker \Gamma_{q*}$ in the Euclidean sense. If we denote by k the dimension of $\ker \Gamma_{q*}$, i.e. $\dim\ \ker T_q\mathcal{Q} = k$, $1 \leq k < n$, and since $\dim\ T_q\mathcal{Q} = n$, it follows that $\dim\ D = n-k$.

From (9.6) it was observed that, if the control input $\dot{q} \in \ker \Gamma_{q*}$, then the energy stored in the springs does not change due to the control input. Hence, the solutions to Problem 9.1 given by (9.8) should be in $\ker \Gamma_{q*}$ or close to it when energy is stored in the springs. This can be achieved by defining on $T_q\mathcal{Q}$ an appropriate metric that weights the solutions given by the Moore-Penrose pseudo inverse [3]. This argument is formalized in the following Lemma.

Lemma 9.2 (Energy efficient control) *Consider a variable stiffness actuator described by an energy function H and the dynamics* (9.4) *and connected to the joint of a robot by a power continuous connection. Assume that the variable stiffness actuator satisfies the property*

$$\mathit{dim}\ \ker \Gamma_{q*} = k, \quad 1 \leq k < n, \quad \forall (q,x) \in \mathcal{Q} \times \mathcal{X}$$

Take on $T_q\mathcal{Q}$ two sets of local coordinates, orthogonal in the Euclidean sense, denoted by $a^1 = (a^1_1, \ldots, a^1_k)$ and $a^2 = (a^2_1, \ldots, a^2_{n-k})$, satisfying

$$\begin{aligned} \ker \Gamma_{q*} &= \mathit{span}\left\{a^1\right\} \\ D &= \mathit{span}\left\{a^2\right\} \end{aligned} \tag{9.11}$$

On $T_q\mathcal{Q}$, define a metric $\mathfrak{g}$, such that in the local coordinates (a^1, a^2) its components $[\mathfrak{g}]$ are given by

$$[\mathfrak{g}] = \begin{bmatrix} I_k & 0 \\ 0 & \alpha\, I_{n-k} \end{bmatrix} \tag{9.12}$$

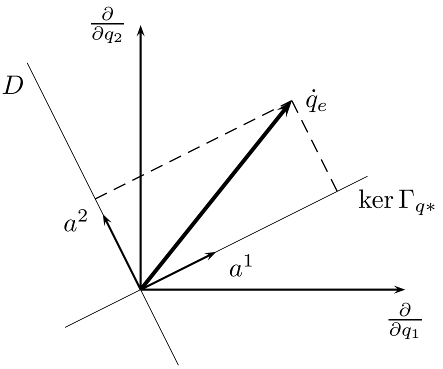

Figure 9.4: Decomposition of the energy efficient control law $\dot{q}_e$ in (9.13) into components in $\ker \Gamma_{q*}$ and in D.

with I_k *and* I_{n-k} *the identity matrix of dimension* k *and* $n-k$ *respectively, and* $\alpha : \mathcal{S} \to \mathbb{R}^+$ *a positive definite function realizing a measure for the amount of energy stored in the springs.*

Then, for (q, x) *in the subset* $\mathcal{M}$*, the control input*

$$\dot{q}_e = V^\sharp \left(\dot{F} - (L_{v_x} F)\, \dot{x} \right) \tag{9.13}$$

where $^\sharp$ *denotes the Moore-Penrose pseudo inverse with respect to the metric* $\mathfrak{g}$ *defined in* (9.12)*, solves Problem 9.1 in an energy efficient way by exploiting the energy stored in the springs.*

Proof: Using the partitioning (9.11), the solution (9.8) can be expressed into components that are either in $\ker \Gamma_{q*}$ or outside, i.e. in D. Figure 9.4 depicts a two dimensional example, in which $\left(\frac{\partial}{\partial q_1}, \frac{\partial}{\partial q_2} \right)$ denotes the canonical basis for $T_q\mathcal{Q}$, the one-dimensional spaces $\ker \Gamma_{q*}$ and D are spanned by the vectors a^1 and a^2, respectively. By choosing the metric $\mathfrak{g}$ as proposed in (9.12), the components of the solution $\dot{q}_e$ in D are weighted by α. In particular, since α is chosen such that it is proportional to the energy stored in the springs, the component in D is smaller when there is more energy available in the springs. Hence, from (9.5) it follows that, when there is more energy available in the springs, less energy is supplied via the control port. ☐

9.3.4 Stiffness Control

The control law derived in Lemma 9.2 achieves control of the joint position, but does not control the apparent stiffness of the joint. However, in many applications it is desired that the apparent joint stiffness attains some specific value. Therefore, we extend the control law with stiffness control. In particular, because of the redundancy in the internal degrees of freedom, we can define a control input, to add to any solution of Problem 9.1, so that the stiffness is controlled independently from the generated output force. This requires that the additional stiffness control $\dot{q}_{kV} \in \ker V$, so to not affect the control $\dot{q}_e$ in (9.13).

Under the assumption of full state measurement, the apparent output stiffness K of the actuator may be estimated. Given a desired output stiffness K_d, we can design a control law $g_K(\cdot)$ such that the desired rate of change of the stiffness is given by

$$\dot{K} = g_K(K_d, K)$$

If we model the stiffness K as a function on the configuration manifold, i.e. $K : \mathcal{Q} \times \mathcal{X} \to \mathbb{R}$, we can formulate a control law for the stiffness as follows.

Lemma 9.3 (Stiffness control) *Define on $T_q\mathcal{Q}$ two sets of coordinates, denoted by b^1 and b^2, satisfying:*

$$\ker V = span\left\{b^1\right\}$$
$$T_q\mathcal{Q} = span\left\{b^1, b^2\right\}$$

Determine a solution $\dot{q}_k$ that achieves the desired rate of change of the stiffness, i.e. a solution satisfying

$$\begin{pmatrix} L_{v_{q,1}}K & \cdots & L_{v_{q,n}}K \end{pmatrix} \dot{q}_k = g_K(K_d, K)$$

where $L_{v_{q,i}}K$ denotes the Lie-derivative of K along $v_{q,i}$. Denote by $\dot{q}_{kV}$ the projection of $\dot{q}_k$ onto b^1. Then, the solution to Problem 9.2 is given by the control input

$$\dot{q}_k = \dot{q}_e + \dot{q}_{kV} \tag{9.14}$$

Proof: The control input $\dot{q}_k$ is chosen such that the stiffness changes as desired, and by taking the projection onto $\ker V$, the stiffness is changed while Problem 9.1 is still solved. □

Remark 9.1 By taking the projection onto $\ker V$, it is ensured that at all times Problem 9.1 is solved. However, it follows that, in general, $\dot{q}_{kV} \neq \dot{q}_k$, and thus that the stiffness does not change exactly as desired, but as close to desired as possible. ◁

Remark 9.2 Since $\dot{q}_{kV}$ was not obtained with respect to the metric $\mathfrak{g}$ as defined in Lemma 9.2, the solution (9.14) is not necessarily energy efficient. In particular, the choice of $g_K(\cdot)$ determines the component outside $\ker \Gamma_{q*}$. ◁

9.4 Simulation Results

In this Section, we show the effectiveness of the control law derived in Section 9.3. This will be done by using a linear variable stiffness actuator design, presented in

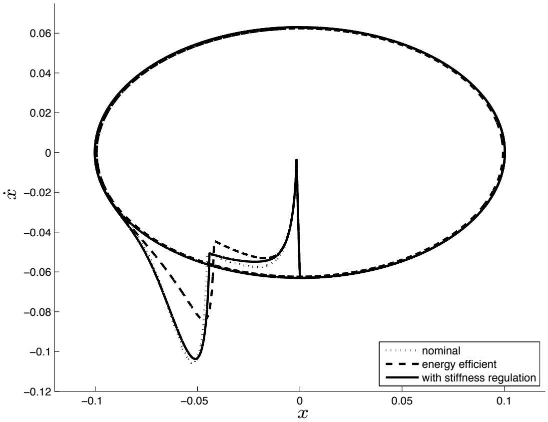

Figure 9.5: Joint phase diagram—In a periodic motion, the disturbance is similarly corrected by each control law.

earlier work [68], which satisfies the condition stated in Lemma 9.2, to actuate a joint. The experiment is as follows. The actuator moves a linear joint on a periodic motion following a sinusoidal trajectory with an amplitude of 10 cm at a frequency of 0.1 Hz. The force u_d needed to make the joint follow the trajectory is calculated using a PD-control law using the current and desired position and velocity. In the time interval $5 \leq t \leq 6$ s, the joint is subjected to a 2 N constant disturbance force. The same experiment is performed with each of the three presented control laws (9.8), (9.13), (9.14), and their performance is compared. In particular, it is investigated how each of the controllers handles the disturbance energy. The results are presented in Figures 9.5-9.7.

Figure 9.5 shows the phase space trajectory of the joint. It can be seen that the response to the disturbance is similar for each of the controllers. Note that each controller required approximately the same amount of time to return to the desired trajectory. In Figure 9.6, the energy supplied via the control port of the variable stiffness actuator is plotted. In particular, the absolute power flow through the control port is integrated, to make explicit that negative work is lost. From the numerical values, it can be seen that the energy efficient control law indeed achieves a significant reduction in energy consumption (approximately 9.6% with respect to the nominal control law). When stiffness regulation is added, the reduction in energy consumption is less (approximately 2.6%), as was expected. From Figure 9.7, the added benefit of stiffness regulation can be seen. Initially, the output stiffness is kept to a desired value of 200 N/m. When the disturbance occurs, the output stiffness increases, because the internal springs store the disturbance energy. The increase in stiffness might be an undesiderable side effect in some applications, e.g. in human-robot interaction, and thus the potential benefit of adding stiffness regulation is illustrated. However, at the same time, it is illustrated that energy

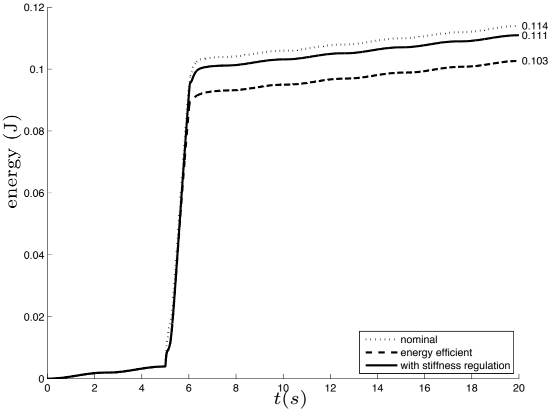

Figure 9.6: Energy supplied via the control port—The energy efficient control law clearly achieves a reduction in supplied energy. However, when stiffness regulation is added, some of the gain in efficiency is lost.

efficient control and regulating stiffness are contradicting goals.

9.5 Conclusions and Future Work

In this work, we presented an energy efficient control method for variable stiffness actuators. In addition, a stiffness regulation control was implemented, with the aim of maintaining a desired output stiffness. Simulation results illustrate the effectiveness of the proposed method. In particular, it was shown that the energy efficient control law indeed achieves a significant reduction in the energy supplied via the control port of the variable stiffness actuator by reusing energy stored in the springs. Adding stiffness regulation reduces the energy efficiency, but the controller still performs better than the nominal controller. It was found that the strict time dependency of the reference trajectory in the simulation can sometimes cause the controllers to perform poorly. This is due to the inherent oscillatory behaviour of the springs. We believe that, in limit cycle trajectory tracking applications, the advantages of the proposed control strategy will become more apparent. Since in such trajectory tracking application time is no longer restrictive, the controller may perform better by taking a state dependent response to the disturbance.

Future work will focus on controlling multiple degree of freedom systems under influence of significant disturbances, where the energy storing capabilities of the springs are more useful. The aim is to control the joints in a coordinated way, and come to an energy efficient disturbance correction. In particular, in the control of walking robots, the energy losses, associated with the impacts of the feet, can be reduced using our proposed control method.

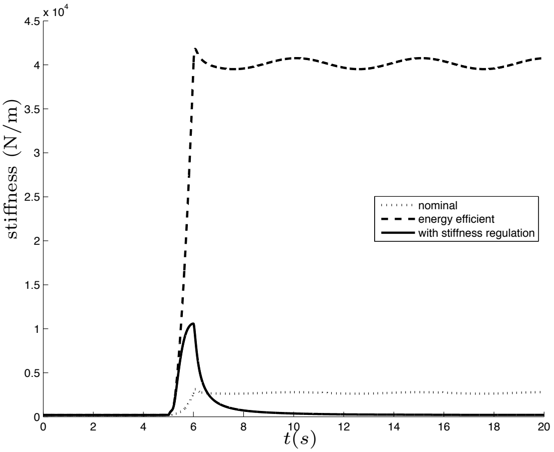

Figure 9.7: Output stiffness—Adding stiffness regulation to the control law ensures that the stiffness of the joint is kept close to a desired value of 200 N/m.

CHAPTER 10

EMBODYING DESIRED BEHAVIOR IN VARIABLE STIFFNESS ACTUATORS

Ludo C. Visser, Stefano Stramigioli, Antonio Bicchi

in: *Proceedings of the 18th IFAC World Congress*, 2011

10.1 Introduction

Variable stiffness actuators are capable of changing the apparent output stiffness independently from the output position. This is achieved by introducing one or more internal elastic elements to the actuator, and a number of actuated internal degrees of freedom that determine how the elastic elements are sensed at the output. In this way, a mechanical compliance with variable stiffness is introduced, that decouples the actuated joint from the actuator itself [5]. In many emerging robotic applications, such as walking robots, service and rehabilitation robotics, and prostheses and orthoses, physical human-robot and robot-environment interaction is an integral part, and in these cases the introduction of the mechanical compliance guarantees an intrinsic level of safety and stability. It can be seen as a mechanical implementation of impedance control [31].

In robotic applications where the motions are mostly periodic, the introduction of a mechanical compliance allows a temporary storage of energy when negative work is done by the actuator [52, 51]. By observing that the added mechanical compliance introduces an oscillatory, passive behavior to the system, it was shown by [55] that by tuning the stiffness properly to the desired motion, more energy efficient actuation of periodic motions can be achieved. The optimal stiffness was assumed to be constant, so that any costs related to changing this stiffness only become relevant when the desired motion is changed.

In this work, we show that the behavior of a variable stiffness actuator can be accurately described by the behavior of a spring with variable stiffness and equilibrium position. A cost is associated to changing the equilibrium position and the stiffness, both in terms of the deviation from the initial position and the rate of change. Then, by allowing both the equilibrium position and the stiffness to change dynamically, the desired output motion of the actuator output can be achieved optimally with respect to this cost. The cost provides a measure of embodiment of desired behavior in the passive dynamics of the variable stiffness actuator: if the deviations from the initial conditions are minimal, then the passive dynamics that the system would show when the equilibrium position and stiffness are not changed, already approaches the desired behavior as close as possible. The optimal initial conditions can be found that minimize the cost criterion.

The paper is organized as follows. Section 10.2 describes the generalized behavior of variable stiffness actuators, with the aim of rendering our approach independent from specific actuator designs. Then, in Section 10.3, the problem is formally stated and explained in detail. In Section 10.4, a nominal solution to the problem is provided, which is then optimized according to the cost criterion in Section 10.5. The effectiveness of our approach is illustrated by algebraic and simulation examples in Section 10.6. Concluding remarks and an outline for future work is given in Section 10.7.

10.2 Generalized Behavior of Variable Stiffness Actuators

In this Section, we present a port-Hamiltonian model for variable stiffness actuators. This model is an extension of the model presented by [68]. Furthermore, we propose a change of coordinates to capture the behavior of the variable stiffness actuator, irrespective of the particular actuator design.

10.2.1 Generic Port-Hamiltonian Model of Variable Stiffness Actuators

A generic port-based model for variable stiffness actuators was introduced by [68], in which it was assumed that:

- the variable stiffness actuator has a number of internal elastic elements, described by a state s and an energy function $H_s(s)$ describing the storage of elastic energy;
- there are a number of actuated internal degrees of freedom, with configuration variables q;

- the behavior at the actuator output, with one degree of freedom, is determined by the intrinsic properties of the elastic elements and the configuration of the internal degrees of freedom.

Moreover, since the model aims to capture the working principle of the variable stiffness actuator, internal inertias and friction were not incorporated in the model. Under these assumptions, it was shown that the actuator behavior can be accurately described in a port-based setting by:

$$\begin{bmatrix} \dot{s} \\ \tau_q \\ \tau_r \end{bmatrix} = \underbrace{\begin{bmatrix} 0 & A(q,r) & B(q,r) \\ -A^T(q,r) & 0 & 0 \\ -B^T(q,r) & 0 & 0 \end{bmatrix}}_{D_0(q,r)} \begin{bmatrix} \frac{\partial H_s}{\partial s} \\ \dot{q} \\ \dot{r} \end{bmatrix} \tag{10.1}$$

where the skew-symmetric matrix $D_0(q,r)$ describes the power continuous port interconnection. In particular, a *storage port*, an *output port* and a *control port* can be identified. The storage port is described by the power conjugate pair $(\dot{s}, \frac{\partial H_s}{\partial s})$, where $\dot{s}$ denotes the rate of change of the state s of the elastic elements and $\frac{\partial H_s}{\partial s}$ denotes the force generated by these elements. The output port is described by the pair $(\dot{r}, \tau_r)$, with $\dot{r}$ the rate of change of the output position r, and τ_r the collocated force. The pair $(\dot{q}, \tau_q)$ describes the control port, where $\dot{q}$ denotes the rate of change of the configuration variables q, and τ_q are the generalized collocated forces. The matrices $A(q,r)$ and $B(q,r)$ are the algebraic Jacobians of the kinematic relation $\lambda : (q,r) \mapsto s$, that relates the actuator output position r and the configuration q of the internal degrees of freedom to the state s of the internal elastic elements. In particular:

$$A(q,r) := \frac{\partial \lambda}{\partial q}, \quad B(q,r) := \frac{\partial \lambda}{\partial r}$$

The description (10.1) assumes ideal internal actuators, and thus velocity control of $\dot{q}$. In practice however, the internal actuators have an inertia, and the torque required to achieve a certain desired $\dot{q}$ follows from the formulation of an appropriate control law. Extending (10.1) to include these internal inertias is straightforward. Letting $M = \mathrm{diag}(m_1, \ldots, m_n)$ denote the constant inertia matrix, we then obtain the following Hamiltonian energy function:

$$H(\rho, s) = \frac{1}{2}\rho^T M^{-1} \rho + H_s(s) \tag{10.2}$$

where $\rho = M\dot{q}$ denotes the momenta of the internal degrees of freedom. It can be shown that (10.1) can then be expanded as:

$$\begin{bmatrix} \dot{s} \\ \dot{\rho} \\ \dot{q} \\ \tau_r \end{bmatrix} = \underbrace{\begin{bmatrix} 0 & A(q,r) & 0 & B(q,r) \\ -A^T(q,r) & 0 & -1 & 0 \\ 0 & 1 & 0 & 0 \\ -B^T(q,r) & 0 & 0 & 0 \end{bmatrix}}_{D(q,r)} \begin{bmatrix} \frac{\partial H}{\partial s} \\ \frac{\partial H}{\partial \rho} \\ \tau \\ \dot{r} \end{bmatrix} \tag{10.3}$$

Where $D(q,r)$ is a skew-symmetric matrix representing the extended Dirac structure. The power conjugate pair $(\dot{q}, \tau)$ defines the new control port.

10.2.2 Change of Coordinates

The behavior of a variable stiffness actuator, seen at the output, is essentially the behavior of a *linear* spring, of which the equilibrium position and the stiffness can be changed [43]. We propose a change of coordinates

$$S : q \mapsto \tilde{q}, \quad \tilde{q} := (\bar{r}, k) \tag{10.4}$$

where $\bar{r}$ denotes the equilibrium output position, and k the apparent output stiffness, defined hereafter, to capture the behavior of the variable stiffness actuator in terms of these quantities.

The equilibrium position $\bar{r}$ of the actuator output is, by definition, the position r for which $\dot{r} = 0$ and remains zero, i.e., the position r for which the potential (elastic) energy function attains a minimum. Given a configuration q of the internal degrees of freedom, and $\dot{q} = 0$, we thus have

$$\begin{aligned} \bar{r} &= \arg\min_r H(\rho, q, r) \\ &= \arg\min_r (H_s \circ \lambda)(q, r) \end{aligned} \tag{10.5}$$

where the second equality follows from q and r being stationary and from the Hamiltonian energy function being quadratic in the momentum variables. The apparent output stiffness follows from the definition of the stiffness:

$$k := \frac{\delta \tau_r}{\delta r} \tag{10.6}$$

i.e., the infinitesimal force generated by an infinitesimal change in output position. Note that the stiffness is a local property, thus (10.6) is only valid for stationary configurations $\dot{q} = 0$ and $\dot{r} = 0$. From (10.3) and the kinematic relation λ, the force at the output is $\tau_r = \frac{\partial}{\partial r} H_s(s \circ \lambda)$, and thus we obtain that the apparent output stiffness is given by:

$$\begin{aligned} k &= -\frac{\partial^2 H}{\partial r^2}(q, r) \\ &= -\frac{\partial^2 (H_s \circ \lambda)}{\partial r^2}(q, r) \end{aligned} \tag{10.7}$$

where the second equality again follows from q and r being stationary. Observe that both $\bar{r}$ and k are not functions of r, as they are only defined for a particular value of r.

Using (10.5) and (10.7), the change of coordinates S is obtained, and it follows that, for a given configuration (q, r),

$$\dot{\tilde{q}} = \frac{\partial S}{\partial q} \dot{q} \tag{10.8}$$

Assumption 10.1 The change of coordinates (10.8) is a diffeomorphism and independent of q. ●

Commonly encountered variable stiffness actuator designs, for example the antagonistic design that is the basis of the VSA-I presented by [54], or the design of the VS-Joint by [75], satisfy this assumption. Under this assumption, the dynamics (10.3) can be rewritten in the new coordinates by transforming the momenta ρ into the new coordinates, denoted by $\tilde{\rho}$. Correspondingly, the new inertia matrix $\tilde{M}$ is obtained as

$$\tilde{M} = \left(\tfrac{\partial S}{\partial q}\right)^{-T} M \left(\tfrac{\partial S}{\partial q}\right)^{-1} \tag{10.9}$$

Then, in the new coordinates, the Hamiltonian energy function becomes

$$\tilde{H}(\tilde{\rho}, \tilde{q}, r) = \frac{1}{2}\tilde{\rho}^T \tilde{M}^{-1}\tilde{\rho} + (H_s \circ \lambda)(S^{-1}(\tilde{q}), r)$$

The dynamic equations in port-Hamiltonian form readily follow, with a new control port $(\tilde{\tau}, \dot{\tilde{q}})$.

For notational convenience, we introduce the following variables for the remainder of this paper:

$$x = \begin{bmatrix} x_1 \\ x_2 \\ x_3 \\ x_4 \end{bmatrix} := \begin{bmatrix} r \\ \dot{r} \\ \bar{r} \\ k \end{bmatrix}$$

Proposition 10.1 *Due to the change of coordinates* (10.4)*, the behavior of the variable stiffness actuator can be described in the form*

$$\begin{aligned} \dot{x}_1 &= x_2 \\ \dot{x}_2 &= \tfrac{1}{m} x_4 (x_3 - x_1) \\ \dot{x}_3 &= u_1 \\ \dot{x}_4 &= u_2 \end{aligned} \tag{10.10}$$

or:

$$\dot{x} = f(x) + g_1\, u_1 + g_2\, u_2$$

where $x \in \mathcal{M}$ denotes the state as element of the state manifold $\mathcal{M}$, $f(x)$ is the drift vector field, and g_1 and g_2 are the constant control input vector fields.

Remark 10.1 We note that, since x_4 corresponds to a stiffness, which is a positive definite quantity, the state manifold $\mathcal{M}$ has a border. Therefore, any solution that is obtained in what follows is only valid if it remains in the bounded set $\{x \in \mathcal{M} \mid x_4 > 0\}$. ◁

10.3 Problem Formulation

The goal of this work is to embed desired behavior into the variable stiffness actuator as much as possible. Consequently, the desired behavior should be represented in the form of a dynamical system, so that it is meaningful to let the autonomous part of (10.10) approach the desired behavior.

Assumption 10.2 The desired periodic motion of the actuator can be described in the phase space (x_1, x_2) by a dynamical system of the form:

$$\begin{aligned} \dot{x}_1 &= x_2 \\ \dot{x}_2 &= a(x_1) - \gamma \end{aligned} \tag{10.11}$$

implying that the desired motion $x_1(t)$ is bounded and at least twice continuously differentiable. •

Assumption 10.3 Because (10.10) describes a physical system, the desired motion is such that it can be achieved with finite inputs u. •

Remark 10.2 Note that we do not allow $a(\cdot)$ to be a function of x_2, as this would imply damping, which will not result in a periodic motion. Only if this damping is nonlinear and satisfies certain properties, such a description can result in periodic behavior. For example, the solutions to Liénard systems are, when certain conditions are met, limit cycles in the phase space [53]. This topic is considered beyond the scope of this paper. ◁

By combining (10.10) and (10.11), we can define a function $\Gamma(x)$:

$$\Gamma(x) = \tfrac{1}{m} x_4 (x_3 - x_1) - a(x_1) \tag{10.12}$$

i.e., $\Gamma(x)$ defines which output force must be generated to follow a desired trajectory. It follows that $\Gamma(x)$ defines foliations $\mathcal{N}_\gamma \subset \mathcal{M}$ described by

$$\mathcal{N}_\gamma = \{x \in \mathcal{M} \mid \Gamma(x) = \gamma\}$$

The goal of this work is to find an input u, such that the system remains on the foliation for a given desired motion (10.11), with minimum effort, i.e., with the smallest control input and minimal deviations of x_3 and x_4 from the initial conditions. This can be formally stated as follows.

Problem 10.1 *Given a desired motion of the actuator output, described by* (10.11)*, find initial conditions* $x^\circ = x(0)$*,* $x^\circ \in \mathcal{N}_\gamma$*, and a control input* u*, such that the criterion*

$$J = \int_0^\infty \frac{1}{2} \|x_3^\circ - x_3\|_{\bar{r}}^2 + \frac{1}{2} \|x_4^\circ - x_4\|_k^2 + \frac{1}{2} \|u\|_u^2 \, dt \tag{10.13}$$

is minimized for given weighted 2*-norms* $\| \cdot \|_*$.

The integrand of (10.13) can be interpreted as a Hamiltonian energy function. Thus, minimizing J corresponds to finding the optimal trajectories $x_3(t)$ and $x_4(t)$ with respect to this energy function. Note that there are two parts in the integrand, and optimizing J means finding a trade-off between those two parts: the first two terms associate a cost to the deviation from the initial conditions, and the last term associates a cost to the rate of change of x_3 and x_4. In particular, the first two terms in fact formulate a measure of embodiment of the desired behavior into the variable stiffness actuator: if the deviations from the initial conditions of x_3 and x_4 are small, it means that the initial values for x_3 and x_4 result in an intrinsic passive behavior that is already close to the desired behavior.

Remark 10.3 It will be shown that there is a cost associated to u that naturally arises from physical considerations. However, there is no such physical cost for the deviations of x_3 and x_4. These costs are associated with changing the equilibrium position and the stiffness, and may be defined by the design of the actuator, by an analysis of desired disturbance rejection, or some other analysis. $\triangleleft$

10.4 Nominal Solution

The first step in solving Problem 10.1 is showing that there exists at least one solution to the problem. The approach will be in two parts: first we establish that there exists an input u such that the system (10.10) exhibits the desired motion (10.11) in the plane (x_1, x_2), and then we will infer that the obtained solution curves allow a minimization of the criterion (10.13).

10.4.1 Nominal Control Input

Given the desired motion (10.11) and the corresponding $\Gamma(x)$ as defined in (10.12), we extend the system description (10.10) by defining an output function $h(x) = \Gamma(x) - \gamma$. Then, given initial conditions $x^\circ \in h^{-1}(0)$, it is possible to compute the maximal controlled invariant output-nulling submanifold. In particular, following the algorithm presented by [42], we obtain the following.

First, we define the submanifold $\mathcal{Z}_1 \subset \mathcal{N}_\gamma \subset \mathcal{M}$ by

$$\mathcal{Z}_1 = \{x \in \mathcal{M} \mid h(x) = 0\}$$

This submanifold is of dimension three, because the restriction of the output function being zero defines a curve of dimension one. With $x^\circ \in \mathcal{Z}_1$, the system dynamics remain in $\mathcal{Z}_1$ for all time, if $\dot{h}(x) = 0$ for all time. We calculate

$$\begin{aligned}\frac{d}{dt}h(x) &= L_f h(x) + L_{g_1} h(x)\, u_1 + L_{g_2} h(x)\, u_2 \\ &= L_f \Gamma(x) + \begin{bmatrix} L_{g_1}\Gamma(x) & , & L_{g_2}\Gamma(x) \end{bmatrix} \begin{bmatrix} u_1 \\ u_2 \end{bmatrix}\end{aligned}$$

with

$$L_f\Gamma(x) = \left(-\frac{1}{m}x_4 - \frac{\partial a}{\partial x_1}\right)x_2$$

i.e., the Lie-derivative of $\Gamma(x)$ along the drift vector field $f(x)$, and similarly the Lie-derivatives of $\Gamma(x)$ along the control input vector fields:

$$\begin{bmatrix}L_{g_1}\Gamma(x) & , & L_{g_2}\Gamma(x)\end{bmatrix} = \begin{bmatrix}\frac{1}{m}x_4 & , & \frac{1}{m}(x_3 - x_1)\end{bmatrix} =: \mathcal{A}(x)$$

Since, as remarked before, x_4 is always nonzero, $\mathcal{A}(x)$ nonsingular for all x, and thus there always exists an input u, such that $\mathcal{A}(x)u + L_f\Gamma(x) = 0$. Define the submanifold $\mathcal{Z}_2 \subset \mathcal{Z}_1$ by

$$\mathcal{Z}_2 = \{x \in \mathcal{Z}_1 \mid \dot{h}(x) = 0\}$$

This submanifold is of dimension two, due to the added restriction of $\dot{h}(x) = 0$. We can take for u a combination of a state feedback and a new input v:

$$u = -\mathcal{A}^R(x)\,L_f\Gamma(x) + \mathcal{A}^\perp(x)v \tag{10.14}$$

where $\mathcal{A}^R$ denotes a right inverse of $\mathcal{A}$, and $\mathcal{A}^\perp$ is the annihilator for $\mathcal{A}$. Then, for initial conditions $x^\circ \in \mathcal{Z}_2$, the input (10.14) ensures that the system remains in $\mathcal{Z}_2$, and thus $\mathcal{Z}_2 =: \mathcal{Z}^*$ is the maximal controlled invariant output-nulling submanifold. Or, in other words, any trajectory $x(t)$ that is a solution to (10.10), subject to the input (10.14), will show the desired motion (10.11) in the plane (x_1, x_2) if the initial conditions $x^\circ \in \mathcal{Z}^*$.

Remark 10.4 Because $\mathcal{A}(x)$ is not full rank, (10.14) defines infinitely many solutions. It is well known that the weighted pseudo inverse is a right inverse that gives a solution of minimum norm with respect to a metric [3]. Therefore, in the context of optimizing (10.13), in (10.14) the pseudo inverse should be taken with respect to the metric defining the norm $\|\cdot\|_u$, and $v \equiv 0$.

Inspection of the third row of (10.3) reveals that, at the port $(\dot{q}, \tau)$, the infinitesimal change $\delta\dot{q}$ as a result of an infinitesimal change of applied control torque $\delta\tau$ is, using the energy function (10.2), given by:

$$\frac{\delta\dot{q}}{\delta\tau} = \frac{\partial^2 H}{\partial\rho^2} = M^{-1}$$

Hence, the metric defined by M is a useful metric to measure a change of $\dot{q}$. Since the input $u = \dot{\tilde{q}}$ is defined in the new coordinates $\tilde{q}$, a meaningful choice for the metric inducing the norm $\|\cdot\|_u$ is the pseudo mass matrix $\tilde{M}$ defined in (10.9). Using the definition of the norm, we obtain

$$\frac{1}{2}\|u\|^2_{\tilde{M}} = \frac{1}{2}u^T\tilde{M}u$$

which has indeed the units of energy, as we observed in defining the integrand of (10.13). ◁

10.4.2 Bounded Solutions

Optimization of the criterion (10.13) is only meaningful if the solutions $x_3(t)$ and $x_4(t)$ remain in some bounded neighborhood of the initial conditions (x_3°, x_4°). It is tempting to assume, since the motion in the plane (x_1, x_2) is periodic, that also the solutions (x_3, x_4) are periodic. However, this assumption may not be valid, since the solution $x(t)$ can be chaotic while still the projection onto (x_1, x_2) gives the desired periodic motion. However, by investigation of (10.14), we can deduce some properties of the solution $x(t)$ of the system (10.10), (10.14).

The desired motion is described in (10.11) by a dynamic system without damping, and thus of the form $\ddot{x}_1 = a(x_1) - \gamma$. For $v \equiv 0$, (10.14) is differentiable, because $\mathcal{A}(x)$ is nonsingular (see Remark 10.1) and bounded by Assumption 10.3. Defining $z := (x_1, x_3, x_4)$, it follows that on a closed and finite time interval, $\dot{z}$ is bounded and C^1, and that $\ddot{z}$ is finite. Therefore, we can write the system dynamics as

$$\ddot{z} = F(z)$$

where $F(z)$ is a function that depends on the state z of the system only, because due to (10.11) and the restriction to $\mathcal{Z}^*$, the feedback in (10.14) can be found in terms of x_1, x_3, x_4 only. If it is possible to find a potential energy function $U(z)$ such that

$$F(z) = -\frac{\partial U}{\partial z}$$

then the system is conservative. Then, assuming $\dot{z}(0) = 0$, due to the law of conservation of energy all solutions $z(t)$ remain in the ellipse $U(z) \leq U(z(0))$ [2].

However, $U(z)$ may not exist, or it may be unbounded or not smooth. Therefore, at this point, no strict conclusions may be drawn about the boundedness of the solutions of $x(t)$. But, if $U(z)$ does not exist and thus that the system is not conservative, this implies that there is energy injection or dissipation, which may be countered by a proper choice for the additional input v. As stated, the optimization of (10.13) is only meaningful if the solution $x(t)$ is bounded, and therefore we will assume the following.

Assumption 10.4 For a desired motion described by (10.11), starting from initial conditions $x^\circ \in \mathcal{Z}^*$, there is a v such that the solution $x(t)$ of the system (10.10), (10.14), remains within an ellipse defined by the initial conditions. •

Remark 10.5 The preceding analysis implies that $v \equiv 0$ should give the desired behavior. Simulation examples in Section 10.6 show that this is indeed the case for some nontrivial periodic motions in (x_1, x_2). ◁

10.5 Optimization

In the previous Section, it was established that the maximal controlled invariant output-nulling submanifold $\mathcal{Z}^*$ is of dimension 2. One dimension corresponds to the desired motion in (x_1, x_2), leaving one degree of freedom in (x_3, x_4). As mentioned before, taking the pseudo inverse in (10.14) with respect to the desired norm on u in (10.13) results in that the term $\frac{1}{2}\|u\|_u^2$ is already minimized among all possible solutions. This leaves the remaining two terms to be minimized by a proper choice of the initial conditions (x_3°, x_4°).

In general, the optimization problem cannot be solved analytically. Therefore, we propose a variation on the line search algorithm that exploits the fact that there is only one degree of freedom left in the choice for the initial conditions (x_3°, x_4°), due to the restriction to $\mathcal{Z}^*$. It is not possible to find the gradient descent of J with respect to (x_3°, x_4°) analytically, but since there is only one degree of freedom to search in, the following algorithm can be effectively executed.

Step 0**:** Choose initial conditions (x_1°, x_2°) for the duration of the algorithm. Determine an initial guess for $x_3^{\circ,1}$ and calculate $x_4^{\circ,1}$ such that $x^{\circ,1} \in \mathcal{Z}^*$. Choose an initial step-size ε_1.

Step $k > 0$**:** Determine the gradient descent direction:

- Calculate the cost J_k according to (10.13), by simulating the system (10.10), (10.14) for a number of periods, starting from initial conditions $x^{\circ,k}$.
- Compute J_k^+ and J_k^- by computing the costs starting from initial conditions $x_3^{\circ,k} + \varepsilon_k$ and $x_3^{\circ,k} - \varepsilon_k$ (and corresponding initial values x_4) respectively.
- Determine $J_{k+1} = \min(J_k^+, J_k^-)$.
- If $J_k - J_{k+1}$ is smaller than a threshold δ, terminate the algorithm: the corresponding initial conditions minimize (10.13). Otherwise, continue with the corresponding initial values and set $\varepsilon_{k+1} = \varepsilon_k/2$.

Remark 10.6 Successful convergence of this algorithm relies on the assumption that, since J is quadratic, it has at least a local minimum. Reaching the global minimum depends on the initial guess $x_3^{\circ,1}$, the threshold value δ, and the initial stepsize ε_1. $\triangleleft$

10.6 Examples

In this Section, we illustrate the results of the preceding Sections with two examples. The first example is the harmonic oscillator, which has optimal values for (x_3°, x_4°) that can be determined a priori. In the second example, the Duffing oscillator is used to illustrate the effectiveness of the optimization process for nontrivial periodic motions.

10.6.1 The Harmonic Oscillator

The harmonic oscillator with unit frequency and amplitude is described in the form (10.11) as:

$$\dot{x}_1 = x_2, \quad \dot{x}_2 = -x_1$$

which admits the analytical solution

$$x_1(t) = \cos t, \quad x_2(t) = -\sin t$$

It follows that the submanifold $\mathcal{Z}_1$ is defined as

$$\mathcal{Z}_1 = \{x \in \mathcal{M} \mid \tfrac{1}{m} x_4(x_3 - x_1) + x_1 = 0\}$$

It is well known that the harmonic oscillator can be implemented by tuning the stiffness to the frequency of the desired oscillation, i.e., choosing k such that $\omega = \sqrt{k/m}$. In this example, we have $m = 1$ and $\omega = 1$, and thus taking $k = 1$ gives the desired motion. Indeed, taking $x_3^\circ = 0$ and $x_4^\circ = 1$ results in initial conditions that are in $\mathcal{Z}_1$ for any (x_1°, x_2°). Moreover, we compute $L_f\Gamma(x)$, with $a(x_1) = -x_1$, we obtain

$$\begin{aligned} L_f\Gamma(x) &= \left(-x_4 - \frac{\partial a}{\partial x_1}\right) x_2 \\ &= (-x_4 + 1)x_2 \end{aligned}$$

which is always equal to zero for $x_4 = 1$. Hence, the control input u can remain zero, and the cost (10.13) is trivially minimized. This illustrates perfectly the principle of embedding desired behavior.

10.6.2 The Duffing Oscillator

Duffing's equation was originally introduced to model nonlinear oscillations with a hardening stiffness effect, but it provides in general an example for studying nonlinear oscillations [27]. In this example, the undamped Duffing oscillator is considered, which takes the form:

$$\ddot{x}_1 + \beta x_1 + \alpha x_1^3 = \gamma \tag{10.15}$$

with $\alpha > 0$. Oscillations of this type can be formulated in the form of (10.11) by taking $a(x_1) = -\beta x_1 - \alpha x_1^3$. To compute the maximal controlled invariant submanifold $\mathcal{Z}^* \subset \mathcal{N}_\gamma \subset \mathcal{M}$, we first compute

$$\mathcal{Z}_1 = \{x \in \mathcal{M} \mid \Gamma(x) + \gamma = 0\}$$

with

$$\Gamma(x) = -\beta x_1 - \alpha x_1^3 - x_4(x_3 - x_1)$$

Table 10.1: Parameter values

Desired motion	(x_1°, x_2°)	$(-2, 0)$
	α, β, γ	$1, -2, 3$
Cost criterion	$\|\cdot\|_{\bar{r}}$	$\|\cdot\|$ (2-norm)
	$\|\cdot\|_k$	$\|\cdot\|$ (2-norm)
	$\|\cdot\|_u$	$\|\cdot\|_{\tilde{M}}$ (weighted 2-norm with $\tilde{M} = \text{diag}(1, 4)$)
Optimization	δ	0.005
	ε_1	0.2

It follows, for any initial conditions (x_1°, x_2°), that (x_3°, x_4°) must satisfy:

$$x_4^\circ = \frac{-\beta x_1^\circ - \alpha x_1^{\circ 3} + \gamma}{x_3^\circ - x_1^\circ}$$

Using this relation, the algorithm presented in Section 10.5 is executed, with the parameter values presented in Table 10.1. Setting the cost for both x_3 and x_4 equally in the cost criterion (10.13) implies that there is no preference on using either one. Note, however, that there are different costs associated with dynamically changing x_3 and x_4, indicated by $\tilde{M} = \text{diag}(1, 4)$. For the initial guess of $x_3^{\circ,1}$, we take the average of the solution to (10.15).

Figure 10.1 shows the solution curves of the system (10.10), (10.14) in the plane (x_1, x_2). Both the initial solutions and the optimal solution, according to the algorithm of Section 10.5, are shown, but cannot be distinguished. The $\circ$ indicates the initial guess $x_3^{\circ,1}$ for the algorithm, and the $+$ the optimal x_3°. Figure 10.2 shows the components x_3 and x_4 of both solutions. It can be clearly seen that the optimal solution (solid black curve) achieves smaller excursions from the initial conditions (dashed curves). It is noted that both the solutions x_3 and x_4 are reduced comparatively (observe the scales of the vertical axes).

The cost criterion (10.13) is calculated over a time span of 100 s. For the optimal solution found by the algorithm, a numerical value of $J = 141.374$ is found. A fine-gridded brute force calculation of the cost for all possible initial conditions finds a minimum of $J = 141.316$, illustrating the effectiveness of the algorithm. To illustrate that it makes sense to have a varying stiffness, the process is repeated with the same parameter values, but with $u_2 \equiv 0$, i.e. a fixed stiffness. The algorithm then finds an optimal cost of $J = 158.397$ (brute force: $J = 155.998$), which is higher than obtained with the variable stiffness, even though we assigned a higher cost to the dynamic changes of the stiffness with respect to the equilibrium position.

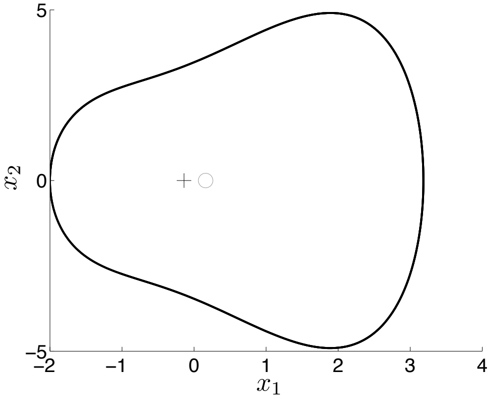

Figure 10.1: Solutions in the plane (x_1, x_2)—The $\circ$ indicates the initial guess $x_3^{\circ,1}$, and the $+$ the optimal initial value for x_3.

10.7 Conclusions and Future Work

In this paper, a cost criterion was proposed, that formulates a measure of embodiment of desired behavior into a variable stiffness actuator. In particular, minimization of the cost criterion achieves a desired output motion with minimum control effort. The effectiveness of this approach was illustrated in an algebraic and a simulation example. Currently, the algorithm is being implemented on a test setup, and experimental results will be reported in a future article.

Future work will focus on how the behavior of the variable stiffness actuator should change in case of a disturbance, considering the fact that the disturbance will add energy to the system that may be used efficiently for actuation. Furthermore, extensions to multi degree of freedom systems need to be formulated. Rather than considering each degree of freedom separately, it should be investigated if a coordinated approach to embodiment of desired behavior in all degrees of freedom is possible.

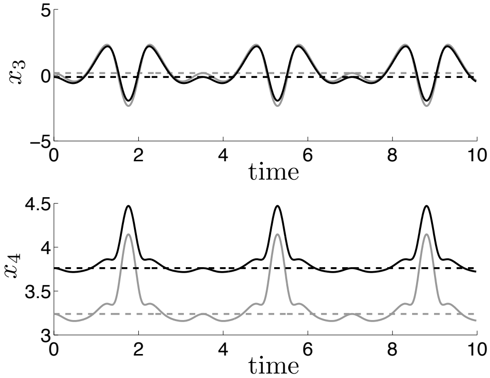

Figure 10.2: Solutions (x_3, x_4)—The grey curves correspond to the first step of the algorithm of Section 10.5, the black curves to the optimal solution, with the dashed lines indicating the initial values.

CHAPTER 11

Energy-Efficient Bipedal Locomotion using Variable Stiffness Actuation

Ludo C. Visser, Raffaella Carloni, Stefano Stramigioli

submitted to: *IEEE Transactions on Robotics*, 2013

11.1 Introduction

Robust and energy efficient bipedal locomotion in robotics is an interesting research topic with many open questions. In particular, on one side of the spectrum, robust bipedal robots are being developed, but without much consideration for energy efficiency [6]. On the other side of the spectrum, extremely efficient bipedal locomotion is being achieved by exploiting passive robot dynamics [11]. However, the gaits of such passive dynamic walkers lack robustness [47].

Human walking is both robust and energy efficient, and a better understanding of human walking could lead to the design of robots achieving similar performance levels. To develop this understanding, models have been proposed that capture the essential properties of human gaits. One remarkably simple model is the bipedal spring-loaded inverted pendulum (SLIP) model, proposed in [21]. Despite its simplicity, the model accurately reproduces the hip trajectory and ground reaction force profiles observed in human gaits. Furthermore, the model encodes a wide variety of gaits, ranging from slow walking to running, each with characteristic robustness properties [44].

It has been shown that the bipedal SLIP model can be used to generate reference gaits for a fully actuated bipedal robot [20, 38]. However, the human musculoskeletal system enables the leg stiffness to be varied continuously, in order to adapt to different gaits and terrains. These stiffness variations also play a role in disturbance rejection, for example in uneven terrain with sudden and unexpected changes in the walking surface. Variable stiffness in the legs of the bipedal SLIP walker has been shown to increase energy efficiency [57, 22] and improve robustness [36]. Recent advances in the field of variable stiffness actuators, a class of actuators that allow the actuator output stiffness to be changed independently from the actuator output position [62], are enabling the realization of robotic walkers with physically variable leg stiffness. Therefore, further research into bipedal walking with variable leg stiffness should be pursued, with the aim of getting closer to realizing bipedal walking robots with human-like performance characteristics.

In this work, we present a constructive method for modeling and controlling bipedal robotic walkers with controllable leg stiffness, starting from the conventional bipedal SLIP model. We iteratively extend this model, first by making the stiffness controllable, then by adding a swing leg and its dynamics, and then further by including a knee in the swing leg. In parallel, we derive a control strategy, which is extended with each model iteration. For each iteration, we prove the stabilizing properties of the controller, showing that the controller derived for the anchor model in the first iteration is sufficiently robust to handle the increasingly complex dynamics in subsequent iterations. Furthermore, it is shown that the controller is energy-efficient by exploiting the compliance of the legs. This model and controller can serve as a template for bipedal robot control strategies.

The paper is organized as follows. In Section 11.2, we revisit the bipedal SLIP model, as presented in [21], and analyze its dynamics. Then, in Section 11.3, we extend the bipedal SLIP model to have controllable stiffness (the V-SLIP model, for Variable SLIP), and derive a control strategy that renders a natural gait of the SLIP model asymptotically stable. In Section 11.4, the controlled V-SLIP model is extended to include feet, with the aim of introducing swing leg dynamics. The V-SLIP control strategy is extended to handle the extra degrees of freedom, and the stabilizing properties of the controller are demonstrated. The swing leg model is further refined in Section 11.5 by adding knees, with again further extension of the control strategy. A comparison of the models and their controllers is presented in Section 11.6, and Section 11.7 concludes the paper with a discussion and final remarks.

Conventions in Notation

To avoid notational clutter, variable names will be reused for different models. However, this reuse is consistent, and variables with the same name indicate the same quantity in the various models. For example, q_i denotes configuration variables, and p_i denotes momentum variables, state vectors are named x, and $f(x)$ and $g_i(x)$ are drift and input vector fields on the state manifold respectively. The Lie-derivative of a function h along a vector field X is denoted by $\mathcal{L}_X h$. Function arguments are omitted where this is considered possible.

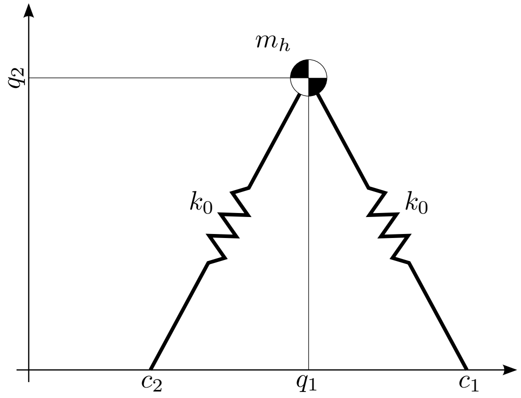

Figure 11.1: The bipedal SLIP model—The model consists of a point mass m_h, located in the hip joint, i.e. where two massless telescopic springs, with a constant spring stiffness k_0 and rest length L_0, are connected. The configuration variables (q_1, q_2) describe the position of the hip.

11.2 The Bipedal SLIP Model

In this Section, we revisit the bipedal SLIP model, as presented in [21]. The model is depicted in Fig. 11.1. It consists of a point mass m_h, located in the joint connecting the two legs, i.e. the hip joint. The legs consist of massless telescopic springs of stiffness k_0 and rest length L_0. The configuration variables $(q_1, q_2) =: q$ describe the planar position of the point mass, with $(p_1, p_2) =: p$ the associated momentum variables. In the following, we derive the dynamic equations for this system, and analyze its dynamics.

11.2.1 System Dynamics

The bipedal SLIP model shows, for appropriately chosen initial conditions [21, 44], a passive walking gait as illustrated in Fig. 11.2. In order to derive the dynamic equations that describe the gait of this model, two phases need to be considered: 1) two legs are in contact with the ground (i.e. the double support phase), and 2) one leg is in contact with the ground (i.e. the single support phase). Furthermore, we consider the parameter α_0, which is the angle at which the massless leg touches down at the end of the single support phase, as indicated in Fig. 11.2.

The contact conditions are determined by the spring rest length L_0 and angle of attack α_0, as shown in Fig. 11.2. In particular, if the system is in the single support phase, the touchdown event of the other leg occurs when

$$q_2 = L_0 \sin(\alpha_0), \tag{11.1}$$

and at this moment the foot contact point c_2 is calculated as

$$c_2 = q_1 + L_0 \cos(\alpha_0).$$

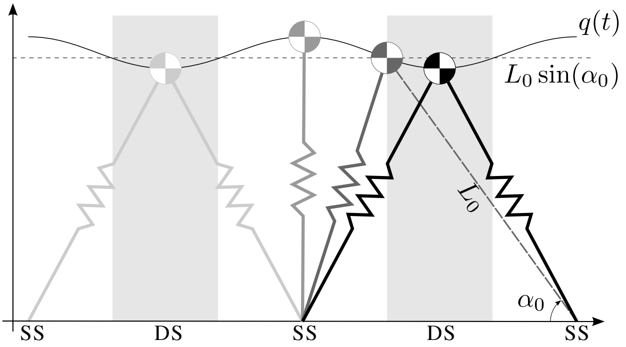

Figure 11.2: Passive gait of the bipedal SLIP model—The model alternates between single support (SS) and double support (DS) phases, depending on the hip height and the model parameters L_0 and α_0. The gray shading will be used throughout this paper to indicate that the walker is in the double support phase.

Conversely, when the system is in the double support phase, the transition to the single support phase occurs when either of the two springs reaches its rest length with non-zero speed, and thus loses contact with the ground, i.e. when

$$\sqrt{(q_1 - c_i)^2 + q_2^2} = L_0, \quad i = 1, 2. \tag{11.2}$$

In nominal conditions, only the trailing leg is allowed to lift off, after which the contact point c_2 is relabeled as c_1 to correspond to the notation used for the single support phase.

In order to derive the dynamic equations, we define the kinetic energy function $K = \frac{1}{2} p^T M^{-1} p$, where

$$M = \operatorname{diag}(m_h, m_h) \tag{11.3}$$

is the mass matrix and $p := M\dot{q}$ are the momentum variables. The potential energy function is defined as

$$V = m_h g_0 q_2 + \tfrac{1}{2} k_0 (L_0 - L_1)^2 + \tfrac{1}{2} k_0 (L_0 - L_2)^2,$$

where $L_i := \sqrt{(q_1 - c_i)^2 + q_2^2}$, and g_0 is the gravitational acceleration. During the single support phase, we set $L_2 \equiv L_0$ to eliminate the influence of this virtually swinging leg.

The dynamic equations in Hamiltonian form are defined through the Hamiltonian energy function $H = K + V$ and given by

$$\frac{\mathrm{d}}{\mathrm{d}t} \begin{bmatrix} q \\ p \end{bmatrix} = \begin{bmatrix} 0 & I \\ -I & 0 \end{bmatrix} \begin{bmatrix} \frac{\partial H}{\partial q} \\ \frac{\partial H}{\partial p} \end{bmatrix}. \tag{11.4}$$

It is noted that solutions of (11.4) are of class C^2. This is due to the fact that the $\frac{\partial V}{\partial q}$ is not differentiable at the moment of phase transition. This is because the

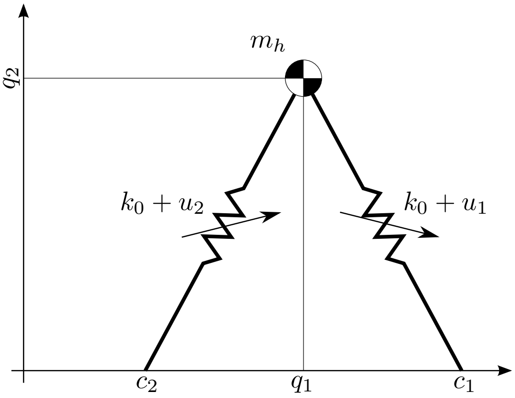

Figure 11.3: The V-SLIP model—In contrast to the bipedal SLIP model, the V-SLIP model has a controllable leg stiffness. This provides two control inputs during the double support phase, but only one control input during the single support phase, rendering the system underactuated.

massless second leg does not have a zero rate of change of length at the moment of touchdown, i.e.

$$\frac{\mathrm{d}}{\mathrm{d}t} L_2 \Big|_{t=t^+_{\text{touchdown}}} \neq 0,$$

where $t^+_{\text{touchdown}}$ indicates that the time-derivative is taken on the right of the discontinuity. It will be shown later that this has consequences for the controller design.

11.3 The Controlled V-SLIP Model

The passive bipedal SLIP model provides no control inputs, and therefore the only way to influence its behavior is by the choice of initial conditions. Therefore, it is proposed to extend the bipedal SLIP model to have massless telescopic springs with *variable* stiffness [69]. This bipedal V-SLIP (for Variable SLIP) model is depicted in Fig. 11.3. The difference with respect to the bipedal SLIP model is that the leg stiffness now has a controllable part, i.e. $k_i = k_0 + u_i, i = 1, 2$. In this Section we give the dynamic equations for this system and present a stabilizing controller.

11.3.1 System Dynamics

The autonomous part of the dynamics of the bipedal V-SLIP model is the same as for the bipedal SLIP model. To include the control inputs, (11.4) is extended, arriving at the dynamics for the V-SLIP model in port-Hamiltonian form:

$$\begin{aligned} \frac{\mathrm{d}}{\mathrm{d}t}\begin{bmatrix} q \\ p \end{bmatrix} &= \begin{bmatrix} 0 & I \\ -I & 0 \end{bmatrix} \begin{bmatrix} \frac{\partial H}{\partial q} \\ \frac{\partial H}{\partial p} \end{bmatrix} + \begin{bmatrix} 0 \\ B \end{bmatrix} u \\ y &= \begin{bmatrix} 0 & B^T \end{bmatrix} \begin{bmatrix} \frac{\partial H}{\partial q} \\ \frac{\partial H}{\partial p} \end{bmatrix}, \end{aligned} \tag{11.5}$$

with $u = (u_1, u_2)$ the controlled leg stiffness, and H is as defined in Section 11.2.1. The input matrix B is given by

$$B = \begin{bmatrix} \frac{\partial \phi_1}{\partial q_1} & \frac{\partial \phi_2}{\partial q_1} \\ \frac{\partial \phi_1}{\partial q_2} & \frac{\partial \phi_2}{\partial q_2} \end{bmatrix},$$

with

$$\phi_1 = -\tfrac{1}{2}(L_0 - L_1)^2 \quad \text{and} \quad \phi_2 = -\tfrac{1}{2}(L_0 - L_2)^2.$$

The output y is dual to u, and it is readily verified that the dual product $\langle u|y \rangle$ has the units of power [14].

As in Section 11.2.1, we set $L_2 \equiv L_0$ during the single support phase to eliminate the influence of the swing leg. It is emphasized that the control inputs $u_i, i = 1, 2$ are restricted, such that the total leg stiffness is physically meaningful, i.e.

$$u_i \in \mathbb{R} \mid 0 < k_0 + u_i < \infty. \tag{11.6}$$

11.3.2 Controller Design

The bipedal SLIP model already shows stable walking gaits, with a relatively large basin of attraction [44]. As shown in our previous work, it is possible to tune the spring stiffness k to further increase the robustness of the gait, while minimally modifying the natural dynamics of the walker [69].

The control strategy uses a natural gait of the bipedal SLIP model as reference, i.e. trajectories $(q^\circ(t), \dot{q}^\circ(t))$ that are a solution of (11.4), where $\dot{q}$ is defined as $\dot{q} = M^{-1}p$. However, the bipedal V-SLIP model is underactuated during the single support phase (since there is only one leg in contact with the ground), and thus it is not possible to track $(q^\circ(t), \dot{q}^\circ(t))$ exactly. To avoid that the walker lags behind the reference during the underactuated phase, we propose to instead define a curve in the configuration space by parameterizing $(q^\circ(t), \dot{q}^\circ(t))$ by the horizontal position q_1, similar to the approach presented in [49]. This is possible[1] as long as $\dot{q}_1 > 0$. Then, the desired reference gait can be equivalently described as $(q_2^*(q_1), \dot{q}_1^*(q_1))$. The control objective is to have the hip trajectory converge to an arbitrary small neighborhood of this reference gait.

---

[1] Exact parameterization is not possible, because $q(t)$ is of class C^2 only, as outlined in Section 11.2.1. Approximating $(q^\circ(t), \dot{q}^\circ(t))$ by finite Fourier series is an alternative that gives satisfactory results, as will be demonstrated.

In formulating the control strategy, we define the state $x = (q, p)$ and rewrite (11.5) in standard form as

$$\dot{x} = f(x) + \sum_i g_i(x) u_i. \tag{11.7}$$

The following control strategy is proposed.

Proposition 11.1 *Given parameterized reference state trajectories* $(q_2^*, \dot{q}_1^*)$*, define the error functions*

$$\begin{aligned} h_1 &= q_2^* - q_2, \\ h_2 &= \dot{q}_1^* - \dot{q}_1. \end{aligned}$$

Then the following control strategy renders solutions of (11.5) *asymptotically converging to* $(q_2^*, \dot{q}_1^*)$*:*

- *during the single support phase,*

  $$u_1 = -\frac{1}{\mathcal{L}_{g_1}\mathcal{L}_f h_1}\left(\mathcal{L}_f^2 h_1 + \kappa_d \mathcal{L}_f h_1 + \kappa_p h_1\right) \tag{11.8}$$

  and $u_2 \equiv 0$*;*

- *during the double support phase, when the leading leg length satisfies* $L_0 - L_e \leq L_1 < L_0$ *(i.e. just after the touchdown event), or when the trailing leg length satisfies* $L_0 - L_e \leq L_2 < L_0$ *(just before the lift-off event), for some small* $L_e > 0$*:*

  $$\begin{bmatrix} u_1 \\ u_2 \end{bmatrix} = -A^\sharp \left(\mathcal{L}_f^2 h_1 + \kappa_d \mathcal{L}_f h_1 + \kappa_p h_1\right), \tag{11.9}$$

  with

  $$A = \begin{bmatrix} \mathcal{L}_{g_1}\mathcal{L}_f h_1 & \mathcal{L}_{g_2}\mathcal{L}_f h_1 \end{bmatrix},$$

  and with $^\sharp$ *denoting the Moore-Penrose*[2] *pseudo inverse;*

- *during the double support phase, when both leg lengths satisfy* $L_i < L_0 - L_e$*,*

  $$\begin{bmatrix} u_1 \\ u_2 \end{bmatrix} = -A^{-1} \begin{bmatrix} \mathcal{L}_f^2 h_1 + \kappa_d \mathcal{L}_f h_1 + \kappa_p h_1 \\ \mathcal{L}_f h_2 + \kappa_v h_2 \end{bmatrix}, \tag{11.10}$$

  with

  $$A = \begin{bmatrix} \mathcal{L}_{g_1}\mathcal{L}_f h_1 & \mathcal{L}_{g_2}\mathcal{L}_f h_1 \\ \mathcal{L}_{g_1} h_2 & \mathcal{L}_{g_2} h_2 \end{bmatrix}.$$

---

[2] Since we are addressing a numerical issue, we are not concerned about deriving a proper invariant metric for defining the pseudo-inverse. Instead, we use the Euclidian metric.

In particular, for suitably chosen constant $\kappa_p, \kappa_d, \kappa_v > 0$*, the control strategy* (11.8)*,* (11.9)*,* (11.10) *realizes:*

$$\lim_{t\to\infty} q_2^*(q_1(t)) - q_2(t) = 0,$$

and, for some arbitrary small $\varepsilon > 0$*,*

$$\lim_{t\to\infty} |\dot{q}_1^*(q_1(t)) - \dot{q}_1(t)| < \varepsilon.$$

Remark 11.1 The control input (11.9) is introduced, because the system (11.5) is no longer controllable when one of the legs reaches its rest length L_0. As such, the transition domain defined by L_e is necessary to comply with (11.6). ◁

Remark 11.2 As observed in Section 11.2.1, the state trajectories $q(t)$ are of class C^2 only, and therefore it is not possible to make the leg stiffness a state of the system, because higher order Lie-derivatives do not exist. ◁

Proof: It is straightforward to show that, during the single support phase, $\mathcal{L}_{g_1}\mathcal{L}_f h_1$ in (11.8) is bounded away from zero if $0 < L_1 < L_0$. Similarly, during the double support phase, the matrix A in (11.10) is invertible if $0 < L_i < L_0, i = 1, 2$ and in addition $c_1 \neq c_2$. These conditions are met through the definition of the phase transitions (11.1) and (11.2).

During the double support phase, (11.10) renders the system strongly input-output decoupled, i.e. h_i is invariant under u_j for $i \neq j$ [42]. Therefore, and by (11.8), (11.9), during both the single and double support phases the error dynamics $h_1(t)$ are described by

$$\ddot{h}_1 + \kappa_d \dot{h}_1 + \kappa_p = 0.$$

If κ_p, κ_d are chosen such that the zeros are in the open left half-plane, then the dynamics of h_1 are asymptotically stable during each phase. The error function h_1 depends on the configuration q only, and $q(t)$ is continuous and differentiable across the phase transitions. Therefore,

$$\lim_{t\to\infty} q_2^*(q_1(t)) - q_2(t) = 0$$

will be achieved.

The dynamics of the error function h_2 are, during the double support phase, described by

$$\dot{h}_2 + \kappa_v h_2 = 0,$$

which has as analytic solution

$$h_2(t) = e^{-\kappa_v (t - t_{\mathrm{ds}})} h_2(t_{\mathrm{ds}}), \quad t \geq t_{\mathrm{ds}},$$

where t_{ds} is the time instant of the last touchdown event. For any $\kappa_v > 0$, $h_2(t)$ is asymptotically stable during the double support phase.

Table 11.1: Controlled V-SLIP model parameter values.

Parameter	Value	Unit	Description
m_h	15.0	kg	Hip mass
L_0	1.0	m	Spring rest length
L_e	0.01	m	Phase transition margin
α_0	62.5	°	Angle of attack
k_0	2000	N/m	Nominal leg stiffness
$k_{\min}$	0	N/m	Lower bound on leg stiffness
$k_{\max}$	10000	N/m	Upper bound on leg stiffness
κ_p	350		Control parameter
κ_d	40		Control parameter
κ_v	15		Control parameter

However, during the single support phase, the dynamics of $h_2(t)$ are uncontrolled. During this phase, the control action of u_1 will result in a change of kinetic energy with respect to the constant energy level of the SLIP reference gait. Since u_1 is bounded, as defined in (11.6), the total increase in kinetic energy is also bounded. Let ΔE_{ss} denote the increase of energy during the single support phase due to u_1. There exists a constant C_1 such that

$$|\Delta E| < C_1,$$

which implies, since $h_2(t)$ is a function of the momentum variable p_2, that

$$|h_2(t_{\text{ds}})| < C_2 < C_1.$$

This in turn implies that there exists $\kappa_v < \infty$ that brings $h_2(t)$ in a neighborhood ε of zero within the duration of the double support phase. □

With the parameters as listed in Table 11.1, a numeric simulation has been carried out using the PyDSTool software package [10]. The reference $(q_2^*, \dot{q}_1^*)$ has been obtained by searching for a limit cycle of the uncontrolled SLIP model with the same parameters. As shown in Fig. 11.4, the controller indeed achieves the converges as claimed in Proposition 11.1. The error h_2 is never exactly zero, because the solutions to (11.4) are not analytical. Therefore the parameterized reference is not an exact representation of the natural dynamics, yielding the mismatch in h_2 during the single support phase.

11.4 The Controlled V-SLIP Model with Swing Leg Dynamics

While the bipedal (V-)SLIP models do accurately reproduce hip trajectories observed in human walking, and thus can give insights in human walking performance,

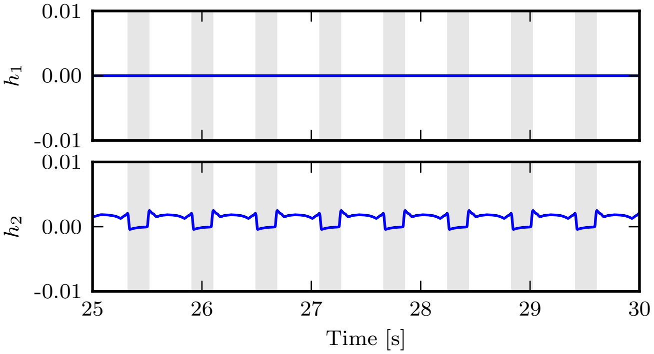

Figure 11.4: Steady-state error functions for the controlled V-SLIP model—It can be seen that for the control parameters listed in Table 11.1 the error functions converge like claimed in Proposition 11.1.

the models are conceptual. In particular, all mass is assumed to be concentrated in a single point mass at the hip, and the legs are assumed to be massless springs—assumptions that cannot be considered valid for a robotic system.

In this Section we extend the V-SLIP model to incorporate swing leg dynamics. This is done by adding a foot mass, as shown in Fig. 11.5 [70]. During the swing phase, the leg is assumed to have a fixed length L_0, while during the stance phase it is again assumed to be a massless spring connecting the foot and the hip masses. In this Section we derive the dynamic equations that govern the system behavior, and extend the controller from Section 11.3.2 to handle the swing leg dynamics.

11.4.1 System Dynamics

In deriving the dynamics of the V-SLIP model with feet, we assume that:

- no slip or bouncing occurs in the foot contact points;
- the springs are unilateral, meaning that we only allow them to be compressed;
- during the single support phase, the swing leg is constraint to have length L_0.

Under these assumptions, during the double support phase, we can use the double support phase model used in Section 11.3.1, and the model behavior is described accordingly by (11.5).

During the single support phase, the model can be simplified as shown in Fig. 11.6. The configuration of the system can be described by (q_1, q_2, q_3), where $q_3 \in [0, \pi)$ is the orientation of the swing leg. The total mass of the swing leg is $m = m_h + m_f$. Since the swing leg is assumed to be a rigid link of length L_0, its

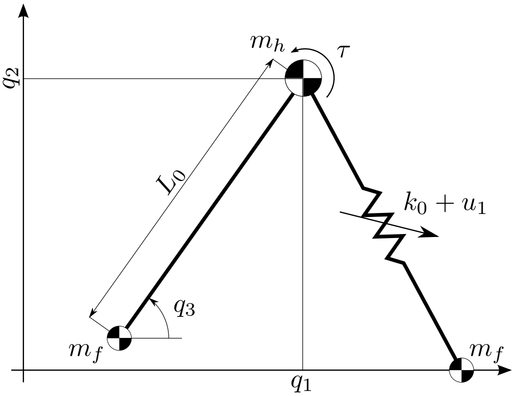

Figure 11.5: The V-SLIP model with feet—By adding feet masses m_f to the V-SLIP model, swing leg dynamics are introduced. The swing leg is assumed to be constraint at a length L_0 during swing, and the stance foot is assumed to be fixed to the ground, i.e. no slip or bouncing in the contact point.

center of mass is at a distance

$$d_{\text{com}} = \frac{m_f L_0}{m_h + m_f}$$

from the hip joint (as indicated in Fig. 11.6). The moment of inertia of the leg around its center of mass is given by

$$J_{\text{com}} = m_h d_{\text{com}}^2 + m_f (L_0 - d_{\text{com}})^2.$$

In order to derive the dynamic equations of the system for the single support phase, we let $(v_1, v_2, v_3) =: v$ denote the horizontal, vertical and rotational velocity of the (center of mass of the) swing leg. These velocities are related to the rate of change of the configuration variables $\dot{q}$ by the Jacobian matrix $S(q)$, defined as:

$$S(q) = \begin{bmatrix} 1 & 0 & d_{\text{com}} \sin(q_3) \\ 0 & 1 & -d_{\text{com}} \cos(q_3) \\ 0 & 0 & 1 \end{bmatrix}, \tag{11.11}$$

such that $v = S(q)\dot{q}$. This allows to have the configuration variables q coincide with those used in the V-SLIP model of Section 11.3. In particular, by defining $p := Mv$, with

$$M = \operatorname{diag}(m_h + m_f, m_h + m_f, J_{\text{com}}) \tag{11.12}$$

the mass matrix of the rigid body representing swing leg, the dynamics during the single support phase can be derived in terms of (q, p) as follows.

The kinetic energy is given by $K = \frac{1}{2} p^T M^{-1} p$, and we derive the potential energy function V as

$$V = (m_h + m_f) g_0 (q_2 - d_{\text{com}} \sin(q_3)) + \tfrac{1}{2} k_0 (L_0 - L_1)^2.$$

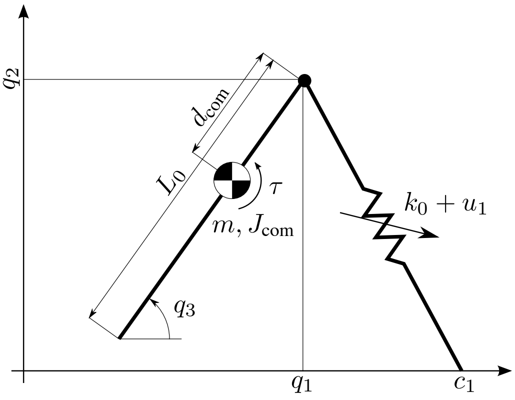

Figure 11.6: Model simplification—Under the assumptions of a rigid swing leg and no slip or bouncing in the foot contact point, the model depicted in Fig. 11.5 can be simplified during the single support phase. During the double support phase, the model is reduced to the V-SLIP model, as shown in Fig. 11.3.

Then, the Hamiltonian energy function is given by $H = K + V$, and we derive the dynamic equations in port-Hamiltonian form by using the Boltzmann-Hamel equations [15], yielding:

$$\begin{aligned} \frac{\mathrm{d}}{\mathrm{d}t}\begin{bmatrix} q \\ p \end{bmatrix} &= J \begin{bmatrix} \frac{\partial H}{\partial q} \\ \frac{\partial H}{\partial p} \end{bmatrix} + \begin{bmatrix} 0 \\ B \end{bmatrix} u \\ y &= \begin{bmatrix} 0 & B^T \end{bmatrix} \begin{bmatrix} \frac{\partial H}{\partial q} \\ \frac{\partial H}{\partial p} \end{bmatrix}, \end{aligned} \tag{11.13}$$

where the skew-symmetric matrix J is given by

$$J = \begin{bmatrix} 0 & S^{-1} \\ -S^{-T} & S^{-T}\left(\frac{\partial^T (S^T p)}{\partial q} - \frac{\partial (S^T p)}{\partial q}\right) S^{-1} \end{bmatrix}.$$

Again, the output y is dual to the input u, so that $\langle u|y\rangle$ defines a power flow. The control input $u = (u_1, \tau)$, i.e. the controllable part of the stance leg stiffness, and the torque applied to the swing leg. The input matrix B is given by

$$B = S^{-T} \begin{bmatrix} \frac{\partial \phi_1}{\partial q_1} & 0 \\ \frac{\partial \phi_1}{\partial q_2} & 0 \\ 0 & 1 \end{bmatrix},$$

with

$$\phi_1 = -\tfrac{1}{2}(L_0 - L_1)^2.$$

The mapping by S^{-T} is necessary because the inputs are not collocated with v, but with $\dot{q}$, as can be seen in Fig. 11.6.

11.4.2 Phase Transitions

Unlike the V-SLIP model, where in both the double and single support phases the same configuration variables are used, this model uses two sets of configuration variables: in the double support phase only the position of the hip with respect to the foot contact points is relevant, while in the single support phase also the swing leg orientation is required. Therefore, phase transition mappings need to be defined as follows.

Transition Conditions

Similar to the (V-)SLIP models, the touchdown event occurs when the foot of the swing leg has passed in front of the hip,[3] and in addition, recalling that the swing leg is constraint to have length L_0 during the swing phase,

$$q_2 = L_0 \sin(q_3).$$

At the time instance that both of these conditions are met, the new foot contact point c_2 is computed as

$$c_2 = q_1 - L_0 \cos(q_3).$$

The lift-off event occurs when the trailing leg reaches its rest length L_0 with non-zero speed, since we do not allow the springs to pull.[4]

Momentum Variable Mapping

To complete the phase transitions, the momentum variables of the double support phase need to be mapped to the momentum variables for the single support phase and vice versa. This mapping also needs to ensure that the constraints on the foot contact points are maintained. In particular, upon touchdown, the foot of the former swing leg needs to be instantaneously constraint to fulfill the no-slip condition. This can be realized by applying a momentum reset at the instant of touchdown [16]. It was shown in our previous work that, despite the energy loss associated with the impact, energy-efficient locomotion can be realized [70]. However, in this work, we will focus on the added benefit of the compliant legs, and thus assume a compliant impact. This implies that, upon impact, the foot mass m_f will instantaneously dissipate its kinetic energy, while the hip mass m_h remains unaffected by the impact due to the compliant leg.

To map the momentum variables between the phases, we need to account for the disappearing and reappearing of the foot mass. For this purpose, we define

---

[3] Essentially the swing leg is allowed to swing through the floor. This will be addressed in the next model iteration in Section 11.5.

[4] To be accurate, the transition occurs when the foot starts to accelerate away from the floor. However, this is practically equivalent to assuming that the transition occurs at the moment the spring length becomes equal to its rest length and assuming that the leg instantly becomes rigid at the same moment.

new coordinates

$$z_1 = (q_1, q_2, q_3) \quad \text{and} \quad z_2 = (q_1, q_2, c_i),$$

where c_i denotes the contact point that is subject to change due to the transition. During both the touchdown and the lift-off event, the leg length is assumed to be L_0, so that we obtain

$$z_2(z_1) = \begin{bmatrix} q_1 \\ q_2 \\ q_1 - L_0 \cos(q_3) \end{bmatrix}.$$

We define the Jacobian matrix $Z := \partial z_2 / \partial z_1$ accordingly.

For the transition from single support to double support, using the subscripts "old" and "new" for post- and pre-transition values, we have:

$$\dot{z}_{2,\text{new}} = Z \dot{z}_{1,\text{old}},$$

where $\dot{z}_{1,\text{old}}$ is defined by the momentum variables p_{old} just before the phase transition:

$$\dot{z}_{1,\text{old}} = S^{-1}(q) M_{\text{ss}}^{-1} p_{\text{old}},$$

with $S(q)$ defined in (11.11) and M_{ss} the mass matrix defined in (11.12). Note that the expression for $\dot{c}_2$ is irrelevant in this phase transition, since we assume that the foot is instantly constraint. The post-transition momentum variables for the double support phase p_{new} are then given by

$$p_{\text{new}} = M_{\text{ds}} \underbrace{\begin{bmatrix} \dot{q}_1 \\ \dot{q}_2 \end{bmatrix}}_{\in \dot{z}_{2,\text{new}}},$$

with M_{ds} the mass matrix defined in (11.3).

Similarly, for the transition from double support to single support, we have

$$\dot{z}_{1,\text{new}} = Z^{-1} \dot{z}_{2,\text{old}},$$

where $\dot{z}_{2,\text{old}}$ is defined through the momentum variables p_{old} just before the phase transition:

$$\dot{z}_{2,\text{old}} = M_{\text{ds}}^{-1} p_{\text{old}},$$

with M_{ds} the mass matrix defined in (11.3), and setting $\dot{c}_1 = 0$, since the foot is stationary at the moment of lift-off. The post-transition momentum variables p_{new} for the single support phase are then calculated as

$$p_{\text{new}} = M_{\text{ss}} S(q) \dot{z}_{1,\text{new}},$$

with $S(q)$ defined in (11.11).

11.4.3 Controller Design

During the double support phase, the model is equivalent to the V-SLIP model, and therefore, during this phase, the control strategy proposed in Proposition 11.1 can be used. For the single support phase, the control strategy has to be extended to regulate the swing leg trajectory $q_3(t)$. For this purpose, we define a reference trajectory $q_3^*(t)$ as a polynomial:

$$q_3^*(t) = \sum_{i=0}^{5} a_i (t - t_{\mathrm{lo}})^i, \quad t_{\mathrm{lo}} \leq t < t_{\mathrm{lo}} + T_{\mathrm{swing}},$$

where T_{swing} is the desired swing time, e.g. obtained from the nominal single support phase time of the SLIP model reference gait, and t_{lo} is the time instant of the last lift-off event. The coefficients a_i are such that $q_3^*(t)$ is a minimum-jerk trajectory with boundary conditions[5]

$$\begin{pmatrix} q_3^*(t_{\mathrm{lo}}) \\ \dot{q}_3^*(t_{\mathrm{lo}}) \\ \ddot{q}_3^*(t_{\mathrm{lo}}) \end{pmatrix} = \begin{pmatrix} q_3(t_{\mathrm{lo}}) \\ 0 \\ 0 \end{pmatrix}$$

and

$$\begin{pmatrix} q_3^*(t_{\mathrm{lo}} + T_{\mathrm{swing}}) \\ \dot{q}_3^*(t_{\mathrm{lo}} + T_{\mathrm{swing}}) \\ \ddot{q}_3^*(t_{\mathrm{lo}} + T_{\mathrm{swing}}) \end{pmatrix} = \begin{pmatrix} \pi - \alpha_0 \\ 0 \\ 0 \end{pmatrix}.$$

In formulating the control strategy, we will define for both the double support and single support phases a state vector of the form $x = (q, p)$ and write the respective differential equations (11.5) and (11.13) in the standard form (11.7). The following control strategy is proposed, extending the V-SLIP control strategy formulated in Proposition 11.1.

Proposition 11.2 *Given reference state trajectories* $(q_2^*, \dot{q}_1^*, q_3^*)$, *define the error functions*

$$\begin{aligned} h_1 &= q_2^* - q_2, \\ h_2 &= \dot{q}_1^* - \dot{q}_1, \\ h_3 &= q_3^* - q_3. \end{aligned}$$

During the double support phase, the corresponding control strategy formulated in Proposition 11.1 renders solutions of (11.5) *asymptotically converging to* $(q_2^*, \dot{q}_1^*)$.

During the single support phase, the following control strategy renders solutions of (11.13) *asymptotically converging to* (q_2^*, q_3^*):

$$\begin{bmatrix} u_1 \\ \tau \end{bmatrix} = -A^{-1} \begin{bmatrix} \mathcal{L}_f^2 h_1 + \kappa_d \mathcal{L}_f h_1 + \kappa_p h_1 \\ \mathcal{L}_f^2 h_3 + \kappa_w \mathcal{L}_f h_3 + \kappa_a h_3 \end{bmatrix}, \tag{11.14}$$

---

[5] The velocity $\dot{q}_3(t_{\mathrm{lo}})$ and the acceleration $\ddot{q}_3(t_{\mathrm{lo}})$ are not matched by the reference trajectory $q_3^*(t)$, because these quantities are in practice very difficult to measure accurately.

with

$$A = \begin{bmatrix} \mathcal{L}_{g_1}\mathcal{L}_f h_1 & \mathcal{L}_{g_2}\mathcal{L}_f h_1 \\ \mathcal{L}_{g_1}\mathcal{L}_f h_3 & \mathcal{L}_{g_2}\mathcal{L}_f h_3 \end{bmatrix}.$$

In particular, for suitable chosen constants $\kappa_p, \kappa_d, \kappa_v, \kappa_a, \kappa_w > 0$*, the control strategy* (11.9)*,* (11.10)*,* (11.14) *realizes, for some small* $\varepsilon_1 > 0$*,*

$$\lim_{t\to\infty} |q_2^*(t) - q_2(t)| < \varepsilon_1,$$

and for some small $\varepsilon_2 > 0$*,*

$$\lim_{t\to\infty} |\dot{q}_1^*(t) - \dot{q}_1(t)| < \varepsilon_2,$$

and, during $t_{lo} \leq t < t_{lo} + T_{swing}$*, for some suitable* $\delta > 0$*,*

$$|q_3^*(t_{lo} + T_{swing}) - q_3(t_{lo} + T_{swing})| < \delta.$$

Proof: The control strategy is such that the system is strongly input-output decoupled. Therefore, the dynamics of $h_1(t)$ are given by

$$\ddot{h}_1 + \kappa_d \dot{h}_1 + \kappa_p h_1 = e_1,$$

where $e_1(t)$ is a disturbance due to the phase transitions. As a result, $q_2(t)$ is continuous, but not differentiable. However, $e_1(t)$ is bounded and impulsive, and therefore there exists constants $\kappa_p, \kappa_d > 0$ such that $h_2(t)$ converges to a neighborhood ε_1 of zero.

Similarly, the dynamics dynamics of $h_2(t)$ are given by

$$\dot{h}_2 + \kappa_v h_2 = e_2,$$

where $e_2(t)$ is also a disturbance due to the phase transitions. As a result of these disturbances, $\dot{q}_1(t)$ is not continuous. However, since $e_2(t)$ is bounded and impulsive, there exist a $\kappa_v > 0$ such that $h_2(t)$ converges to a neighborhood ε_2 of zero.

During the single support phase, the dynamics $h_3(t)$ are given by

$$\ddot{h}_3 + \kappa_w \dot{h}_3 + \kappa_a h_3 = 0.$$

For suitably chosen constant $\kappa_a, \kappa_w > 0$, such that the zero are in the open left half-plane, the error function $h_3(t)$ converges to a neighborhood δ of zero in finite time. □

The proposed control strategy has been validated through numeric simulations. The same parameters were used as for the V-SLIP model as listed in Table 11.1, and $m_f = 2.5$ kg. Furthermore, $\kappa_a = 1000$ and $\kappa_w = 40$. It can be observed that the error functions converge as claimed in Proposition 11.2. In particular, the influence of the swing leg can be clearly observed when the plots are compared to Fig. 11.4. Specifically, we can see the influence of the swing leg motion in the error

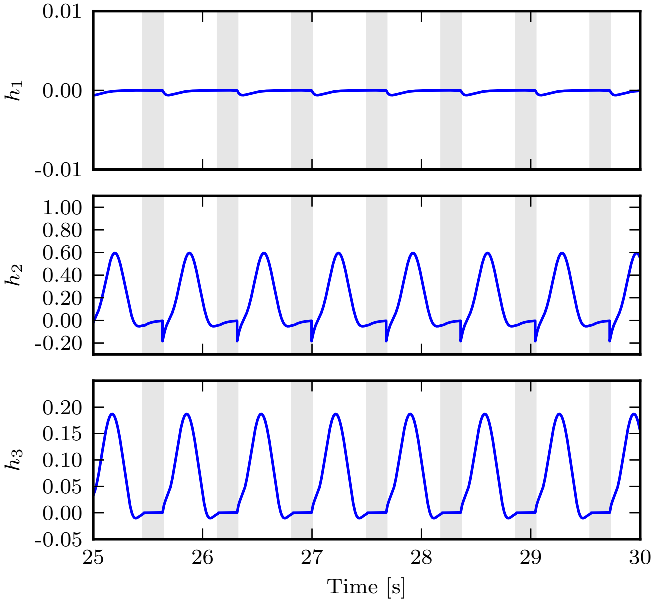

Figure 11.7: Steady-state error functions for the controlled V-SLIP model with swing leg—It can be seen that the error functions converge like claimed in Proposition 11.2. Note that $h_3 \equiv 0$ during the double support phase.

function h_1 at the onset of the single support phases (the unshaded areas of the plot). The error function h_2 also shows a significant increase in amplitude during the swing. We can also observe in h_2 the lift-off of the swing leg in the form of discontinuities at the moment of transition from the double support phase (shaded areas) to the single support phase (unshaded areas). The error function h_3 shows that the swing leg motion is controlled as claimed by the proposed control law. Note that the degree of freedom q_3 is not defined during the double support phase, and therefore $h_3 \equiv 0$ during this phase.

11.5 The Controlled V-SLIP model with Retracting Swing Leg Dynamics

In this Section, we further refine the model presented in Section 11.4 by adding a knee, as shown in Fig. 11.8. This allows the swing leg to be retracted, so that it can be swung forward without scuffing the ground. We derive in this Section the dynamic equations for this model, and further extend the controller.

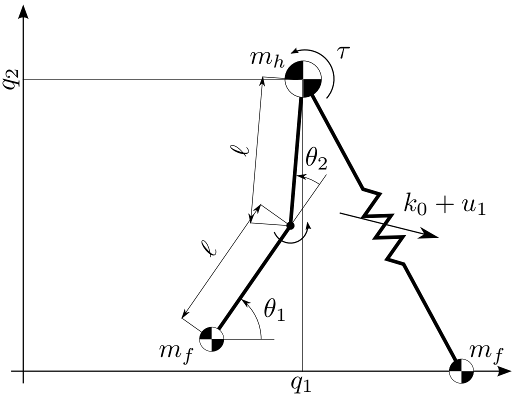

Figure 11.8: The V-SLIP model with feet and knees—By adding an actuated knee joint to the model of Section 11.4, the leg can be retracted during the single support phase. This allows the leg to swing forward without scuffing the ground. It is assumed that no slip or bouncing occurs in the foot contact point of the stance leg.

11.5.1 System Dynamics

Similar to the model presented in Section 11.4, we will assume that:

- no slip or bouncing occurs in the foot contact points;
- the spring are unilateral.

These assumptions allow to again use the double support phase model used in Section 11.3.1.

To avoid notational clutter due to goniometric relations, the simplified model depicted in Fig. 11.9 is used. The simplification is possible, because the introduction of the knee joint introduces only a kinematic relation between the hip mass and the foot mass, since these are located at the extremities of the swing leg.

In deriving the dynamic equations for the single support phase of this model, we define new coordinates as

$$z_1 = (q_1, q_2, q_3, q_4) \quad \text{and} \quad z_2 = (q_1, q_2, s_1, s_2) \tag{11.15}$$

where

$$\begin{aligned} s_1 &= q_1 - q_4 \cos(q_3), \\ s_2 &= q_2 - q_4 \sin(q_3), \end{aligned} \tag{11.16}$$

i.e. the position of the foot of the swing leg. We furthermore define the tangent map $Z = \partial z_2 / \partial z_1$. Using this relation and noting that $z_1 = q$ and thus that $\dot{z}_2 = Z\dot{q}$, we can derive the mass matrix $M(q)$ from the energy equality

$$\tfrac{1}{2}\dot{q}^T M(q)\dot{q} = \tfrac{1}{2}\dot{z}_2^T M_0 \dot{z}_2 = \tfrac{1}{2}\dot{q}^T Z^T M_0 Z \dot{q}, \tag{11.17}$$

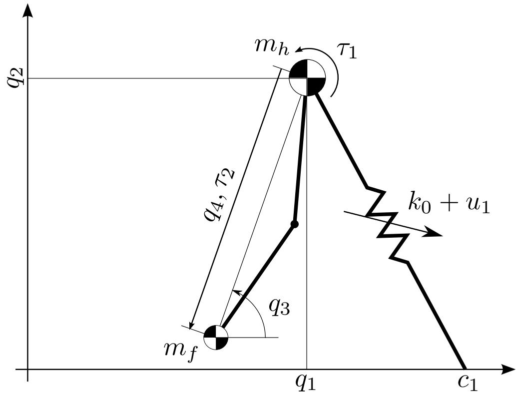

Figure 11.9: Model simplification—The configuration of the swing leg can be equivalently described by a linear degree of freedom q_4, corresponding to the distance between the hip and the foot, and the orientation q_3, analogous to the model of Fig. 11.5. During the double support phase, the model is reduced to the V-SLIP model, as shown in Fig. 11.3.

with $M_0 = \text{diag}(m_h, m_h, m_f, m_f)$.

By defining the momentum variables $p := M(q)\dot{q}$, the kinetic energy $K = \frac{1}{2}p^T M^{-1}(q)p$, and the potential energy function V is found to be:

$$V = m_h g_0 q_2 + m_f g_0 (q_2 - q_4 \sin(q_3)) + \tfrac{1}{2}k_0 (L_0 - L_1)^2.$$

Then, the Hamiltonian energy function $H = K + V$ and the dynamic equations in port-Hamiltonian form are given by

$$\begin{aligned} \frac{\mathrm{d}}{\mathrm{d}t}\begin{bmatrix} q \\ p \end{bmatrix} &= \begin{bmatrix} 0 & I \\ -I & 0 \end{bmatrix} \begin{bmatrix} \frac{\partial H}{\partial q} \\ \frac{\partial H}{\partial p} \end{bmatrix} + \begin{bmatrix} 0 \\ B \end{bmatrix} u \\ y &= \begin{bmatrix} 0 & B^T \end{bmatrix} \begin{bmatrix} \frac{\partial H}{\partial q} \\ \frac{\partial H}{\partial p} \end{bmatrix}, \end{aligned} \tag{11.18}$$

where $u = (u_1, \tau_1, \tau_2)$, i.e. the controllable parts of the stance leg stiffness, and the torques collocated with q_3 and q_4. The input matrix B is given by

$$B = \begin{bmatrix} \frac{\partial \phi_1}{\partial q_1} & 0 & 0 \\ \frac{\partial \phi_1}{\partial q_2} & 0 & 0 \\ 0 & 1 & 0 \\ 0 & 0 & 1 \end{bmatrix},$$

with

$$\phi_1 = -\tfrac{1}{2}(L_0 - L_1)^2.$$

11.5.2 Phase Transitions

Just as in the model described in Section 11.4, also in this model we need to consider the different sets of configuration variables in the single and double support phases. Therefore, in the following the phase transition mappings are defined.

Transition Conditions

The touchdown event occurs when the swing leg foot hits the ground, i.e. when, using (11.16),

$$q_2 = q_4 \sin(q_3).$$

At this time instant, the new foot contact point c_2 (see Fig. 11.3) is computed as

$$c_2 = q_1 - q_4 \cos(q_3).$$

The lift-off event is defined the same as in Section 11.4.2, since both models are reduced to the V-SLIP model during the double support phase.

Momentum variable mapping

Similarly to the approach taken in Section 11.4.2, we start from the new set of coordinates defined in (11.15) and the corresponding Jacobian matrix Z. Thus, for the transition from single support to double support:

$$\dot{z}_{2,\text{new}} = Z\dot{z}_{1,\text{old}},$$

where $\dot{z}_{1,\text{old}}$ is defined by the pre-transition momentum variables p_{old} through

$$\dot{z}_{1,\text{old}} = M_{\text{ss}}^{-1} p_{\text{old}}.$$

Here, M_{ss} is the mass matrix defined in (11.17). As in Section 11.4.1, the post-transition momentum variables for the double support phase p_{new} are given by

$$p_{\text{new}} = M_{\text{ds}} \underbrace{\begin{bmatrix} \dot{q}_1 \\ \dot{q}_2 \end{bmatrix}}_{\in \dot{z}_{2,\text{new}}},$$

with M_{ds} the mass matrix defined in (11.3).

For the transition from double support to single support, we again have

$$\dot{z}_{1,\text{new}} = Z^{-1}\dot{z}_{2,\text{old}},$$

where $\dot{z}_{2,\text{old}}$ is defined through the momentum variables p_{old} just before the phase transition:

$$\dot{z}_{2,\text{old}} = M_{\text{ds}}^{-1} p_{\text{old}},$$

with M_{ds} the mass matrix defined in (11.3), and setting $\dot{s}_1 = \dot{s}_2 = 0$, since the foot is stationary at the moment of lift-off. The post-transition momentum variables p_{new} for the single support phase are then calculated as

$$p_{\text{new}} = M_{\text{ss}}\dot{z}_{1,\text{new}}.$$

11.5.3 Controller Design

During the double support phase, the control strategy proposed in Proposition 11.1 can again be used because of the model correspondence during this phase. For the single support phase, the control strategy has to be extended with respect to the control strategy presented in Proposition 11.2. In particular, in addition to the control of the swing leg orientation, the swing leg length has to be regulated as well. For this purpose, we define a reference trajectory $q_4^*(t)$ of the form

$$q_4^*(t) = b_0 + b_1 t + b_2 t^2, \quad t_{\mathrm{lo}} \le t \le t_{\mathrm{lo}} + T_{\mathrm{swing}}.$$

The coefficients b_i are such that the trajectory $q_4^*(t)$ satisfies the following conditions:

$$\begin{pmatrix} q_4^*(t_{\mathrm{lo}}) \\ q_4^*(t_{\mathrm{lo}} + \frac{1}{2}T_{\mathrm{swing}}) \\ q_4^*(t_{\mathrm{lo}} + T_{\mathrm{swing}}) \end{pmatrix} = \begin{pmatrix} q_4(t_{\mathrm{lo}}) \\ L_0 - \Delta \\ L_0 \end{pmatrix},$$

with $\Delta > 0$ the amount of retraction of the swing leg. This trajectory ensures that at the moment of lift-off the swing leg is immediately accelerating away from the floor, reaching the maximum retraction during the predicted mid-stance. At touchdown, the swing leg will have length L_0, corresponding to the (V-)SLIP model.

Defining the state vector of the form $x = (q, p)$ and writing (11.5) and (11.18) in the standard form (11.7), the following control strategy is proposed, extending the strategy formulated in Proposition 11.2.

Proposition 11.3 *Given reference state trajectories* $(q_2^*, \dot{q}_1^*, q_3^*, q_4^*)$*, define the error functions*

$$\begin{aligned} h_1 &= q_2^* - q_2, \\ h_2 &= \dot{q}_1^* - \dot{q}_1, \\ h_3 &= q_3^* - q_3, \\ h_4 &= q_4^* - q_4. \end{aligned}$$

During the double support phase, the corresponding control strategy formulated in Proposition 11.1 renders solutions of (11.5) *asymptotically converging to* $(q_2^*, \dot{q}_1^*)$.

During the single support phase, the following control strategy renders solutions of (11.18) *asymptotically converging to* (q_2^*, q_3^*, q_4^*)*:*

$$\begin{bmatrix} u_1 \\ \tau \end{bmatrix} = -A^{-1} \begin{bmatrix} \mathcal{L}_f^2 h_1 + \kappa_d \mathcal{L}_f h_1 + \kappa_p h_1 \\ \mathcal{L}_f^2 h_3 + \kappa_w \mathcal{L}_f h_3 + \kappa_a h_3 \\ \mathcal{L}_f^2 h_4 + \kappa_n \mathcal{L}_f h_4 + \kappa_\ell h_4 \end{bmatrix}, \tag{11.19}$$

with

$$A = \begin{bmatrix} \mathcal{L}_{g_1}\mathcal{L}_f h_1 & \mathcal{L}_{g_2}\mathcal{L}_f h_1 & \mathcal{L}_{g_3}\mathcal{L}_f h_1 \\ \mathcal{L}_{g_1}\mathcal{L}_f h_3 & \mathcal{L}_{g_2}\mathcal{L}_f h_3 & \mathcal{L}_{g_3}\mathcal{L}_f h_3 \\ \mathcal{L}_{g_1}\mathcal{L}_f h_4 & \mathcal{L}_{g_2}\mathcal{L}_f h_4 & \mathcal{L}_{g_3}\mathcal{L}_f h_4 \end{bmatrix}.$$

In particular, for suitable chosen constants $\kappa_p, \kappa_d, \kappa_v, \kappa_a, \kappa_w, \kappa_\ell, \kappa_n > 0$, *the control strategy* (11.9), (11.10), (11.19) *realizes for some small* $\varepsilon_1 > 0$*:*

$$\lim_{t\to\infty} |q_2^*(t) - q_2(t)| < \varepsilon_1,$$

and for some small $\varepsilon_2 > 0$,

$$\lim_{t\to\infty} |\dot{q}_1^*(t) - \dot{q}_1(t)| < \varepsilon_2,$$

and, during $t_{lo} \leq t < t_{lo} + T_{swing}$, *for some suitable* $\delta_1, \delta_2 > 0$,

$$\begin{aligned} |q_3^*(t_{lo} + T_{swing}) - q_3(t_{lo} + T_{swing})| &< \delta_1 \\ |q_4^*(t_{lo} + T_{swing}) - q_4(t_{lo} + T_{swing})| &< \delta_2 \end{aligned}$$

The proof is analogous to the proof given in Section 11.4.3 and is omitted for brevity. The control strategy is validated through numeric simulations, with the same model parameters as used in Section 11.4.3, and in addition $\kappa_\ell = 1000$ and $\kappa_n = 40$, with a leg retraction $\Delta = 7.5$ cm. The resulting error function plots are shown in Fig. 11.10, and it can be seen that they converge as claimed in Proposition 11.3. The error functions show now significantly bigger influences of the swing leg dynamics when compared to Fig. 11.7.

11.6 Comparison by Numerical Simulation

Starting from the bipedal SLIP model, three iterations of model refinement have been presented in Section 11.3, Section 11.4, and Section 11.5. Also, in the first iteration, a robust controller for leg stiffness has been presented in Section 11.3.2, which has been extended in subsequent iterations. In this section, a comparison of the performance of these controllers is presented.

11.6.1 Comparison of Gait Control

Fig. 11.11 shows the horizontal hip trajectory $q_1(t)$, and a detail of the corresponding vertical hip trajectory $q_2(t)$. The most notable difference between the three models is their average forward velocity, which is 1.18 m/s for the V-SLIP model, but only 1.01 m/s and 0.64 m/s for the models including the swing leg dynamics and the knee. Looking at the hip trajectories, it can be seen that this is due to the inclusion of the swing leg dynamics, which introduces a lag in forward motion with respect to the V-SLIP dynamics.

The leg stiffness trajectories $k_i = k_0 + u_i$ are shown in Fig. 11.12. Since the reference trajectory is the natural gait of the bipedal SLIP model, it is not surprising that the V-SLIP model requires very little control action to track the reference. The small amount that is required is due to the small mismatch between the parameterized reference trajectory and the true dynamics, as pointed out already in

Section 11.3.2. The introduction of the swing leg dynamics introduces a significant disturbance to the V-SLIP dynamics, exemplified by the larger magnitude of the control inputs. It is interesting to note that the V-SLIP model with swing leg, as introduced in Section 11.4, requires an impulse-like control input during the single support phase to counter the acceleration and deceleration of the swing leg. In contrast, including the leg retraction (Section 11.5) results in a smaller moment of inertia, resulting in a smoother control. However, it is noted that the swing leg retraction does result in larger deceleration of the hip, which manifests itself in larger control inputs during the double support phase (bottom plot), actually reaching the lower bound of zero leg stiffness $k_2 = k_0 + u_2$ for short periods of time.

11.6.2 Energy Balance

We claim that the proposed control strategies are energy efficient. To investigate this claim, the energy balance of the model is instrumental. First, it is noted that the natural gait of the bipedal SLIP model is associated to a constant energy level [21, 44]. Since the V-SLIP model presented in Section 11.3 matches the bipedal SLIP model, its energy balance is the same if the reference trajectory for the V-SLIP controller exactly matches the solutions of (11.4). However, as already noted before, the solutions of (11.4) are not analytical, and therefore a small mismatch between the natural dynamics of the V-SLIP model and the reference is inevitable, resulting in small control action even in nominal conditions, as shown in Fig. 11.12.

The energy balance for the model including the swing leg (Section 11.4) is presented in Fig. 11.13. It can be seen that the introduction of the swing leg dynamics introduces a significant deviation of the constant energy level of the bipedal SLIP model, indicated by the dashed line. The bulges in the kinetic energy plot clearly show the accelerating and the decelerating of the swing leg.

The energy balance for the swing leg model with leg retraction (Section 11.5) is shown in Fig. 11.14. It clearly shows that the leg retraction further slows down the system, as exemplified by the lower total energy level when compared to Fig. 11.13. However, it is also noted that the bulges observed in Fig. 11.13 have been reduced in amplitude in Fig. 11.14. This is because the leg retraction results in a lower swing leg inertia, mitigating the influence of the swing of the leg.

Both Fig. 11.13 and Fig. 11.14 show relatively small variations in the total energy level. Intuitively, this could be interpreted as energy-efficient, as it signifies that only small amounts of energy are exchanged with the environment and via the control action.

11.6.3 Cost of Transport

Cost of transport (also known as specific resistance) is a measure of energy efficiency, as it measures the energy that a system uses to travel a specified distance [23, 30]. Using the definition proposed in [30], the cost of transport is obtained by exploiting the port-Hamiltonian formulation of the dynamic equations

(11.5), (11.13), (11.18):

$$C = \frac{1}{m_{\text{total}} g_0 \Delta x} \int_T |\langle u|y\rangle| \, \mathrm{d}t, \tag{11.20}$$

where m_{total} denotes the total mass and Δx the distance traveled during the time T. The cost C captures the amount of energy required for walking the distance Δx, taking into account that, in general, actuators dissipate energy when negative work is done, rather than storing it.

Using (11.20), we find $C = 3 \cdot 10^{-3}$ for the controlled V-SLIP model. The cost is not exactly zero due to the aforementioned mismatch between the reference trajectory and the true natural dynamics: if the reference had been exact, we would have $C \equiv 0$. For the model with swing leg (Section 11.4), we obtain $C = 0.32$. For the model with the retracting swing leg (Section 11.5), we obtain $C = 0.34$. While Fig. 11.14 hinted to lower energy expenditure when compared to Fig. 11.13, this gain in efficiency is offset by the lower average velocity. The cost of transport $C = 0.34$ is in the same range as of human walking [23], and thus the proposed control strategy can be considered energy efficient in the sense that it is shown that the theoretical performance approaches that of human walking.

11.7 Conclusions

In this paper, we presented a constructive method for designing a control strategy for a bipedal walker. The starting point was the bipedal spring-loaded inverted pendulum model, extended by variable leg stiffness to provide control inputs. Subsequent modeling iterations extended the model to include full swing leg dynamics, while at the same time the control strategy was extended to handle the refined models. The final result is a template model of a bipedal walker, based on the principles of the bipedal spring-loaded inverted pendulum, and an energy-efficient controller with a performance level comparable to human walking. This model plus controller can serve as the basis for control of bipedal robots.

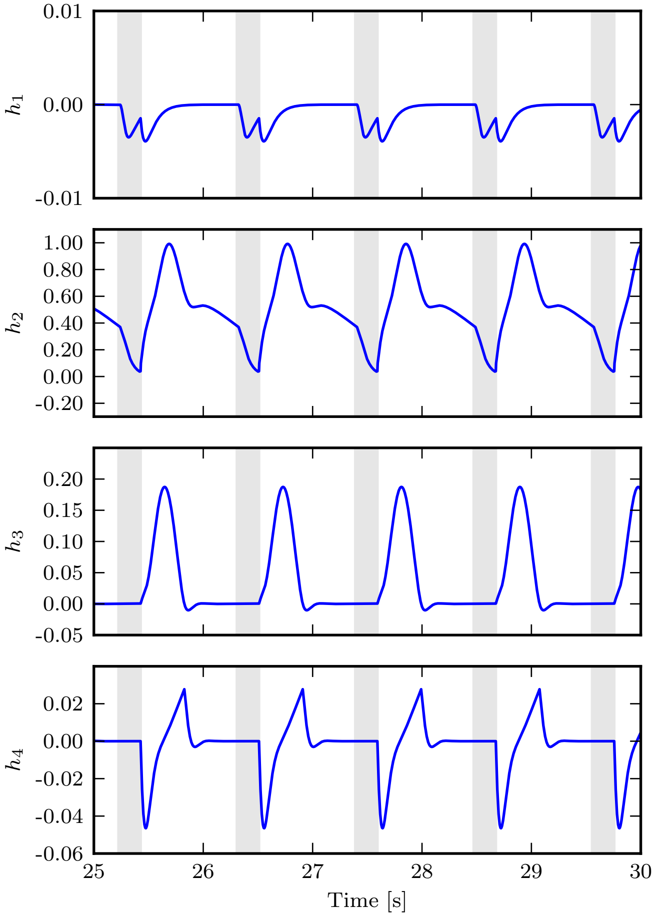

Figure 11.10: Steady-state error functions for the controlled V-SLIP model with leg retraction—It can be seen that the error functions converge like claimed in Proposition 11.3. Note that $h_3 \equiv 0$ and $h_4 \equiv 0$ during the double support phase.

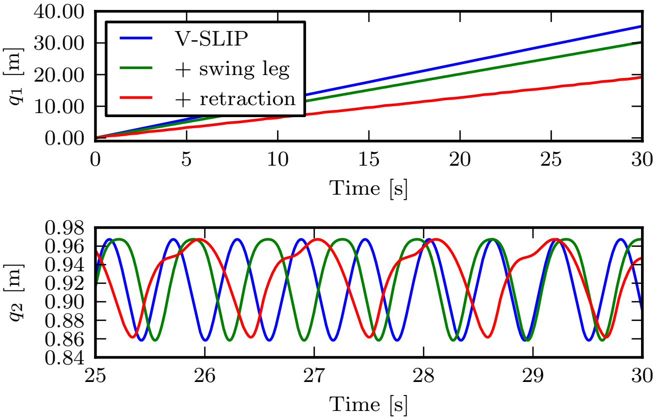

Figure 11.11: Hip trajectories $q_1(t)$ and $q_2(t)$—It can be observed that swinging and retracting the leg has a negative influence on the forward velocity. This influence is particularly apparent in the vertical hip position trajectories.

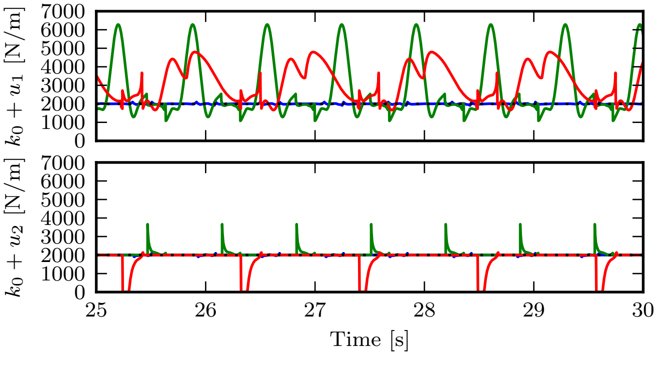

Figure 11.12: Control inputs—See Fig. 11.11 for the legend. The controlled V-SLIP model hardly requires any control input to track the reference, which is by design of the control strategy. Adding the swing leg and retracting introduces a significant disturbance in the dynamics, and thus more control input. Note that $u_2 \equiv 0$ during the single support phase.

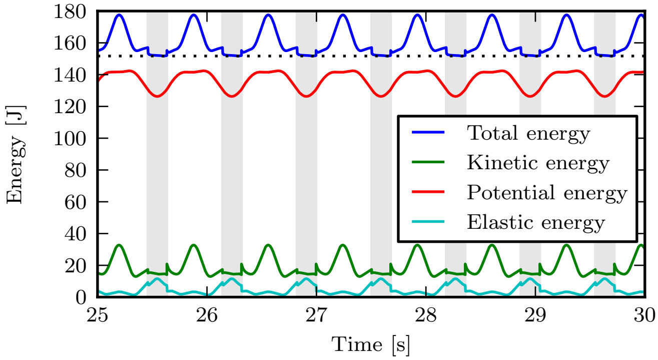

Figure 11.13: Energy balance for the controlled V-SLIP model with swing leg—The dashed line indicates the constant energy level of the bipedal SLIP model. The influence of the swing leg is clearly seen in the bulges in the kinetic energy.

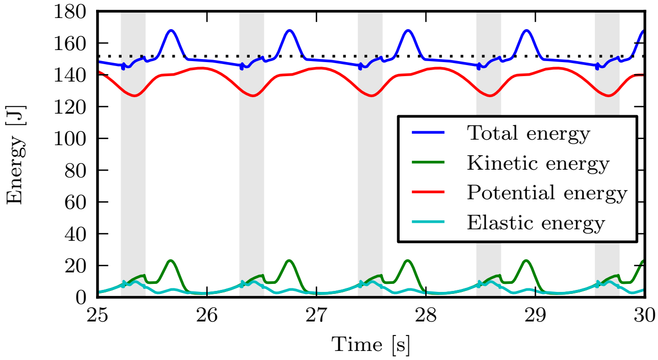

Figure 11.14: Energy balance for the controlled V-SLIP model with leg retraction—The dashed line indicates the constant energy level of the bipedal SLIP model. Also here the influence of swinging and retracting the swing leg is clearly seen.

Part III

Appendix

APPENDIX A

CONTROLLER DESIGN FOR A BIPEDAL WALKING ROBOT USING VARIABLE STIFFNESS ACTUATORS

Jildert G. Ketelaar, Ludo C. Visser, Stefano Stramigioli, Raffaella Carloni

in: *Proceedings of the IEEE International Conference on Robotics and Automation*, 2013

A.1 Introduction

The human musculoskeletal system enables highly energy-efficient and robust walking. However, walking machines are not yet close to achieving similar performance with the same level of robustness. In particular, robotic walkers are either energy-efficient, such as passive dynamic walkers [41, 11], or robust, such as PETMAN [6]. In order to be able to build robotic walkers that can come close to human performance levels, a better understanding of human walking is needed.

Human-like walking can be modeled by bipedal Spring-Loaded Inverted Pendulum (SLIP) model, which reproduces, to a large extent, the human hip motion and ground reaction forces observed in human gaits [21]. As shown in [44], the stiffness of the legs not only influences the type of gait, but also robustness against external disturbances. This property inspired the introduction of the bipedal Variable Spring-Loaded Inverted Pendulum (V-SLIP) model, in which the leg stiffness can be continuously varied [69]. It was shown that a controller exists that, by active variation of the leg stiffness, renders an arbitrary gait asymptotically stable, thus further improving the robustness.

Table A.1: Properties of model abstraction levels

Model	Abstraction	Legs	Mass distribution
V-SLIP	high	telescopic linear springs	point mass at hip
V-SLIP with knees	middle	segmented legs, compliant knee	realistic inertias of upper and lower leg
Robot model	low	segmented legs, VSA in knee	realistic inertias of upper and lower leg

The main shortcoming of the bipedal SLIP and V-SLIP models is that they are purely conceptual. In particular, any robotic walker will be influenced by swing leg dynamics and energy losses due to foot impacts, which have not been incorporated in these models. In [20], it was shown that it is possible to use the passive gait of the bipedal SLIP model onto a fully actuated bipedal robot model by projecting the bipedal SLIP dynamics onto the robot dynamics. In [70], it was shown that the control strategy developed for the V-SLIP model can be extended to handle the swing leg dynamics.

In this work we present a control strategy for a bipedal robot, actuated by variable stiffness actuators (VSAs), a class of actuators that allow the actuator output position and stiffness to be controlled independently. With these actuators, the robot realizes controllable leg compliance, so that it closely matches the bipedal V-SLIP model. The control strategy is implemented using different abstraction levels for a bipedal robot model. At the highest abstraction level the model is the bipedal V-SLIP model, as presented in [69]. One level below, the model features variable compliant elements in the knees and non-massless leg elements. At the lowest abstraction level, physical elements are considered, such as the models of the motors and the VSAs. Table A.1 lists the three different model abstraction levels and their features. The effectiveness of the control strategy is demonstrated by numeric simulation and experiments performed on the robot.

This paper is organized as follows. Section A.2, Section A.3, and Section A.4 describe the models listed in Table A.1 and present control strategies for gait control at that particular level of abstraction. Section A.5 presents the integrated control strategy, and in Section A.6 numeric simulation results are presented, validating the controller design. Preliminary experimental results are presented in Section A.7. Section A.8 concludes the paper with final remarks.

A.2 V-SLIP Model and Controller

This Section covers both the model and the controller design for the highest abstraction level considered in this work, i.e., the V-SLIP model, as proposed in our previous work [69] and illustrated in Fig. A.1.

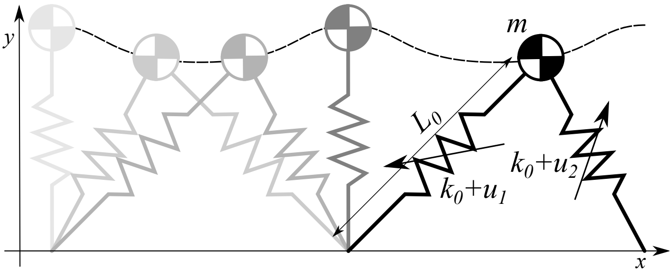

Figure A.1: The V-SLIP model—The model consists of a point mass m, and two massless telescopic springs with controllable stiffness $k_0 + u_i, i = 1, 2$ and rest length L_0. A walking gait is a periodic hip trajectory $(x(t), y(t))$.

A.2.1 Model Description

The V-SLIP model consists of a point mass m located at the hip and two massless telescopic linear springs with rest length L_0 and variable stiffness $k_0 + u_i$. The system is restricted to the sagittal plane, so that the hip position is described by the planar coordinates (x, y). The control inputs to the V-SLIP model are the stiffness variation u_1 and u_2.

The dynamics of the V-SLIP model are described by [69]

$$\begin{bmatrix} m & 0 \\ 0 & m \end{bmatrix} \begin{bmatrix} \ddot{x} \\ \ddot{y} \end{bmatrix} + \begin{bmatrix} 0 \\ mg_0 \end{bmatrix} - F_{s_0}(x, y) = F_{s_u}(x, y),$$

where g_0 is the gravitational acceleration, F_{s_0} the force exerted by the springs on the mass due to the nominal spring stiffness k_0, and F_{s_u} the force exerted on the mass due to the control inputs u_i.

The dynamics of the V-SLIP model are hybrid in nature, due to the foot lift-off and touchdown events throughout the walking gait. In particular, we consider three specific domains. When both feet are in contact with the ground, the biped is said to be in the *double support* phase and both control inputs can then be used to control the hip motion of the biped. When only one foot is in contact with the ground, the biped is said to be in the *single support* phase, during which only one control input can be used to control the hip motion. Furthermore, it might happen that a *flight* phase occurs, when both feet lose contact with the ground.

A.2.2 Control Strategy

A control strategy for the bipedal V-SLIP model, which renders its dynamics asymptotically converging to an arbitrary gait of the bipedal SLIP model, has been proposed in [69]. The reference gait is obtained from the bipedal SLIP model with a nominal leg stiffness k_0 and spring rest length L_0 [21]. Because the horizontal position of the hip x is a monotonically increasing variable, it is possible to parameterize a specific gait by this variable. The reference gait can then be fully described by the hip height $y(x)$ and the forward hip velocity $\dot{x}(x)$. These two variables are chosen as a reference because they are a measure for a part of the amount of energy associated with the gait, potential energy and kinetic energy respectively. The control objective is then formulated as follows:

Problem A.1 *Given a parameterized reference gait as* $(y^*(x), \dot{x}^*(x))$*, find control inputs* u_1 *and* u_2*, such that*

$$\lim_{t\to\infty} y^*(x(t)) - y(t) = 0,$$

and, for some small $\varepsilon > 0$*,*

$$\lim_{t\to\infty} |\dot{x}^*(x(t)) - \dot{x}(t)| < \varepsilon,$$

i.e., such that the trajectory $(x(t), y(t))$ *approaches the reference gait asymptotically, with bounded error in the desired forward velocity.*

From the error in the hip height and the error in the forward velocity, the V-SLIP controller derives the change in leg stiffness u_1 and u_2, which is added to the nominal stiffness k_0 to obtain the total leg stiffness. During the single support phase, the controller only derives one control input, since there is only one leg touching the ground, and the swing leg is not considered in the V-SLIP model. During the double support phase, the controller calculates control inputs for both legs. Given the leg stiffness, the force $F_i, i = 1, 2$ that is applied along the legs of the V-SLIP model is then:

$$F_i = (k_0 + u_i)(L_i - L_0), \quad i = 1, 2, \tag{A.1}$$

where L_i is the leg length.

A.3 V-SLIP Model with Knees and Controller

The model described in Section A.2 is purely conceptual, since the legs are massless and the swing leg is completely ignored. In order to go to a realistic model of a bipedal robot, this Section describes a model with a lower level of abstraction, i.e. the V-SLIP model with knees, and extends the control strategy.

A.3.1 Model Description

The V-SLIP with knees model is shown in black in Fig. A.2, overlapped to the V-SLIP model in gray. The V-SLIP model with knees consists of four rigid bodies: an upper and lower leg for each leg. For each body the center of mass is indicated, labeled as m_{ul} and m_{ll}. It is assumed that the masses of the upper legs are larger than the lower legs, with a total mass distribution such that the center of mass is close to the hip joint, aimed to closely approach the point mass distribution of the

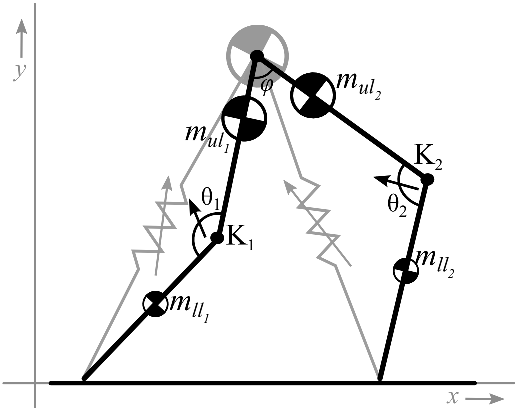

Figure A.2: The V-SLIP model with knees—The model features variable stiffness knee joints and its mass distribution is such that it approaches that of the V-SLIP model, depicted in gray.

V-SLIP model. The bodies are connected by means of three joints: the upper legs by the hip joint, and each pair of upper and lower leg by a knee joint.

From Fig. A.2 it is observed that the virtual spring legs of the V-SLIP model (shown in gray) are realized by a segmented leg configuration, where the upper and lower leg are connected by torsion springs with variable stiffness. The knee angles are denoted by $\theta_i, i = 1, 2$ and the angle between the two upper legs, i.e., the hip angle, as φ.

A.3.2 Stance Leg Control

In order to implement the control strategy proposed for the V-SLIP model, a mapping is required between the telescopic springs of the V-SLIP model and the segmented legs of the kneed model, if these are in contact with the ground. In particular, the forces derived in (A.1) need to be realized by appropriate variations of the torsional knee stiffness, as function of the knee angle θ_i.

The conversion is visualized in Fig. A.3. The moment arm a, which defines the relation between the translational and rotational domain ($\tau = a \cdot F$), is equal to the shortest distance between the knee joint and the virtual leg. It can be easily shown that this distance is equal to

$$a = \frac{l_1 l_2}{L_i} \sin(\theta_i),$$

where l_1 and l_2 are the lengths of upper and lower leg. The singularity $\theta_i = \pi$ is to be avoided by an end-stop.

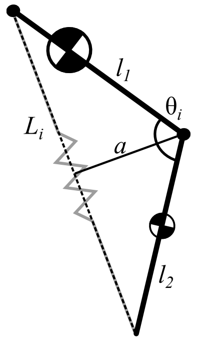

Figure A.3: Visualization of the mapping of the V-SLIP model—The behavior of the telescopic legs of the V-SLIP model is implemented by the variable stiffness springs in the knee joints.

A.3.3 Swing Leg Control

The motion of the swing leg in the single support phase is governed by a motion profile generator. The generator computes reference trajectories for the hip and knee joint, based on a estimation of the swing duration. The motions are designed such that the swing leg is first retracted, then swung forward, and then extended again for touchdown. To achieve the desired motion of the knee joint, the stiffness of the knee joints are controlled to have high stiffness for accurate motion tracking, but a lower stiffness just before the predicted moment of touchdown to absorb the impact force.

A.4 Robot Model and Controller

This Section describes a third and final model refinement of a bipedal robot, incorporating variable stiffness actuators, and the corresponding extension of the control strategy.

A.4.1 Model Description

The robot model is based on CAD drawings of the real robot and implemented using the *3D Mechanics Toolbox* of the *20-sim* software package(Controllab Products B.V., Enschede, The Netherlands). A visual representation of the model is depicted in Fig. A.4. It includes full 3D dynamics, ground contact models, and actuator dynamics. The sideways motion of the robot is constrained by a guide rail in order to keep the motion in the sagittal plane.

The required variable leg compliance of the biped model is implemented by means of variable stiffness actuators in the knees. This class of actuators are characterized by the property that they can change the output position and stiffness independently. By using these actuators in the knee joints of the robot, the variable

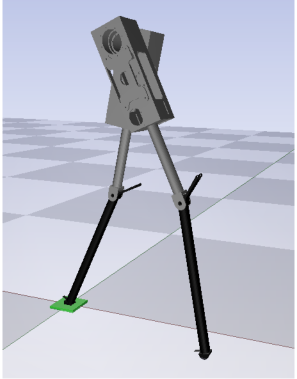

Figure A.4: Visual representation of the robot model—The model is implemented using the CAD drawings of the robot design, and includes full 3D dynamics and ground contact models.

leg stiffness behavior of the bipedal V-SLIP model can be reproduced. In this work, the vsaUT-II [26] variable stiffness actuator is used. This actuator uses the concept of a lever with a moving pivot to vary the apparent output stiffness. Considering two springs with a fixed stiffness k and a lever length d, the apparent output stiffness K is given by:

$$K(q_1) = \frac{\partial \tau}{\partial \theta_i} = \left(\frac{q_1}{d - q_1} \right)^2 \cdot 2 \cdot k,$$

where q_1 is the position of the pivot. This method enables to realize an output stiffness in the range of zero stiffness ($q_1 = 0$) and infinite stiffness ($q_1 = d$).

Besides q_1, the vsaUT-II has a second degree of freedom, i.e., q_2, which defines the equilibrium position of the output. The torque delivered by the actuator at the output is a function of the state of the internal springs, the output position θ_i, and the two degrees of freedom q_1 and q_2.

A.4.2 VSA Control

The V-SLIP model with knees assumes an ideal variable compliant knee element and, therefore, the control of the VSA needs to be added to the previously presented controller. In particular, in Section A.3 a required knee torque τ_d, together with a desired knee stiffness K_d, has been derived. These two quantities are the inputs to the VSA controller that calculates the required motion for the degrees of freedom q_1 and q_2 of the actuator.

The VSA controller is based on the controller presented in [65]. Given the desired knee torque τ_d, and given the exerted torque τ from the vsaUT-II model [26], we define a desired rate of change

$$\dot{\tau}_d = \kappa_p (\tau_d - \tau),$$

for some $\kappa_p > 0$. The rate of change of the output torque delivered by the VSA can be shown to be of the form

$$\dot{\tau} = V_q \begin{bmatrix} \dot{q}_1 \\ \dot{q}_2 \end{bmatrix} + V_\theta \dot{\theta}_i, \tag{A.2}$$

where the matrix function V_q and the scalar function V_θ follow from the actuator kinematics, and $\dot{\theta}_i$ is the rate of change of the output angle of the actuator.

In order to find the required $(\dot{q}_1, \dot{q}_2)$ to realize $\dot{\tau}_d$, (A.2) needs to be inverted. However, V_q is not square, causing the problem to be under-constrained. To resolve the redundancy, [65] proposes to use a weighted pseudo inverse of the form

$$V_q^\sharp = M^{-1} V^T \left(V M^{-1} V^T \right)^{-1}, \tag{A.3}$$

with M given by

$$M = \begin{bmatrix} w_1 & 0 \\ 0 & w_2 \end{bmatrix}.$$

Here w_1 and w_2 are functions of q_1 and q_2, respectively. The purpose of the weighting functions w_i is to control the ratio between $\dot{q}_1$ and $\dot{q}_2$, and are constructed to appoint near-infinite weight to a degree of freedom approaching its extremal positions. In the vsaUT-II, the motor controlling q_1 is much smaller than the motor controlling q_2, and therefore the former is given a higher weight to prevent overloading of the motor.

Given the pseudo inverse (A.3), (A.2) can be inverted, yielding

$$\dot{q} = V_q^\sharp \left(\dot{\tau}_d - V_\theta \dot{\theta}_i \right) + g(K_d),$$

where the function $g(K_d)$ is a special function that regulates the VSA output stiffness K to the torsional equivalent K_d of k_0 in the null-space of V_q, i.e. it attempts to keep the virtual leg stiffness close to k_0 without interfering with effectuation of τ_d (see [65] for details).

A.5 Integrated Control Architecture

The previous Sections have covered three iteration steps of modeling and control a bipedal robot. The three controllers form a complete controller for the robot model, as shown in Fig. A.5. The V-SLIP controller, shown on the left, maps the robot state on the V-SLIP model and calculates leg stiffness variations for the V-SLIP model. Then, in a second layer, these stiffness variations are mapped onto the knees of the bipedal model and along with this control, trajectories for the swing leg and hip trajectory are calculated. At the next level, the VSA control maps the desired knee torques during stance onto the individual degrees of freedom of the vsaUT-II. After this, a switching block selects the correct control inputs for the different joints, i.e. stiffness control during the stance phase and motion control during the swing phase. The low-level I/O block computes the required motor currents in order to achieve the desired torques or motions.

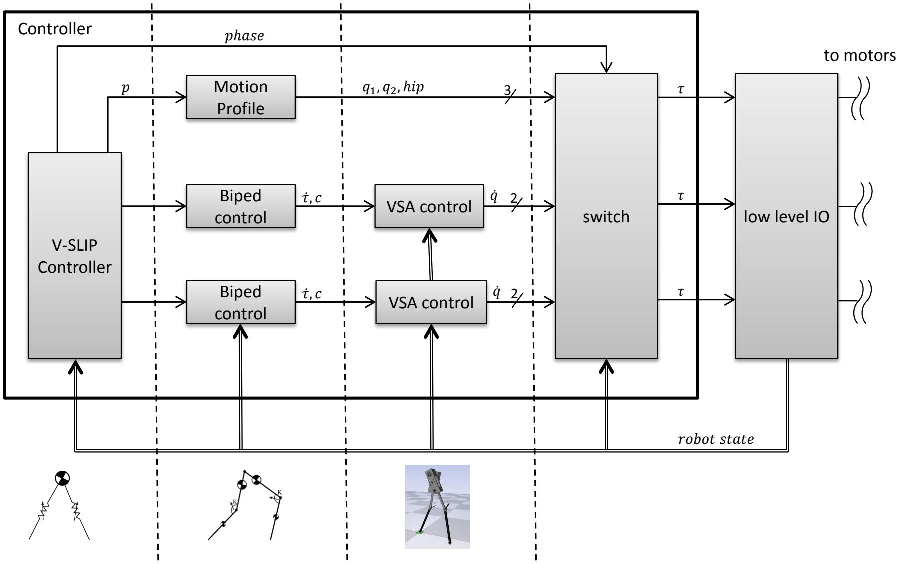

Figure A.5: Multi-layer control architecture—The first layer maps the robot state onto the V-SLIP model. The resulting control action are then mapped to the V-SLIP model with knees. The third level maps these torques onto the control of the variable stiffness actuators. A low-level controller switches between stiffness control in stance phase and motion control during swing.

A.6 Simulation Results

In this Section, numeric simulation results are presented that validate the control strategy. For the simulations the robot model described in Section A.4 is used, together with the complete control structure as outlined in Section A.5.

In Fig. A.6, the top plot shows the vertical position y of the hip during walking, together with the reference y^* obtained from the SLIP model. It can be seen that in steady state conditions, the height of the robot deviates approximately a centimeter from the reference of the conceptual SLIP model. The lower plot shows the forward velocity $\dot{x}$ of the hip, together with the reference $\dot{x}^*$. The spikes are caused by the impact of the feet with the ground. It is observed that the velocity is out of phase with the reference. This is due to the dynamics of the swing leg, which need to be swung forward during the single support phase. The motion of the inertia of the swing leg causes extra acceleration and deceleration of the hip. Despite these deviations in hip height and velocity, a stable gait is obtained, as shown in the movie attachment.

The hip and the knee motion during four steps are shown in Fig. A.7, to illustrate the switching between VSA control and motion control. The hip angle φ shows a smooth periodic motion, representing the hip swinging forward and backward during subsequent steps. The motion of the knee angles is shown in the

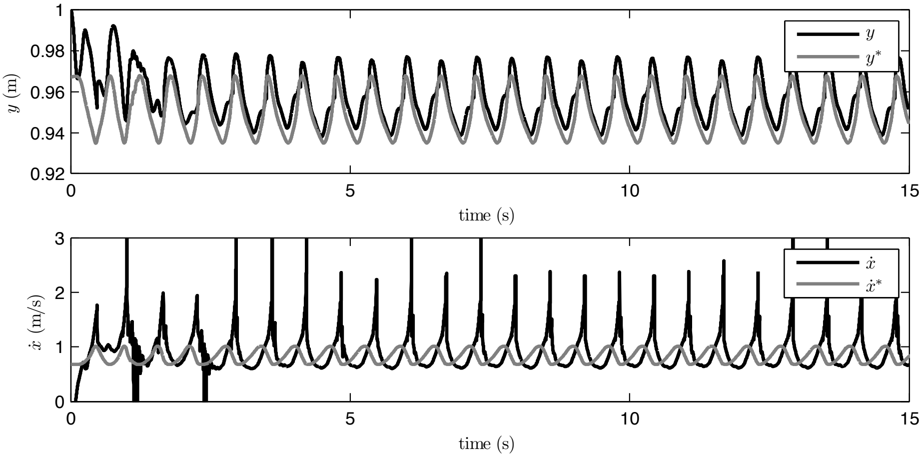

Figure A.6: Simulation results—The top plot shows the hip height y of the bipedal robot, along with the reference $y^*(x)$. The lower plot shows the forward velocity $\dot{x}$ of the hip plotted, along with the reference $\dot{x}^*$. It can be seen that a stable gait is attained.

bottom plot. During the swing phase the knee is controlled to an angle $\theta = 2.0$ rad, retracting the leg to avoid foot scuffing. Before ending the swing phase, the knee angle is controlled to $\theta = 2.86$ rad, extending the leg to its full length just before impact. During the stance phase, the knee is passively compressed to an angle $\theta \approx 2.5$ rad.

A.7 Experimental Results

The robot modeled in Section A.4.1 has been constructed, as shown in Fig. A.8.[1] This Section presents an overview of the mechanical realization and preliminary experimental results.

A.7.1 Mechanical Realization of the Robot

The robot features different properties which are required to match the original V-SLIP model as close as possible. In the V-SLIP model, most of the total mass of the robot is located close to the hip joint. To meet this requirement, the upper and lower leg parts are made of light-weight carbon fiber tubes. Also the variable stiffness actuators, which act on the knee joint, are situated close to the hip joint. A light-weight transmission rod connects the output of the variable stiffness actuator to the knee joint. The left and right leg are connected by an actuated hip joint. In order to constrain the motion of the robot to the sagittal plane, a set of linear

---

[1] Details on the design can be found in Appendix B.

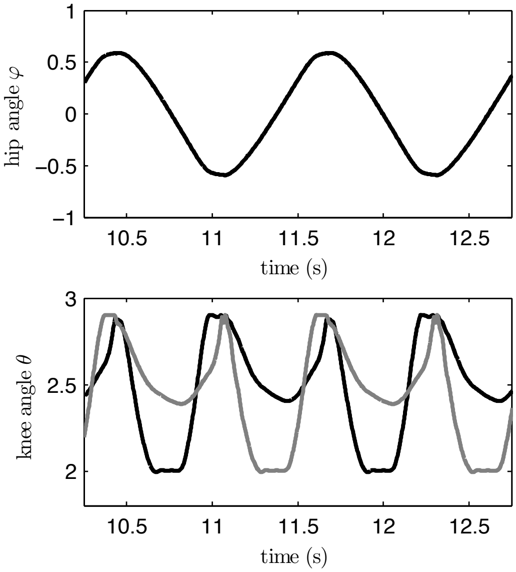

Figure A.7: Hip and knee angles during simulation—The top plot shows the periodic hip motion, and the bottom plot shows the knee angles for both the left and right leg.

guides is used, connected to the left leg via a passive joint. A treadmill is used as walking surface.

The electronics is based on the micro-controller, providing the low-level I/O with the motor drivers and sensors. The micro-controller communicates with a PC, on which the control architecture is implemented in *Simulink* (The Mathworks Inc., Natick, MA, USA) in real-time.

A.7.2 Preliminary Experimental Results

With the control architecture implemented, a preliminary experiment has been performed, in which the robot has been able to walk approximately seven steps autonomously. The results of these experiments are presented in this Section and in the movie attachment.

Fig. A.9a shows the hip height y and the forward velocity of the hip $\dot{x}$ (shown in black), along with reference gait (shown in gray). It is observed that the hip height trajectory show the correct periodic behavior, but the average height is decreasing over time. From the forward velocity it is observed that the average velocity of the hip stays in the same order of magnitude as the desired velocity.

Fig. A.9b shows the hip and the knee motion during the same steps as presented in Fig. A.9a. The top plot shows the motion of the hip, which shows agreement with the simulation results presented in Fig. A.7. The bottom plot shows the knee angles trajectories: in gray for the left leg and in black for the right leg. The global

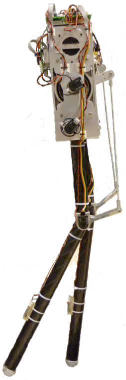

Figure A.8: Photograph of the bipedal robot—The robot design corresponds to the model described in Section A.4.1.

behavior of leg retraction during swing and passive compression during stance can be observed.

A.8 Conclusions and Future Work

We presented a control strategy for a bipedal robot with variable stiffness actuators. The different degrees of freedom of the robot are controlled at different levels of abstraction. With this approach, the control problem remains tractable. The effectiveness of the controller was demonstrated by simulations and preliminary experiments.

A stable gait was attained in simulation, and it was shown in preliminary experiments that the robot is capable of autonomous walking. However, this gait cannot yet be sustained for longer periods of time, because, as observed in Fig. A.9a, the robot is slowly losing height, ultimately leading to foot scuffing and tripping. An improved robot model, capturing complex dynamics and nonlinear friction phenomena that the current model does not yet include, and technological improvements of the robot design, will address these issues.

Acknowledgment

The authors would like to thank Wouter de Geus for his contribution to the design and construction of the robot.

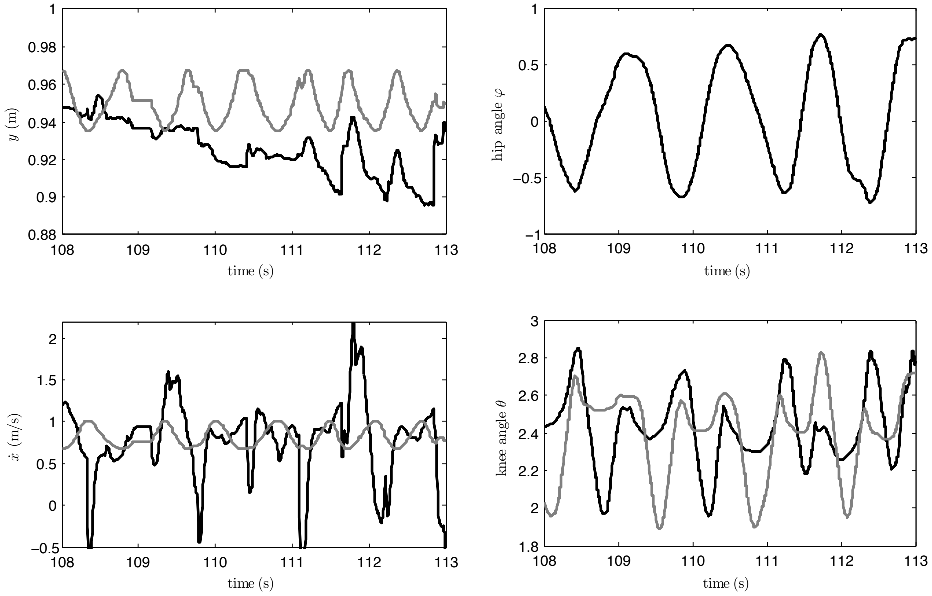

(a) Hip reference trajectories

(b) Hip angle and knee angle trajectories

Figure A.9: Experimental results—On the left, the top plot shows the hip height y (black) during seven succeeding stepst, and the reference trajectory (gray). The bottom plot shows the forward velocity $\dot{x}$ of the hip, and also the reference. On the right, he top plot shows the periodic hip angle trajectory, and the lower plot shows the knee angle trajectories.

APPENDIX B

Description of the Robot Design

This appendix describes the design of the robot used in the experiments described in Appendix A, summarizing the work presented in [12, 37]. The design requirements are reviewed, and an overview of the mechanical, electrical, and software components of the robot is given.

B.1 Design Requirements

The purpose of the robot is to investigate the control strategies presented in Chapter 5. Therefore, the robot design should incorporate the characteristic features of the models that have been used in deriving the control strategies. In particular, since the bipedal V-SLIP model, introduced in [69] and described in Section 5.2, is at the basis of this line of research, the robot design should aim to resemble this model as closely as possible.

The characteristic properties of the V-SLIP model are summarized as follows:

- point mass in the hip;
- massless telescopic springs, with variable stiffness, representing the legs;
- motion constrained to the sagittal plane.

The robot design should reproduce these properties as closely as possible, while also be able to deal with the non-ideal properties of bipedal walking that are not captured by the V-SLIP model. In the context of these considerations, the following requirements for the robot design have been derived:

- the mass distribution of the robot should be such that most of the mass is located close to the hip joint;

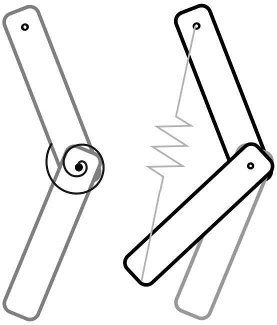

Figure B.1: Conceptual leg design—By segmenting the leg, with a variable compliant element in the connecting joint, a virtual telescopic spring element can be realized between the extremal points of the leg.

- a passive compliance with variable stiffness must be implemented in such a way that a (virtual) telescopic spring can be realized between the hip joint and the foot of the leg;
- the motion of the robot must be constrained to the sagittal plane;
- an actuated degree of freedom in each leg to retract it during the swing phase, with the aim of avoiding foot scuffing;
- an actuated hip joint to control the swing leg motion.

Based on these requirements, a concept has been designed based on segmented legs with a variable compliant element connected to the knee joints, as shown in Figure B.1. In this way, a virtual telescopic spring can be realized between the hip and foot of the leg by appropriate stiffness variations at the output of the actuator. Moreover, by controlling the equilibrium position of the joint, and setting the output stiffness sufficiently high, motion control algorithms can be employed to retract the leg during the swing phase.

B.2 Mechanical Realization

The concept has been realized as shown in Figure B.2. In view of the design requirements, a number of characteristic features can be identified.

The robot essentially consists of two largely identical legs, connected by a hip joint. The hip joint is actuated by a conventional DC-motor, so that the swing motion of the legs can be accurately controlled. The legs are constructed from carbon fibre material and aluminum parts, with the aim of keeping the weight low. The legs are segmented by a knee joint, which is actuated by the vsaUT-II variable stiffness actuator [26]. The variable stiffness actuator is placed close to the hip joint, with the aim of approaching the ideal mass distribution of the V-SLIP model

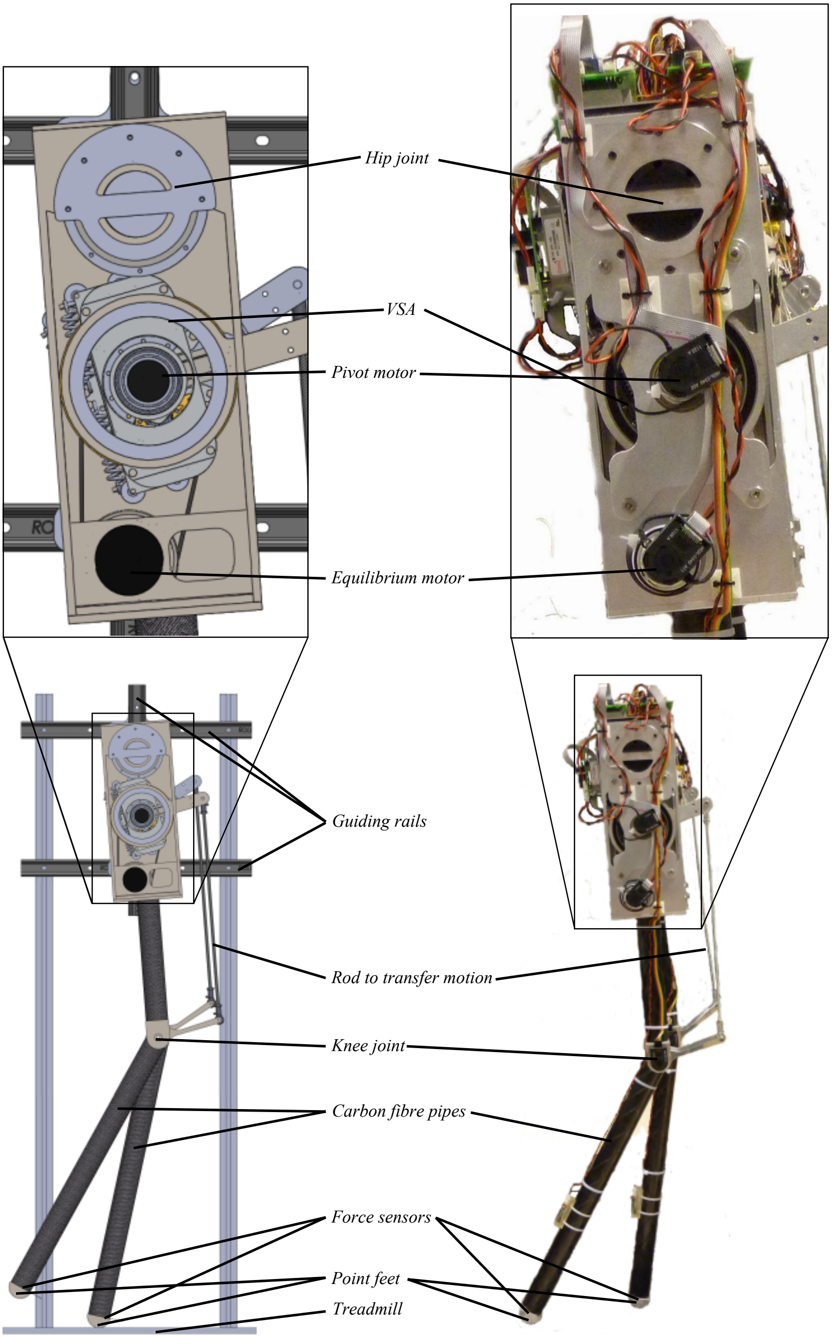

Figure B.2: Robot design and realization—On the left, a CAD drawing of the robot design is shown. On the right, a photograph of the realized system.

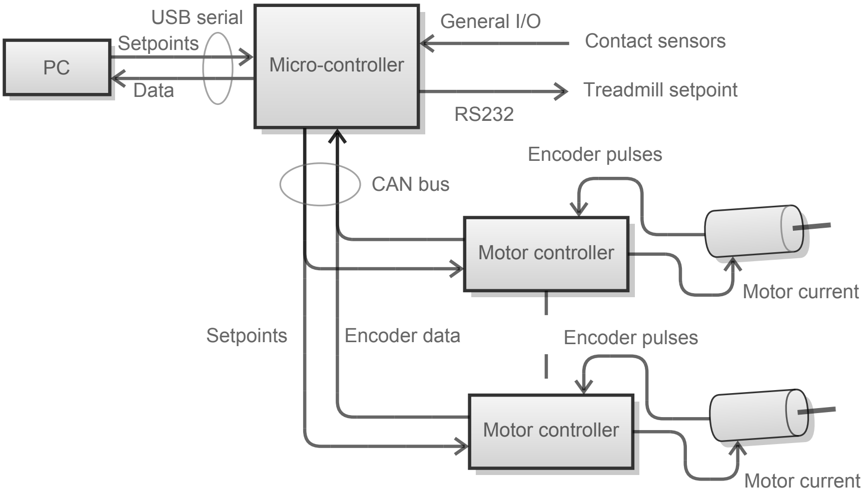

Figure B.3: Organization of robot electronics—The microcontroller orchestrates the coordination between the various components. It acquires sensor data from the foot sensors and various encoders, and receives setpoints for the motor and treadmill controllers.

as close as possible. The output of the actuator is connected to the knee joint by a pulling rod, and thus controls the equilibrium angle of the knee joint and the joint stiffness.

In order to constrain the motion of the robot to the sagittal plane, a set of guide rails is employed. An attachment point, which is free to move in the sagittal plane via the rails, is attached to the robot through a passive rotation joint, connected to the robot in the rotation axis of the hip. In order to facilitate unrestricted forward motion of the robot, a treadmill is used as a walking surface. By estimating the forward velocity of the robot, the treadmill speed is matched to the robot speed.

B.3 Electronics and Software

The electronics of the robot are organized as depicted in Figure B.3. The central component is an MBED prototyping board (ARM Ltd., Cambridge, UK), which is based on the NXP LPC1768 Cortex-M3 microprocessor. The microcontroller acquires sensor data from contact sensor in the foot and the various encoders of the robot joints and motors. This sensory data is sent to the PC via USB, providing the input to the control algorithm, described in Appendix A, which is implemented on the PC in *Simulink* (The Mathworks Inc., Natick, MA, USA), running in real-time. The motor setpoints, calculated by the control model, are sent back to the microcontroller, which sends these to the motor controllers (Elmo Motion Control Ltd., Petach-Tikva, Israel) and the treadmill speed controller.

B.4 Recommendations for Improvements

While the robot has been shown to be capable of autonomous walking, it was found that some aspects of the robot design need to be improved in order to be able to achieve robust performance and sustained walking gaits.

- The original vsaUT-II design, as presented in [26] has been modified to better meet the performance requirements of the robot. However, some performance issues have been identified that should be addressed. In particular, the load imposed by the robot during the stance phase induces significant friction in the pivot point and the attachment points of the springs. This friction is highly nonlinear and deteriorates the actuator performance in dynamically changing the output stiffness.
- The control strategies presented in Chapter 5 rely on the availability of the full state of the robot, as well as that of the abstracted models (e.g. the V-SLIP model). In the current design, the joint angles are measured by encoders, and the rate of change of these quantities is numerically computed. The noise introduced by these computations has been shown problematic in reconstructing the state variable measurements for the abstracted models. The robot performance can likely be improved considerably by improved state measurements and state reconstruction, in particular of the velocities.
- An important aspect any control strategy for a walking robot is determining in which phase of the gait the robot is, i.e. the single support phase, double support phase, etc. The current robot design employs simple pressure sensors to determine which of the feet are in contact with the ground, and thus determining the phase of the gait. However, these sensors are susceptible to chattering due to the rigid contact of the feet with the ground. An improved foot design and sensor could likely improve the robot performance by reducing bouncing and slip of the feet.

BIBLIOGRAPHY

[1] A. Albu-Schäffer, O. Eiberger, M. Grebenstein, S. Haddadin, C. Ott, T. Wimböck, S. Wolf, and G. Hirzinger. Soft robotics. *IEEE Robotics and Automation Magazine*, 15(3):20–30, 2008.

[2] V. I. Arnol'd. *Mathematical Methods of Classical Mechanics.* Springer-Verlag, 1989.

[3] A. Ben-Israel and T. N. E. Greville. *Generalized Inverses.* Springer, 2003.

[4] A. Bicchi, S. L. Rizzini, and G. Tonietti. Compliant design for intrinsic safety: general issues and preliminary design. In *Proceedings of the IEEE/RSJ International Conference on Intelligent Robots and Systems*, pages 1864–1869, 2001.

[5] A. Bicchi and G. Tonietti. Fast and 'soft-arm' tactics: Dealing with the safety-performance tradeoff in robot arms design and control. *IEEE Robotics and Automation Magazine*, 11(2):22–33, 2004.

[6] Boston Dynamics. PETMAN - BigDog gets a big brother. online: http://www.bostondynamics.com/robot_petman.html, 2011.

[7] F. Bullo and A. D. Lewis. *Geometric Control of Mechanical Systems.* Springer, 2004.

[8] R. Carloni, L. C. Visser, and S. Stramigioli. Variable stiffness actuators: a port-based power flow analysis. *IEEE Transactions on Robotics*, 28(1):1–11, 2012.

[9] J. Choi, S. Park, W. Lee, and S.-C. Kang. Design of a robot joint with variable stiffness. In *Proceedings of the IEEE International Conference on Robotics and Automation*, pages 1760–1765, 2008.

[10] R. H. Clewley, W. E. Sherwood, M. D. LaMar, and J. M. Guckenheimer. PyDSTool, a software environment for dynamical systems modeling. online: http://pydstool.sourceforge.net, 2007.

[11] S. Collins, A. Ruina, R. Tedrake, and M. Wisse. Efficient bipedal robots based on passive-dynamic walkers. *Science*, 307(5712):1082–1085, 2005.

[12] W. de Geus. Design and realisation of a biped walker with compliant legs. Master's thesis, University of Twente, 2012.

[13] A. De Luca, F. Flacco, A. Bicchi, and R. Schiavi. Nonlinear decoupled motion-stiffness control and collision detection/reaction for the VSA-II variable stiffness device. In *Proceedings of the IEEE/RSJ International Conference on Intelligent Robots and Systems*, pages 5487–5494, 2009.

[14] V. Duindam, A. Macchelli, S. Stramigioli, and H. Bruyninckx. *Modeling and Control of Complex Physical Systems.* Springer, 2009.

[15] V. Duindam and S. Stramigioli. Singularity-free dynamic equations of open-chain mechanisms with general holonomic and nonholonomic joints. *IEEE Transactions on Robotics*, 24(3):517–526, 2008.

[16] V. Duindam and S. Stramigioli. *Modeling and Control for Efficient Bipedal Walking Robots.* Springer, 2009.

[17] V. Duindam, S. Stramigioli, and J. M. A. Scherpen. Port-based asymptotic curve tracking for mechanical systems. *European Journal of Control*, 10(5):411–420, 2004.

[18] O. Eiberger, S. Haddadin, M. Weis, A. Albu-Schäffer, and G. Hirzinger. On joint design with intrinsic variable compliance: Derivation of the DLR QA-joint. In *Proceedings of the IEEE International Conference on Robotics and Automation*, pages 1687–1694, 2010.

[19] F. Ficuciello, R. Carloni, L. C. Visser, and S. Stramigioli. Port-hamiltonian modeling for soft-finger manipulation. In *Proceedings of the IEEE/RSJ International Conference on Intelligent Robots and Systems*, 2010.

[20] G. Garofalo, C. Ott, and A. Albu-Schäffer. Walking control of fully actuated robots based on the bipedal SLIP model. In *Proceedings of the IEEE International Conference on Robotics and Automation*, pages 1456–1463, 2012.

[21] H. Geyer, A. Seyfarth, and R. Blickhan. Compliant leg behaviour explains basic dynamics of walking and running. *Proceedings of the Royal Society B*, 273(1603):2861–2867, 2006.

[22] R. Ghorbani. *On Controllable Stiffness Bipedal Walking.* PhD thesis, University of Manitoba, 2008.

[23] P. Gregorio, M. Ahmadi, and M. Buehler. Design, control, and energetics of an electrically actuated legged robot. *IEEE Transactions on Systems, Man, and Cybernetics*, 27(4):626–634, 1997.

[24] M. Griffis and J. Duffy. Global stiffness modeling of a class of simple compliant couplings. *Mechanism and Machine Theory*, 28(2):207–224, 1993.

[25] M. W. Griffis. *Kinestatic Control: A Novel Theory for Simultaneously Regulating force and displacement.* PhD thesis, University of Florida, 1991.

[26] S. S. Groothuis, G. Rusticelli, A. Zucchelli, S. Stramigioli, and R. Carloni. The vsaUT-II: a novel rotational variable stiffness actuator. In *Proceedings of the IEEE International Conference on Robotics and Automation*, pages 3355–3360, 2012.

[27] J. Guckenheimer and P. Holmes. *Nonlinear Oscillations, Dynamical Systems and Bifurcations of Vector Fields.* Springer, 1983.

[28] S. Haddadin, A. Albu-Schäffer, and G. Hirzinger. The role of the robot mass and velocity in physical human robot interaction - part I: Non-constrained blunt impacts. In *Proceedings of the IEEE International Conference on Robotics and Automation*, pages 1331–1338, 2008.

[29] S. Haddadin, A. Albu-Schäffer, and G. Hirzinger. The role of the robot mass and velocity in physical human robot interaction - part II: Constrained blunt impacts. In *Proceedings of the IEEE International Conference on Robotics and Automation*, pages 1339–1345, 2008.

[30] D. G. E. Hobbelen and M. Wisse. Controlling the walking speed in limit cycle walking. *International Journal of Robotics Research*, 27(9):989–1005, 2008.

[31] N. Hogan. Impedance control: An approach to manipulation: Part I — theory. *Journal of Dynamic Systems, Measurement, and Control*, 107(1):1–7, 1985.

[32] K. W. Hollander, T. G. Sugar, and D. E. Herring. Adjustable robotics tendon using a 'Jack Spring'$^{\mathrm{TM}}$. In *Proceedings of the International Conference on Rehabilitation Robotics*, pages 113–118, 2005.

[33] J. W. Hurst, J. E. Chestnutt, and A. A. Rizzi. An actuator with physically variable stiffness for highly dynamic legged locomotion. In *Proceedings of the IEEE International Conference on Robotics and Automation*, pages 4662–4667, 2004.

[34] A. Jafari, N. G. Tsagarakis, B. Vanderborght, and D. G. Caldwell. A novel actuator with adjustable stiffness (AwAS). In *Proceedings of the IEEE/RSJ International Conference on Intelligent Robots and Systems*, pages 4201–4206, 2010.

[35] A. Jafari, N. G. Tsagarakis, B. Vanderborght, and D. G. Caldwell. AwAS-II: A new actuator with adjustable stiffness based on the novel principle of adaptable pivot point and variable lever ratio. In *Proceedings of the IEEE International Conference on Robotics and Automation*, pages 4638–4643, 2011.

[36] M. Jafarian, G. van Oort, R. Carloni, and S. Stramigioli. Performance comparison of a planar bipedal robot with rigid and compliant legs. In *Proceedings of the 18th IFAC World Congress*, pages 6924–6929, 2011.

[37] J. G. Ketelaar. Controller design for a bipedal robot with variable stiffness actuators. Master's thesis, University of Twente, 2012.

[38] J. G. Ketelaar, L. C. Visser, S. Stramigioli, and R. Carloni. Controller design for a bipedal walking machine using variable stiffness actuators. In *Proceedings of the IEEE International Conference on Robotics and Automation*, 2013.

[39] B.-S. Kim and J.-B. Song. Hybrid dual actuator unit: A design of a variable stiffness actuator based on an adjustable moment arm mechanism. In *Proceedings of the IEEE International Conference on Robotics and Automation*, pages 1655–1660, 2010.

[40] P. Y. Li and R. Horowitz. Passive velocity field control of mechanical systems. *IEEE Transactions on Robotics and Automation*, 15(4):751–763, 1999.

[41] T. McGeer. Passive dynamic walking. *International Journal of Robotics Research*, 9(2):62–82, 1990.

[42] H. Nijmeijer and A. J. van der Schaft. *Nonlinear Dynamical Control Systems.* Springer, 1990.

[43] G. Palli, C. Melchiorri, and A. De Luca. On the feedback linearization of robots with variable joint stiffness. In *Proceedings of the IEEE International Conference on Robotics and Automation*, 2008.

[44] J. Rummel, Y. Blum, and A. Seyfarth. Robust and efficient walking with spring-like legs. *Bioinspiration and Biomimetics*, 5(4):046004, 2010.

[45] J. K. Salisbury. Active stiffness control of a manipulator in Cartesian coordinates. In *Proceedings of the IEEE Conference on Decision and Control including the Symposium on Adaptive Processes*, pages 95–100, 1980.

[46] R. Schiavi, G. Grioli, S. Sen, and A. Bicchi. VSA-II: A novel prototype of variable stiffness actuator for safe and performing robots interacting with humans. In *Proceedings of the IEEE International Conference on Robotics and Automation*, pages 2171–2176, 2008.

[47] A. L. Schwab and M. Wisse. Basin of attraction of the simplest walking model. In *Proceedings of the ASME Design Engineering Technical Conference*, 2001.

[48] A. Seeni, B. Schafer, B. Rebele, and N. Tolyarenko. Robot mobility concepts for extraterrestrial surface exploration. In *Proceedings of the IEEE Aerospace Conference*, pages 1–14, 2008.

[49] A. Shiriaev, J. W. Perram, and C. Canudas-de-Wit. Constructive tool for orbital stabilization of underactuated nonlinear systems: Virtual constraints approach. *IEEE Transactions on Automatic Control*, 50(8):1164–1176, 2005.

[50] S. Stramigioli. *Modeling and IPC Control of Interactive Mechanical Systems: a Coordinate-free Approach.* Springer, 2001.

[51] S. Stramigioli and M. van Dijk. Energy conservative limit cycle oscillations. In *Proceedings of the 17th IFAC World Congress*, pages 15666–15671, 2008.

[52] S. Stramigioli, G. van Oort, and E. Dertien. A concept for a new energy efficient actuator. In *Proceedings of the IEEE/ASME International Conference on Advanced Intelligent Mechatronics*, pages 671–675, 2008.

[53] S. H. Strogatz. *Nonlinear Dynamics and Chaos.* Perseus Books, 1994.

[54] G. Tonietti, R. Schiavi, and A. Bicchi. Design and control of a variable stiffness actuator for safe and fast physical human/robot interaction. In *Proceedings of the IEEE International Conference on Robotics and Automation*, pages 526–531, 2005.

[55] M. Uemura and S. Kawamura. Resonance-based motion control method for multi-joint robot through combining stiffness adaptation and iterative learning control. In *Proceedings of the IEEE International Conference on Robotics and Automation*, pages 1543–1548, 2009.

[56] M. Uemura, K. Kimura, and S. Kawamura. Generation of energy saving motion for biped walking robot through resonance-based control method. In *Proceedings of the IEEE/RSJ International Conference on Intelligent Robots and Systems*, pages 2928–2933, 2009.

[57] R. Q. van der Linde. Active leg compliance for passive walking. In *Proceedings of the IEEE International Conference on Robotics and Automation*, pages 2339–2344, 1998.

[58] A. J. van der Schaft. *L_2-Gain and Passivity Techniques in Nonlinear Control.* Springer, 2000.

[59] R. van Ham, T. G. Sugar, B. Vanderborght, K. W. Hollander, and D. Lefeber. Compliant actuator designs. *IEEE Robotics and Automation Magazine*, 16(3):81–94, 2009.

[60] R. van Ham, B. Vanderborght, M. van Damme, B. Verrelst, and D. Lefeber. MACCEPA: the mechanically adjustable compliance and controllable equilibrium position actuator for ‘controlled passive walking’. In *Proceedings of the IEEE International Conference on Robotics and Automation*, pages 2195–2200, 2006.

[61] B. Vanderborght, N. G. Tsagarakis, C. Semini, R. van Ham, and D. G. Caldwell. MACCEPA 2.0: Adjustable compliant actuator with stiffening characteristic for energy efficient hopping. In *Proceedings of the IEEE International Conference on Robotics and Automation*, 2009.

[62] B. Vanderborght, R. van Ham, D. Lefeber, T. G. Sugar, and K. W. Hollander. Comparison of mechanical design and energy consumption of adaptable, passive-compliant actuators. *International Journal of Robotics Research*, 28(1):90–103, 2009.

[63] B. Verrelst, R. van Ham, B. Vanderborght, F. Daerden, and D. Lefeber. The pneumatic biped “LUCY” actuated with pleated pneumatic artificial muscles. *Autonomous Robots*, 18(2):201–213, 2005.

[64] L. C. Visser, R. Carloni, F. Klijnstra, and S. Stramigioli. A prototype of a novel energy efficient variable stiffness actuator. In *Proceedings of the IEEE International Conference on Engineering in Medicine and Biology*, pages 3703–3706, 2010.

[65] L. C. Visser, R. Carloni, and S. Stramigioli. Energy efficient control of robots with variable stiffness actuators. In *Proceedings of the IFAC International Symposium on Nonlinear Control Systems*, pages 1199–1204, 2010.

[66] L. C. Visser, R. Carloni, and S. Stramigioli. Variable stiffness actuators: a port-based analysis and a comparison of energy efficiency. In *Proceedings of the IEEE International Conference on Robotics and Automation*, pages 3279–3284, 2010.

[67] L. C. Visser, R. Carloni, and S. Stramigioli. Energy efficient variable stiffness actuators. *IEEE Transactions on Robotics*, 27(5):865–875, 2011.

[68] L. C. Visser, R. Carloni, R. Ünal, and S. Stramigioli. Modeling and design of energy efficient variable stiffness actuators. In *Proceedings of the IEEE International Conference on Robotics and Automation*, pages 3273–3278, 2010.

[69] L. C. Visser, S. Stramigioli, and R. Carloni. Robust bipedal walking with variable leg stiffness. In *Proceedings of the IEEE International Conference on Biomedical Robotics and Biomechatronics*, pages 1626–1631, 2012.

[70] L. C. Visser, S. Stramigioli, and R. Carloni. Control strategy for energy efficient bipedal walking with variable leg stiffness. In *Proceedings of the IEEE International Conference on Robotics and Automation*, 2013.

[71] H. Vu Quy, L. Aryananda, F. Sheikh, F. Casanova, and R. Pfeifer. A novel mechanism for varying stiffness via changing a novel mechanism for varying stiffness via changing transmission angle. In *Proceedings of the IEEE International Conference on Robotics and Automation*, pages 5076–5081, 2011.

[72] M. Wassink and S. Stramigioli. Towards a novel safety norm for domestic robotics. In *Proceedings of the IEEE/RSJ International Conference on Intelligent Robots and Systems*, pages 3354–3359, 2007.

[73] M. M. Williamson. Series elastic actuators. Technical report, Massachusetts Institute of Technology, 1995.

[74] S. Wolf, O. Eiberger, and G. Hirzinger. The DLR FSJ: Energy based design of a variable stiffness joint. In *Proceedings of the IEEE International Conference on Robotics and Automation*, pages 5082–5089, 2011.

[75] S. Wolf and G. Hirzinger. A new variable stiffness design: Matching requirements of the next robot generation. In *Proceedings of the IEEE International Conference on Robotics and Automation*, pages 1741–1746, 2008.

[76] M. Zefran and V. Kumar. Affine connections for the cartesian stiffness matrix. In *Proceedings of the IEEE International Conference on Robotics and Automation*, pages 1376 – 1381, 1997.

[77] G. Zeng and A. Hemami. An overview of robot force control. *Robotica*, 15(5):473–482, 1997.

DANKWOORD

Het einde van het proefschrift en het einde van een gedenkwaardige tijd als promovendus. Zonder langdradig te worden wil ik dit moment gebruiken om een aantal mensen te bedanken.

In de eerste plaats Stefano, die zijn woord hield en, ook op het allerlaatste moment, een plek voor mij had als promovendus. Ook wil ik je bedanken voor de vele discussies en uitleg, welke mij altijd veel geholpen hebben. Raffaella, bedankt voor de alle steun, hulp en begeleiding in de afgelopen jaren. Ik mocht altijd binnenlopen met vragen, en je eindeloze correcties op mijn schrijven hebben mij weliswaar veel tijd gekost, maar waren zeer waardevol.

Ik wil ook iedereen op de vakgroep bedanken voor alle hulp en steun, in grote en kleine mate. En natuurlijk bedankt voor de goede tijd die ik heb gehad bij de groep, tijdens en na werktijd.

Mijn bijzondere dank gaat uit naar mijn familie en vrienden, die mij in de afgelopen jaren altijd zijn blijven steunen. Ook in tijden waarin het allemaal niet zo soepel ging stonden jullie altijd voor mij klaar.

Ludo

ABOUT THE AUTHOR

Ludo Visser was born in Arnhem and moved to Enschede to pursue his studies in Electrical Engineering at the University of Twente. As part of the study program, he completed an internship at Oakland University in Rochester, Michigan (USA), working on navigation algorithms for autonomous vehicles. In 2008, he obtained the M.Sc. degree after completing his final thesis work on motion control of a humanoid robotic head. After graduation, he continued to obtain his Ph.D. degree under the supervision of Stefano Stramigioli and Raffaella Carloni.

STELLINGEN

behorende bij het proefschrift getiteld

VARIABLE STIFFNESS ACTUATORS: MODELING, CONTROL, AND APPLICATION TO COMPLIANT BIPEDAL WALKING

in het openbaar te verdedigen op vrijdag 17 mei 2013 om 12:45 uur door

Ludo Christian Visser

1. Actuatoren met variabele stijfheid kunnen het energieverbruik reduceren enkel als het veranderen van de stijfheid slechts weinig energie kost. (Hoofdstuk 3)
2. Actuatoren met interne elastische elementen kunnen onbedoeld energie opslaan die was bedoeld om arbeid mee te verrichten. (Hoofdstuk 3)
3. Periodieke bewegingen kunnen efficiënt aangestuurd worden door actuatoren met interne elastische elementen, omdat negatieve arbeid kan worden omgezet in herbruikbare elastische energie. (Hoofdstuk 4)
4. Tweebenige lopende robots kunnen significant profijt hebben van regelalgoritmen gebaseerd op variabele beenstijfheid. (Hoofdstuk 5)
5. Wiskunde is een krachtig gereedschap; het is een middel om ingewikkelde problemen elegant te beschrijven, maar het is ook een middel om eenvoudige problemen ingewikkeld te laten lijken.
6. Het nut van geautomatiseerde symbolische manipulatie van vergelijkingen kan niet overschat worden.
7. Wiskundige details beschreven als “eenvoudig”, “een direct gevolg van het voorafgaande”, of “een oefening voor de lezer” zijn vaak alleen eenvoudig, een direct gevolg van het voorafgaande, of een eenvoudige oefening voor de auteur.
8. Wetenschappelijk onderzoek is als het verkennen van onbekende gebieden: je komt interessante dingen tegen in alle richtingen, maar je moet altijd in gedachten houden waar je in de eerste plaats naar op zoek was.
9. Het gros van des werelds problemen is het gevolg van het vermogen van de mensheid zich sneller voor te planten dan de snelheid waarmee de mensheid de samenleving kan reorganiseren om toenemende bevolkingsaantallen te onderhouden.
10. De morgenstond heeft goud in de mond, maar een uurtje later beginnen kan ook geen kwaad.

PROPOSITIONS

belonging to the thesis titled

VARIABLE STIFFNESS ACTUATORS: MODELING, CONTROL, AND APPLICATION TO COMPLIANT BIPEDAL WALKING

to be defended in public on Friday, May 17, 2013 at 12:45 by

Ludo Christian Visser

1. Variable stiffness actuators can reduce energy consumption only if changing the stiffness can be done in an energy-efficient way. (Chapter 3)
2. Actuators with internal elastic elements can unintentionally store energy that was meant to do work. (Chapter 3)
3. Periodic motions can be efficiently realized by actuators with internal eleastic elements, because negative work can be converted in reusable elastic energy. (Chapter 4)
4. Bipedal walking robots can significantly benefit from control algorithms based on variable leg stiffness. (Chapter 5)
5. Mathematics is a powerful tool; it provides a way to describe complicated problems elegantly, but it is also a way to obfuscate simple problems.
6. The benefits of automated symbolic manipulation of equations cannot be overestimated.
7. Mathematical details described as “easy”, “following directly from the preceding”, or “left as an exercise for the reader” are often only easy, following directly from the preceding, or an easy exercise for the author.
8. Research is like exploring uncharted areas: you see something interesting in every direction, but you should keep in mind what your were looking for in the first place.
9. The majority of the world’s problems are the result of the capability of mankind to reproduce faster than the speed with which mankind can reorganize society to accomodate growing population numbers.
10. The morning hour is golden, but starting a bit later does not hurt either.

ISBN 978-90-365-3551-9